The Calibration of Material Properties for Use in Discrete Element Models

by

Etienne Horn

Thesis presented in partial fulfilment of the requirements for the degree Master of Science in Engineering (Mechanical) at the University of Stellenbosch

Supervisor: Dr. C.J. Coetzee

Faculty of Engineering

Department of Mechanical and Mechatronic Engineering

March 2012

Declaration

By submitting this thesis electronically, I declare that the entirety of the work contained therein is my own, original work, that I am the sole author thereof (save to the extent explicitly otherwise stated), that reproduction and publication thereof by Stellenbosch University will not infringe any third party rights and that I have not previously in its entirety or in part submitted it for any qualification.

Signature: .....

E. Horn

Date: 1 March 2012

Abstract

One of the main challenges in using the Discrete Element Method (DEM) is to specify the correct input parameter values. In general, the models are sensitive to the input parameter values and accurate results can only be achieved if the correct values are specified. For the linear contact model, micro parameters such as the particle density, stiffness, coefficient of friction, as well as the particle size and shape distributions are required. Thus, there is a need for a procedure to accurately calibrate these parameters before any attempt can be made to accurately model a complete bulk materials handling system.

Since the DEM is often used to model applications in the mining and quarrying industries, a calibration procedure was developed for materials that consist of relatively large (up to 40 mm in size) particles. A coarse crushed aggregate was used as the test material. Using a specially designed large scale shear box, the confined Young's Modulus and internal friction angle of the material were measured by means of the confined compression test and the direct shear test respectively. The bulk (macro) density and porosity were also measured. The particle size distribution was measured while visual inspection was used to identify the different particle shapes.

DEM models of the experimental set-up were developed and the input parameter values were varied iteratively until a close correlation between the experimental and numerical results was achieved. The resulting set of input parameter values were then verified through a series of anchor pull-out and angle of repose experiments and simulations. A good correlation between the experimental and numerical results was observed.

In a study, independent of the calibration process, a half fraction factorial design was implemented to quantify the effect of the input parameter values on the bulk properties and to construct multiple linear regression models that relate the parameters to the bulk properties. The results were found to be in accordance with expected bulk behaviour, and can be used to develop advanced DEM calibration strategies.

Based on the project outcomes, it was concluded that the developed calibration procedure performed satisfactorily and that the calibrated input parameters allow for the accurate modelling of the coarse aggregate.

Opsomming

Een van die groot uitdagings in die gebruik van die Diskreet Element Metode (DEM) is om die korrekte invoer parameterwaardes te spesifiseer. Die modelle is in die algemeen sensitief vir die invoer parameterwaardes, en akkurate resultate kan slegs verkry word indien die korrekte waardes gespesifiseer word. Mikro-parameters soos partikeldigtheid, styfheid, wrywingskoëffisiënt, die partikelgrootte verspreiding asook die partikelvorm verspreiding, word benodig vir die lineêre kontakmodel. 'n Prosedure word dus benodig om hierdie parameters akkuraat te kalibreer alvorens 'n volledige korrelagte materiaal-hanteringstelsel akkuraat gemodelleer kan word.

Aangesien die DEM gereeld in die modellering van myn- en gruisgroefbedryf toepassings gebruik word, is 'n kalibrasieprosedure ontwikkel vir materiaal wat bestaan uit relatief groot (tot 40 mm in grootte) partikels. Grofgebreekte klippe is as toetsmateriaal gebruik. Deur gebruik te maak van 'n spesiaal ontwerpte grootskaal-skuifboks is die ingeperkte Young se Modulus en die interne wrywingshoek van die materiaal gemeet deur middel van die ingeperkte kompressietoets en die direkte skuiftoets onderskeidelik. Die makro-digtheid en poreusheid is ook gemeet. Die partikelgrootte verspreiding is gemeet terwyl visuele inspeksie gebruik is om die verskillende partikelvorms te identifiseer.

DEM modelle van die eksperimentele opstelling is ontwikkel en die invoer parameterwaardes is herhaaldelik gewysig totdat 'n goeie korrelasie verkry is tussen die eksperimentele en numeriese resultate. Die gevolglike stel invoer parameterwaardes is daarna geverifieer deur 'n reeks ankeruittrek- en natuurlike helling eksperimente en simulasies.

In 'n studie, onafhanklik van die kalibrasieproses, is die half-fraksie faktoriaalontwerp geïmplementeer om die invoer parameterwaardes se effek op die makro eienskappe te kwantifiseer en om meervoudige lineêre regressiemodelle te ontwikkel wat die parameters met die makro eienskappe verbind. Die resultate was in ooreenstemming met die verwagte makro gedrag en kan gebruik word om gevorderde DEM kalibrasie-strategieë te ontwikkel.

Daar is tot die gevolg gekom dat, gebaseer op die projekresultate, die ontwikkelde kalibrasieprosedure bevredigend presteer en dat die gekalibreerde invoer parameters die akkurate modellering van die grofgebreekte klippe toelaat.

Acknowledgements

I would like to express a sincere word of gratitude to the following people, without whom this project would not have been possible:

- My supervisor, Dr. Corné Coetzee, for his guidance, helpful advice and patience throughout this project.
- Mr. Ferdi Zietsman, for his contributions and advice in building the experimental apparatus.
- Mr. Alex Oelofse, for his assistance with conducting the experimental work.
- My friends, who made my time at Stellenbosch very memorable.
- My parents, for giving me the opportunity and blessing to follow my dreams.
- Marsunet Scholtz, for her love and support, for encouraging me when it all seemed hopeless and for believing in me. *Baie dankie, Engel!*

Opgedra aan Renier Pretorius (1919 - 2010)

Table of Contents

List of Tables

List of Figures

List of Symbols

k_n	Normal contact stiffness
k_s	Shear (tangential) contact stiffness
μ	Friction coefficient
k_p	Normal and tangential particle stiffness
μ_{pp}	Inter-particle friction coefficient
ρ_p	Particle density
k_w	Normal and tangential wall stiffness
μ_{pw}	Particle-wall friction coefficient
σ_x	Mean (bulk) stress in x-direction (shear)
ε_x	Mean (bulk) strain in x-direction (shear)
σ_z	Mean (bulk) stress in z-direction (normal)
ε_z	Mean (bulk) strain in z-direction (normal)
σ_y	Mean (bulk) stress in y-direction
ε_y	Mean (bulk) strain in y-direction
c	Cohesion
ϕ	Internal friction angle
σ_s	Bulk shear stress (simplified notation)
σ_n	Bulk normal stress (simplified notation)
ε_s	Bulk shear strain (simplified notation)
ε_n	Bulk normal strain (simplified notation)
ψ	Angle of dilatancy
F_n	Total normal load on bulk material packing
$F_n^{recorded}$	Normal load reading on load cell
F_l	Weight load of lid
F_s	Nett shear load on bulk material packing

$F_s^{recorded}$	Shear load reading on load cell
F_{rf}	Rolling friction force (on castor wheels)
μ_{rf}	Rolling friction coefficient
F_{bh}	Weight load of bottom container half
F_m	Weight load of bulk material
A	Container cross-sectional area
d_n	Normal displacement of lid
d_s	Shear (horizontal) displacement of container bottom half
E'	Confined Young's Modulus
E	Young's Modulus
υ	Poisson's Ratio
k_b	Average bulk stiffness
H	Initial packing height
V_b	Bulk volume (initial)
m_b	Bulk mass
ρ_b	Bulk density (initial)
n	Porosity (initial)
e	Voids ratio (initial)
C	Overlap factor
R	Sphere radius (general)
R_{min}	Minimum sphere radius
R_{max}	Maximum sphere radius
γ	Sliding angle
ξ	Critical (viscous) damping ratio
V_v	Voids volume (total)
V_s	Solid volume (total)

m_s	Sample mass
V_d	Displaced volume (water)
V_l	Lens (overlap) volume
R_1	Radius of 1st sphere (double clump)
R_2	Radius of 2nd sphere (double clump)
D	Distance between centres of spheres
σ_n^{upper}	Upper normal stress data point (confined compression test)
σ_n^{lower}	Lower normal stress data point (confined compression test)
ε_n^{upper}	Upper normal strain data point (confined compression test)
ε_n^{lower}	Lower normal strain data point (confined compression test)
$\Delta\sigma_x$	Change in shear stress (Cartesian)
$\Delta\sigma_z$	Change in normal stress (Cartesian)
$\Delta\sigma_s$	Change in shear stress (simplified notation)
$\Delta\sigma_n$	Change in normal stress (simplified notation)
$\Delta\varepsilon_n$	Change in normal strain (simplified notation)
α	Angle of repose (subscript added for individual values)
α_{exp}^{avg}	Average experimental angle of repose
α_{num}^{avg}	Average numerical angle of repose
L	Packing height (anchor pull-out test)
k	Number of design variables (factors)
y	Response variable
y_i	Response associated with i^{th} run
β_0	y-intercept
β	Regression coefficient (subscript added for associated factor, 2nd and 3rd order interaction)

x_i	Factor value associated with i^{th} run (subscript added for associated factor)
ε_i	Random error associated with i^{th} run
R^2	Coefficient of determination
A	Factor associated with particle density
B	Factor associated with inter-particle friction coefficient
C	Factor associated with particle-wall friction coefficient
D	Factor associated with particle friction
AB	2nd order interaction between A and B
AC	2nd order interaction between A and C
BC	2nd order interaction between B and C
ABC	3rd order interaction between A, B and C
F_n^{μ}	Normal load on castor tracks (rolling friction estimation)
m_1	Mass of weight in container (rolling friction estimation)
m_2	Mass of bottom container half (rolling friction estimation)
F_s^{μ}	Recorded friction force (rolling friction estimation)

List of Abbreviations

DEM	Discrete Element Method
DOE	Design of Experiments
FEM	Finite Element Method
PIC	Particle in Cell
CFD	Computational Fluid Dynamics
PFC^{3D}	Particle Flow Code in Three Dimensions
ANOVA	Analysis of Variance
PB	Plackett-Burman
CCD	Central Composite Design
RSM	Response Surface Method
DST	Direct Shear Test
CCT	Confined Compression Test
PID	Proportional-Integral-Derivative
PLC	Programmable Logic Controller
HBM	Hottinger Baldwin Messtechnik
LVDT	Linear Variable Differential Transducer
BDPVR	Bulk Density, Porosity and Voids Ratio

1. Introduction

The use of the discrete element method (DEM) in the numerical modelling of bulk material handling processes and systems has become very popular in recent years. Advances in computing resources have resulted in the increased usage of the DEM as a design validation and process optimisation tool as opposed to expensive physical prototyping (Nordell, 1997, Hastie *et al.* 2008, Gröger and Katterfeld, 2006).

In addition to the general engineering challenges usually associated with simulating complex systems from a pre-processing perspective, a crucial element of discrete element modelling lies in the acquisition of accurate and reliable material input properties. Since natural bulk materials are mostly complex, non-linear materials that are frequently affected by external conditions and geographic locations, obtaining the appropriate input parameter values can become very challenging.

A large variety of experimental test procedures exist with which bulk material properties can be quantified. The results from these tests are normally related to the relevant DEM input parameters by means of a calibration procedure. Common challenges in using a calibration procedure include the large time scales normally needed to perform the calibration experiments and subsequent numerical calibration. In some cases the calibration of the bulk material can be the largest component of a DEM simulation project. This is also worsened in that the input parameters are mostly calibrated one at a time, using very simple iterative strategies. This ultimately causes the overall calibration procedure to be very inefficient and time consuming.

Therefore a clear need exists for calibration procedures that are more efficient from both an experimental and numerical point of view. Robust experimental tests are required that can quantify most of the desired bulk material properties and also provide for the effective comparison to the DEM input parameters. Improved numerical calibration strategies are also needed to enable more efficient optimisation of these input parameters.

Most of the available and commercial test equipment that can be used to quantify the bulk properties have been developed for relatively fine bulk materials such as sands, soils and powders. These equipment cannot be used effectively when materials from the mining and quarrying industries are considered, where substantially larger constituents are usually present. For the calibration of these materials, large scale test equipment are needed that can account for the larger sized particles.

1.1 Objectives

The main objective of this project was to develop test equipment that could be used in the DEM calibration of a coarse aggregate and to conduct a calibration process using the equipment and applicable DEM simulations. The focus was on the calibration of the DEM input parameters for a material with relatively large particles (up to 40 mm in size) as applicable to the mining and quarrying industries. The following objectives were identified:

- The design and construction of a large scale shear box for conducting confined compression tests and direct shear tests.
- The measurement of material properties for use in the DEM model such as particle size, shape and density.
- The measurement of the confined Young's Modulus and internal friction angle using the large scale shear box.
- The modelling of the confined compression test and direct shear test to determine the correct set of DEM input parameter values.
- Devise and conduct experiments for the validation of the calibration procedure.
- Utilise design of experiments (DOE) to determine how sensitive the calibration procedure is to the DEM input parameter values. This study is independent of the calibration process and the results will be used in future work to improve the calibration procedure.

1.2 Motivation

It is estimated that 40% of the capacity of industrial plants are wasted because of bulk handling problems (Tijskens *et al*. 2006). Considering the scale and importance of bulk material handling operations in industry, ranging from the mining and pharmaceutical to the agricultural industries, the positive economic impact of more efficient systems, from a design and operational point of view, cannot be ignored. For the DEM to be utilised more readily as a relevant engineering tool in the development of more efficient systems, certain aspects need to be addressed.

A very important aspect that could have a profound impact on the DEM's popularity and relevance is the availability of adequate calibration procedures. Insights into bulk material behaviour can be obtained, which can be of significant engineering value. This would ultimately enable engineers to overcome an obstacle that in general has prohibited the DEM to be effectively used in more applications.

2. Literature Overview

2.1 Numerical Modelling of Bulk Materials

In recent decades, the need to model bulk material behaviour has increased significantly. Typical scenarios include classic rock and soil mechanics applications in the civil engineering and construction industries, as well as more non-linear systems such as rock failure and breakage in the mining and quarrying industries. Powder processing in the pharmaceutical and metallurgical industries also contribute largely to bulk material applications.

A variety of applications are also concerned with the processing of general bulk materials such as ore, aggregate and agricultural products. With systems such as conveyor belts, hoppers, chutes, dragline buckets and crushers in the mining industries, the knowledge of the static and dynamic behaviour of bulk materials has become indispensible. Bulk material knowledge is also used extensively in the design and development of silos and agricultural equipment such as tillage tools.

The large and generally complex nature of these systems have resulted in the increasing use of numerical methods to simulate bulk material behaviour during the design and development processes as well as system optimisation. With the significant improvements in computational resources since the early nineties, the use of numerical methods is surpassing physical prototypes due to the financial and practical advantages (Nordell, 1997).

Conventionally, two general disciplines are used to simulate bulk material behaviour, namely continuum mechanics and discrete element methods (DEM). Using continuum methods the bulk material is typically considered as a continuous, elastoplastic, medium that is deformable (Frenning, 2008). Due to this approximation, these methods are usually best suited for finer materials such as powders and sands, where there is a small variation in particle size (Dymond, 2007). The governing equations are solved using the finite element method (FEM). Continuum methods have been used successfully in the modelling of static bulk material applications where relatively small deformations take place. Where material flow or larger deformations occur, problems can arise from using FEM techniques in the form of remeshing difficulties and mesh distortion when large strains are encountered (Coetzee and Els, 2009). Advanced non-linear finite element techniques and the so-called particle in cell (PIC) methods can be used to account for these complex phenomena from a continuum perspective (Coetzee *et al*. 2007).

Due to the difficulties of using FEM techniques in modelling material failure (such as rock breakage), mixing of different materials and segregation, the DEM has gained more popularity in bulk materials modelling (Coetzee and Els, 2009). Fundamentally the DEM describes the material as individual and interacting particles (Frenning, 2008), by determining the kinematic force and resulting

displacement on each finite-sized particle at each time step (Mio *et al*. 2008). According to Malone and Xu (2008) an advantage of the DEM is that, by tracking the motion of each individual particle, comprehensive information on system behaviour can be obtained over a range of time and length scales. As opposed to continuum methods, the DEM also enables the modelling of fast flowing (fully dynamic), static and quasi-static zones within a bulk material system using the same constitutive equations (Gröger and Katterfeld, 2006).

Frenning (2008) also highlighted a third method that combines the continuum and discrete element methods, which is typically used to model powder compression. In this combined DEM/FEM method, each particle is described as a deformable continuous body (using the FEM), while the particle movements and interactions are considered using the DEM (Frenning, 2008). According to Coetzee and Els (2009), in recent years the use of computational fluid dynamics (CFD) has also been investigated in the modelling of bulk material flow applications. The use of CFD in liquid dominated bulk flow applications, such as slurry pumps, could be useful. However, more research is needed to validate the suitability thereof.

An important disadvantage of the DEM, as well as the combined DEM/FEM method, is the computational intensity of using these methods as opposed to pure continuum methods. This is due to the large amounts of information that are typically obtained on a particulate level, causing increasing numbers of particles along with increasing calculation steps, to require substantially more computational resources. Malone and Xu (2008) and Mio *et al*. (2008) discuss a number of solutions to reduce the computational load of the DEM; the most popular of which is the use of lower particle stiffness values to enable a larger time step to be used. This is of particular use when the simple linear contact model is used in the DEM, as will be discussed in Section 2.2. Other approaches include the use of advanced contact detection algorithms and parallel computing.

Nevertheless, due to increasing computational power and ongoing refinements in the DEM, which was originally developed by Cundall and Strack (1979), the DEM's relevance as a numerical tool for bulk materials modelling has become significant. Simulations using the DEM can be viewed as numerical experiments that allow for the contactless measurement of microscopic quantities that are usually impossible to quantify using physical experiments. Typical data can then be used to visualise the process and also to compute macroscopic (bulk) quantities such as stresses and mean velocities (Gröger and Katterfeld, 2006). This can prove to be very useful in the design and optimisation of equipment and processes.

In this project the numerical work was performed using the DEM as implemented in the commercial software package PFC^{3D}, by the Itasca Consulting Group in Minneapolis (Itasca, 2003). In the following section a brief background into the DEM is presented.

2.2 The Discrete Element Method (DEM)

The discrete element method is essentially based on the simulation of the motion of granular materials as individual particles (Coetzee and Els, 2009). In general the DEM consists of two stages, the first one being the use of a suitable contact model to resolve any forces acting on a particle in the system. This is then followed by an application of Newton's second law of motion to calculate changes in the motion of particles resulting from any unbalanced forces (Malone and Xu, 2008). For a more detailed description into the DEM, the reader is referred to Itasca (2003).

Using the soft particle approach, each contact is modelled with a linear spring in the contact normal direction (with stiffness k_n) and a linear spring in the contact tangential or shear (with stiffness k_s) direction, as seen in Figure 2.1. Frictional slip is allowed in the tangential direction with a friction coefficient (μ).

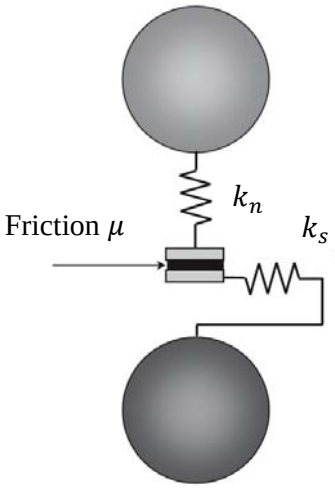

Figure 2.1 - The Linear Contact DEM Model (Coetzee and Els, 2009)

The particles are allowed to overlap and the amount of overlap is used in combination with the spring stiffness values to calculate the respective contact forces for each time step. Newton's second law is then applied to determine particle accelerations, which are numerically integrated using an explicit scheme, to find particle velocities and displacements (Hanley *et al*. 2011). This then ultimately allows for the particle positions and orientations to be updated after each time step.

A damping force can also be accounted for which acts on a particle in the opposite direction to the global particle velocity and is proportional to the resultant force applied on the particle with a damping coefficient (Coetzee *et al*. 2010). The contact model is typically modified by adding a viscous damper in both the normal and tangential directions.

The abovementioned basic linear contact model is found in most commercially available DEM software packages and is also the default model implemented in PFC^{3D} (Coetzee *et al.* 2010). By specifying bonds at the contacts, cohesion between particles can also be modelled. In this project a dry, cohesionless, friction dominated material in the form of crushed aggregate was investigated, thus bonds were not necessary. Other contact models such as the non-linear modified Hertz-Mindlin contact model and the Walton-Braun model can also be used to model more complex contact behaviour. However, these approaches are usually computationally less efficient than the basic linear contact model.

The default particles in most commercially available DEM packages are spherical. However, when using spherical particles, the macro or bulk friction of the simulated material is usually lower than that of a real granular material like crushed aggregate. Thus, non-spherical particles are needed to increase the particle interlocking effect (Coetzee *et al.* 2010) that typically results in higher bulk friction characteristics. Different methods are used to model different shapes in the DEM. Shape descriptors (in 2D and 3D) range from ellipses or ellipsoids, superquadric bodies, discrete functions, shape combinations and composite particles (Kruggel-Emden *et al.* 2008).

In the composite approach simple geometries (such as spheres) are clustered together to represent a more complex shape (Kruggel-Emden *et al.* 2008). This is also known as the multi-sphere method and forms the basis on which the so-called clump logic in PFC^{3D} is based. According to Kruggel-Emden *et al.* (2008) this method has the advantage that contact detection and force calculation are based on simple algorithms and are therefore very efficient and robust. A drawback is that, although it is commonly used, research on its validity is very limited and even contradictory. Despite these limitations the multi-sphere method is still the most general and efficient method for representing complex shapes within the DEM (Kruggel-Emden *et al.* 2008).

Particles comprising the clump remain at a fixed distance from each other and can also overlap to any extent without generating contact forces between these particles (Itasca, 2003). Furthermore, clumps cannot break up during simulations regardless of the forces acting upon them. In PFC^{3D} a clump is also regarded as a rigid particle, although the boundaries are still subjected to the relevant force-displacement law to allow for overlaps when contact with other clumps is detected (Itasca, 2003).

In order to successfully use a linear contact particle model in PFC^{3D} to simulate the material for this project, the following micro parameters need to be defined: the normal and tangential particle stiffness, k_p, the friction coefficient between the particles (also referred to as the inter-particle friction, μ_{pp}), the damping characteristics (in the form of the normal and shear critical viscous damping ratios, together with local damping coefficients) and the density of the particles, ρ_p. The wall stiffness (k_w), in both the normal and tangential directions, also need

to be specified to account for any interface contacts with the particles. The tangential (shear) contact parameters are mostly based on the value of their normal counterparts (Malone and Xu, 2008) and were also implemented as such in this project.

Furthermore, the friction coefficient between the particles and the interfaces also needs to be defined (also known as the particle-wall friction coefficient, μ_{pw}). Size parameters are defined in the form of minimum and maximum ball radii (for spherical particles), with a size distribution if necessary. When alternative shapes are modelled, minimum and maximum clump sizes are defined according the applicable shapes' geometric parameters. Again, a size distribution can also be specified.

2.3 DEM Parameter Calibration

A very important challenge in using the DEM successfully is to select the correct micro parameters so that the simulated system's behaviour and responses, match the real life physical system as close as possible. Since the main purpose of simulating a bulk material process in the DEM is to achieve an accurate model of the bulk behaviour of the material, material properties that affect the material behaviour at the particulate level, need to be defined, which will dictate the overall bulk behaviour as desired (Curry *et al*. 2009).

The direct measurement of particle properties from an industrial process is not always possible. Measuring the individual particle micro properties and applying them directly in the simulation also do not guarantee accurate results (Curry *et al*. 2009). A calibration process is therefore needed to obtain these micro properties. During a calibration procedure the relevant DEM micro parameters are varied until a simulated model response corresponds closely to an equivalent physical experimental response (Hanley *et al*. 2011). The core of a calibration procedure entails experimental work, in which certain bulk properties are measured as the experimental responses. The experimental set-up and procedure are then simulated in the DEM, where the micro properties are then varied until the responses correspond.

In general, the calibration approach is a simple procedure where the micro parameters are varied individually and the effect on the responses measured (Hanley *et al*. 2011). These variations in micro properties typically take place in an iterative manner. The calibration work performed for this project was approached using this methodology, as discussed in Chapter 4.

A large variety of experimental test procedures have been developed over the centuries to measure bulk material characteristics with which elastic contact, friction and cohesion properties, amongst others, can be quantified. Most of the tests focus on a specific characteristic and are used to good effect in calibration procedures to obtain their applicable micro properties. In the following section a

quick review on different test procedures is given. This is followed by a brief overview of more advanced calibration procedures using design of experiments (DOE) strategies.

2.3.1 Characterisation Experiments

Flow characteristics of bulk materials are in many cases the primary concern when characterising these materials, since the results are usually needed in the design and development of equipment that store, transport and process bulk materials (Schwedes, 2003). In a comprehensive review on flow property testers by Schwedes (2003), a wide variety of testers is discussed. Along with cohesion, friction properties influence the flow properties of a bulk material significantly (Gröger and Katterfeld, 2006). The majority of flow property testers are concerned with the quantification of friction characteristics, considering that bulk friction is one of the most complex parameters due to its dependence on micro friction, particle shape and size distribution, packing structure and bulk density (Gröger and Katterfeld, 2006).

Popular tests include the direct shear test (in the form of the Jenike Shear Tester), uniaxial test, biaxial shear test, ring and torsional shear tests, triaxial test, the penetration test and avalanching methods which include angle of repose techniques (Schwedes, 2003). Bulk elastic (stiffness) characteristics can be obtained by means of tests such as the confined compression test and the triaxial test.

Wall friction properties can be measured using the Jenike Wall Friction Tester, which is a modified version of the conventional Jenike Shear Tester. Since typical samples for these offline tests are very small and their representation of the full batch of material not always realistic, researchers such as Pillai *et al*. (2007) have suggested the use of a so-called online wall friction tester, that enables a more continuous flowability of a material, to be investigated. Liu *et al*. (2005) also suggests an in-situ direct shear test method with which field tests can be conducted.

As the friction and elastic characteristics are the main parameters that were investigated in this project, the experimental work focussed mainly on the direct shear test and the confined compression test. These tests and the supporting experimental work are discussed in more detail in Chapters 3 and 4.

2.3.2 A Background on DOE in DEM Parameter Calibration

The fundamentally simple calibration approach of varying one micro property at a time has a number of disadvantages as pointed out by Hanley *et al*. (2011). This includes the lengthy time scales normally needed to obtain the correct set of micro properties. The total number of DEM simulations needed for the calibration is very difficult, or even impossible in some cases, to know beforehand. Also, the

final set of parameters obtained may not be the optimal, due to the limited insights into the complex interactions of the micro parameters (Hanley *et al*. 2011). To overcome these limitations, more efficient DEM calibration approaches have been developed and proposed using design of experiments (DOE) methods.

A variety of DOE methods exist with which the relation between a response (dependent variable) and its factors (independent variables) can be quantified. The effect of each factor on the response can be determined and the most prominent factors singled out. Further data analysis can be done by means of formal regression analysis and analysis of variance (ANOVA) to derive regression models that provide empirical relations between the response and its factors. The factors are also known as design variables. These regression models can then ultimately be used as objective functions and constraints (inequality and equality) in an optimisation scheme to obtain the most appropriate set of micro parameters.

Hanley *et al*. (2011) used the Taguchi method to analyse the influence of input parameters on the simulated response of powder (bonded) agglomerates. The Taguchi method has two main advantages, the first one being that the chosen designs can minimise the amount of information needed. Secondly the analysis methods can clearly identify what is being analysed and relate only to actual system behaviour (Hanley *et al*. 2011). However, an important disadvantage is that the typical orthogonal arrays involved can generate very intricate confoundings (Hanley *et al*. 2011), meaning that a column (assigned design variable) may contain a number of partial or full interactions, in addition to an actual factor (variable).

Yoon (2007) used the Plackett-Burman (PB) design method to determine which micro properties have the largest effects on the uniaxial compressive strength, Young's Modulus and Poisson's ratio for a bulk material that is modelled by means of a contact-bonded particle model in the DEM. This is also known as a screening procedure. Linear regression fits were generated from the results to serve as linear equality and inequality constraints for optimisation purposes. Yoon (2007) then singled out the largest two effects on each bulk property and estimated their non-linear relations to the bulk responses using the Central Composite Design (CCD) method, which is a Response Surface Method (RSM). Non-linear regression fits (2^{nd} order polynomial) were generated to describe the response surfaces and be used as non-linear inequality constraints. Since the objective is to minimise the absolute value of the difference between the experimental bulk property and its equivalent non-linear regression fit (estimation), the objective function was constructed accordingly (Yoon, 2007). The micro properties were then optimised using non-linear constrained optimisation.

The primary reason for the estimation of the non-linear relations using the CCD method is that, although it is possible to express a response as a linear combination of the independent variables, it is more desirable to also allow for the

estimation of interactions and quadratic effects of each independent variable (Yoon, 2007). This will evidently enable a more precise estimation of the responses. Yoon (2007) also points out that the PB design is limited in that it cannot predict interaction effects between factors. Thus, to fully consider the interaction effects, either a full factorial design or a fractional factorial design should be used.

For this project an independent DOE investigation was conducted to evaluate a number of micro property effects on bulk property responses. The simple iterative calibration procedure was still followed in this project to calibrate the micro properties for the physical material. However, due to time constraints, the additional DOE investigation was conducted independently as an additional study to form the foundation from which a future DOE calibration procedure can be developed.

Since a full factorial design is usually disadvantaged by a large number of runs that makes it computationally very expensive, a fractional factorial design approach was used for this project (in the form of a half fraction factorial design), while still accounting for the 2^{nd} order interactions between the micro properties. It should be mentioned that only a screening procedure was performed to identify significant micro properties, while no subsequent response surface estimations and formal optimisation were performed. The higher order (3^{rd} order) interactions were assumed not to be applicable, according to the general assumptions for the half fraction factorial design. The independent DOE investigation for this project is discussed in more detail in Appendix A.

3. Experimental Developments

3.1 Introduction

The test procedure predominantly considered for this project is the direct shear test. The direct shear test (also referred to as the DST in this report) is a widely implemented technique that is used to very good effect to characterise bulk material flow properties. As a result, the bulk friction properties of the material in this project were quantified using this test. The results were then used in the calibration of the relevant DEM micro properties, as discussed in more detail in Chapter 4.

The direct shear test was performed using a so-called shear box (also known as a shear cell, or direct shear tester). For this project a dedicated shear box test set-up was designed and built. In this chapter a brief background on general shear box theory is presented. The shear box design and DST procedure, in the context of the test set-up for this project, is also covered in more detail. Additional applications of the shear box in the form of the confined compression test (also referred to as the CCT), that is used to characterise bulk elastic properties is also briefly discussed.

3.2 Shear Box Theory: A Background

A direct shear test set-up generally consists of a bulk material sample that is contained in a shear box. The shear box is typically constructed of two halves, namely a top and a bottom half. This shear box can be cylindrical, square or rectangular in form. The sample is sheared laterally by moving either the top or bottom half relative to the other, while simultaneously applying a normal load on the sample (on its top level, in a direction normal to shear). This shear displacement normally occurs at a constant velocity. It is mostly assumed that this action induces a thin, well defined shear zone for finer grained materials (Härtl and Ooi, 2008). The mean normal and shear stress acting on this horizontal plane are calculated from the measured normal and shear loads and subsequently used to determine bulk properties such as the internal friction angle (Härtl and Ooi, 2008). A schematic of a typical cylindrical DST set-up can be seen in Figure 3.1, where the bottom half is sheared relative to the top half and the normal load is applied via a lid.

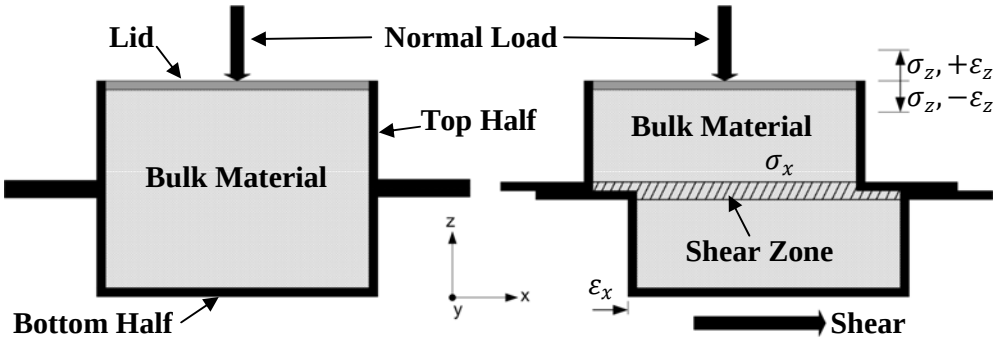

Figure 3.1 - Direct Shear Test Schematic

The mean (bulk) shear stress, σ_x, and strain, ε_x, are used to generate a plot as in Figure 3.2a. Here the typical behaviour of the shear stress on the shear plane, as the strain develops along this plane, can be seen for a fine, powder based, bulk material sample.

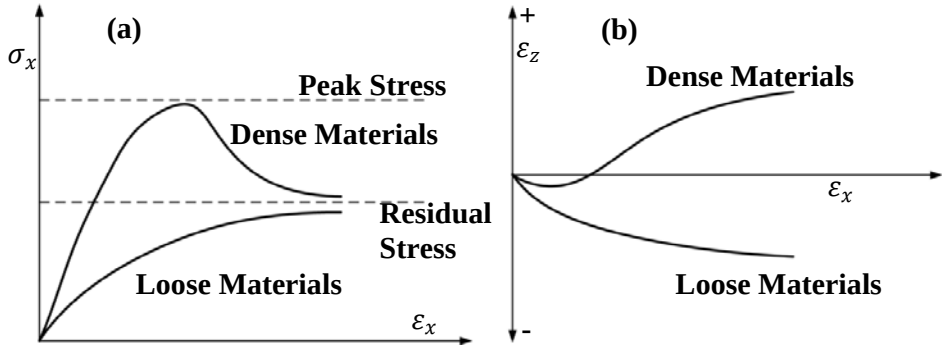

Figure 3.2 - Theoretical Bulk Behaviour during a Direct Shear Test

For a densely compacted material a peak shear stress is visible. At this point shear failure of the sample occurs. After this the shear stress gradually decreases to a steady state region, also known as a residual stress (Coetzee, 2000). For a loosely compacted material, a clear peak shear stress is not observed, even though it still reaches a residual value. In the experimental and numerical results obtained in this project a peak shear stress was rarely obtained (as will be seen in Chapter 4), hence the residual shear stresses were used in further interpretations. Härtl and Ooi (2008) took shear failure in such a case to be at the limiting shear stress, which is in effect the residual shear stress.

The bulk normal strain, ε_z, which is also referred to as the vertical strain by Lee *et al*. (2008) and Yan (2008a & 2008b), can also be represented relative to the bulk shear strain as in Figure 3.2b. Again it should be noted that this is a typical plot for finer materials. For a dense material it can be seen that the material undergoes an initial contraction in the vertical (normal) direction after which it starts to expand or dilate, as the shear strain develops (Head, 1988). When considering a loose material it is generally observed that the material continues to undergo a bulk normal contraction until it reaches a residual normal strain region or value.

A series of these tests is conducted, consisting of three to four runs, each at a different applied normal load. Since the stress-strain relationship for bulk materials is largely stress dependent, the different confining loads will result in different residual shear stresses. Plotting the different residual shear stresses against their respective normal stresses, typically yields a curve as in Figure 3.3, which is also known as a failure (or Coulomb) envelope according to Lee *et al.* (2008) and Head (1988).

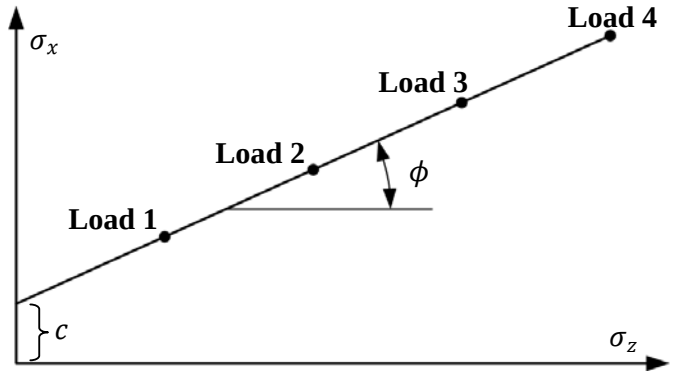

Figure 3.3 - Theoretical Coulomb Envelope for a Bulk Material

A linear fit can be constructed through the data points. This plot is used to good effect to illustrate the Mohr-Coulomb failure criterion (Härtl and Ooi, 2008), which describes the failure of a bulk material mass,

$$\sigma_x = c + \sigma_z \tan\phi \tag{3.1}$$

In this equation, σ_x and σ_z are the residual shear stress and normal stress respectively, c denotes the cohesion and ϕ the internal friction angle. Cohesion effects are important to consider, especially when a finer bulk material with a level of moisture content is present. When a dry, friction dominated material (a so-called $c-\phi$ material) is considered, cohesive effects are negligible, and c indicates the interlocking effects of the entities within the bulk material sample. This makes c a useful parameter in judging the reliability of the particle shape and size distribution, as typically obtained beforehand (see Chapter 4). The gradient of the linear fit was used to obtain the internal friction angle (in the remainder of this thesis the shear and normal stress are denoted by σ_s and σ_n respectively, while shear and normal strain are represented by ε_s and ε_n respectively),

$$\phi = \tan^{-1}\left(\frac{\Delta\sigma_x}{\Delta\sigma_z}\right) = \tan^{-1}\left(\frac{\Delta\sigma_s}{\Delta\sigma_n}\right) \tag{3.2}$$

The plot of the bulk normal strain versus shear strain (Figure 3.2b) can also be used to obtain the angle of dilatancy, ψ. This parameter is very useful in describing the dilatant behaviour of the material. Alejano and Alonso (2005) define dilatancy as a change in bulk volume that results from the shear distortion of the material. For a typical contractive-dilative behaviour (at moderate normal

compression levels) the angle of dilatancy can be defined as the inverse tangent of the relation between the bulk shear and normal displacement of the sample. This will be discussed in more detail in Chapter 4.

In a similar fashion, as to how the internal friction angle is determined, the interface-material friction angle can also be obtained. This is typically done by replacing the bottom half of the container with a plate or thick sheet of the applicable interface material. The abovementioned direct shear test procedure is then performed in the normal way.

Härtl and Ooi (2008) point out fundamental shortcomings of the direct shear test in that there is no information on the stresses in planes other than the shear plane, and that the stress state is non-uniform throughout the sample. This results in the true stresses that cause failure to be largely unknown. The true stress pattern is very complex and the directions of the planes of principal stresses rotate as the shear strain is increased (Head, 1988). The applied shear deformation of the sample is also limited by the maximum length of travel of the system.

Regardless of these disadvantages, the direct shear test still remains a popular test procedure in bulk material characterisation. Its general simplicity and low cost have caused the direct shear test, originally developed as the Jenike Shear Cell, to become an industrial standard (Carson and Wilms, 2006). The Jenike Shear Cell has been developed for use primarily in the testing of soils and powders. As a result, typical shear boxes for these applications are very small. Sizes are in the region of an inner diameter of 95 mm and a total height of 30 mm (Carson and Wilms, 2006) for a cylindrical Jenike Shear Cell, and between 60 x 60 mm and 100 x 100 mm for a square box (Head, 1988).

When bulk materials from the mining and quarrying industries are considered, particle sizes are mostly too large for the conventional Jenike Shear Cell size to perform a direct shear test properly. Since the material used in this project is coarse aggregate, the need for a large scale shear box was identified to account for the larger particle sizes. Head (1988) names a primary advantage of the direct shear test in that the principle can be extended to materials containing larger particles. The implementation of a large scale shear box for this project was thus justified. In the following section the design and operation of the large scale shear box, as implemented in this project, is discussed in more detail.

3.3 Large Scale Shear Box Design

3.3.1 Design and Specifications

General Concept and Layout

The large scale shear box consists of a cylindrical container, divided into a top and bottom half. The container has an inner diameter of 590 mm and a depth of

330 mm and is filled with the bulk material. The top half of the container is fixed to a support frame, while the bottom half is resting on a set of tracks, thus enabling it to be moved horizontally on steel castor wheels. The tracks also form part of the frame. In Figure 3.4 the large scale shear box layout can be seen.

Head (1989) suggests a particle size to bin diameter ratio of less than (or equal to) 0.125 for a similar DST test set-up. He also suggests a particle size to sample height ratio of less than or equal to 0.1 for a confined compression test set-up. As discussed in Section 3.4, the confined compression test was also performed using the large scale shear box's container. The design was therefore done according to these guidelines.

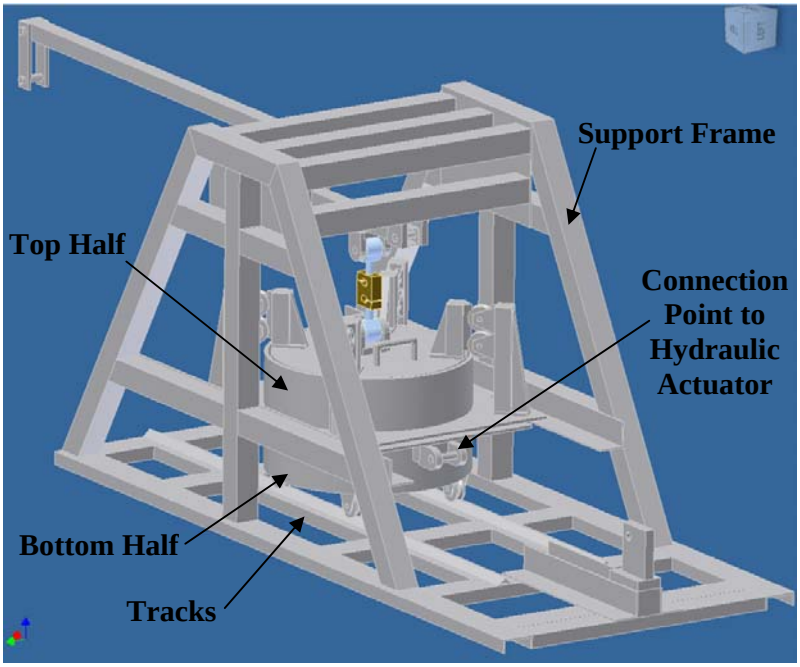

Figure 3.4 - Large Scale Shear Box Layout

The bottom half is connected to a hydraulic actuator (via a 50 kN load cell), which is mounted on the support frame. To facilitate the normal load on the sample, a lid is placed on top of the sample (see Figure 3.5). Guides are used to prevent the lid from twisting and to keep it as level as possible during the DST. The actual normal load is applied by means of a linkage mechanism that is connected to a lid via a 50 kN load cell (Figure 3.5). A gap of 5 mm exists between the top and bottom half as to induce a shear effect in the bulk material sample only, eliminating any steel-on-steel friction between the top and bottom halves.

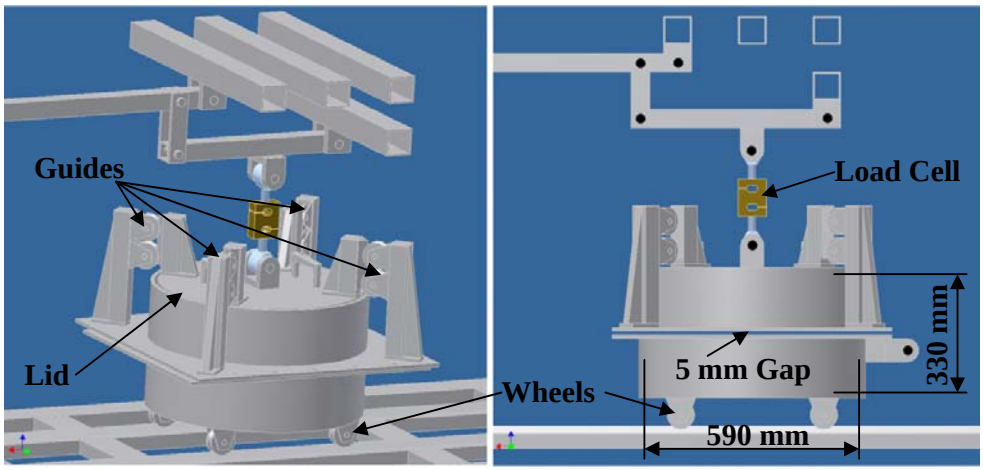

Figure 3.5 - Large Scale Shear Box Detail

Linkage Mechanism

The linkage mechanism that is used to apply the normal load on the sample in the container works on the leverage principle. A weight is attached to the far end of the linkage's long bar. This load is then transferred to the lid through the mechanism. The linkage is designed so that the normal load that the lid experiences is approximately 42 times the load at the end of the bar. The linkage mechanism can be seen in Figure 3.6.

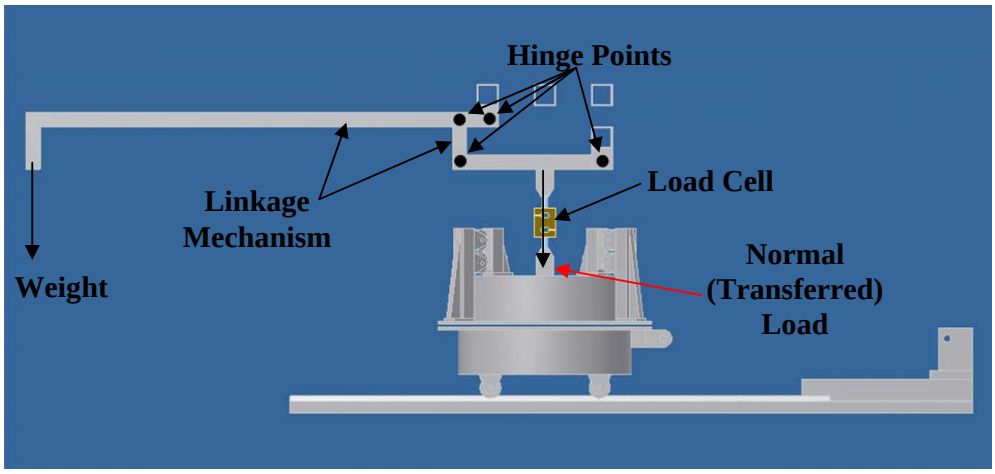

Figure 3.6 - Linkage Mechanism Details

It should be noted that the weight of the linkage itself, as well as the lid, also contributes to the normal load on the sample. By hanging a weight (and incrementally adding one) at the end of the linkage, the normal load is increased. For this project 10 kg weights were used. The number of weights was increased to a maximum of four (40 kg) for the confined compression test (Section 3.4) and a maximum of three (30 kg) for the direct shear test. In Table 3.1 the average induced normal stress on the sample for each weight is summarised. Here the

effect of the mass of the lid itself is included. These normal stresses were implemented directly in the DEM simulations of the respective tests.

Table 3.1 - Induced Normal Stress Values for Different Weight Loads

	Description	Stress (kPa)	Used in
Load 1	Linkage and Lid	10.5	CCT & DST
Load 2	Linkage, Lid + 10 kg	24.0	CCT & DST
Load 3	Linkage, Lid + 20 kg	38.3	CCT & DST
Load 4	Linkage, Lid + 30 kg	52.4	CCT & DST
Load 5	Linkage, Lid + 40 kg	65.6	CCT

The calibration process for this project was developed with an anchor pull validation test taken into account (as in Chapter 5), since bulk material calibration parameters are application specific. The range of normal stresses as in Table 3.1 was therefore derived so that it is within the same range as the induced local stresses brought about by the anchor during the anchor pull test.

Hydraulic Actuation and Control

The horizontal displacement of the bottom half of the container is provided by a hydraulic actuator. The layout of the general design implies that the actuator pulls the bottom half to ensure that the load cell only experiences tension. In the case of the conventional Jenike Shear Tester, it also allows for the self-alignment of the tester (Carson and Wilms, 2005). To provide the constant shear velocity needed for the direct shear test, the motion of the cylinder is controlled by means of a PID controller on a PLC interface. The horizontal displacement of the bottom half was used as the feedback parameter in the control strategy. Through this control, a constant shear velocity of 1 mm/s was applied over a total shear distance of 70 mm. The connection of the bottom half to the hydraulic actuator, as well as the general actuation and control set-up, can be seen in Figure 3.7.

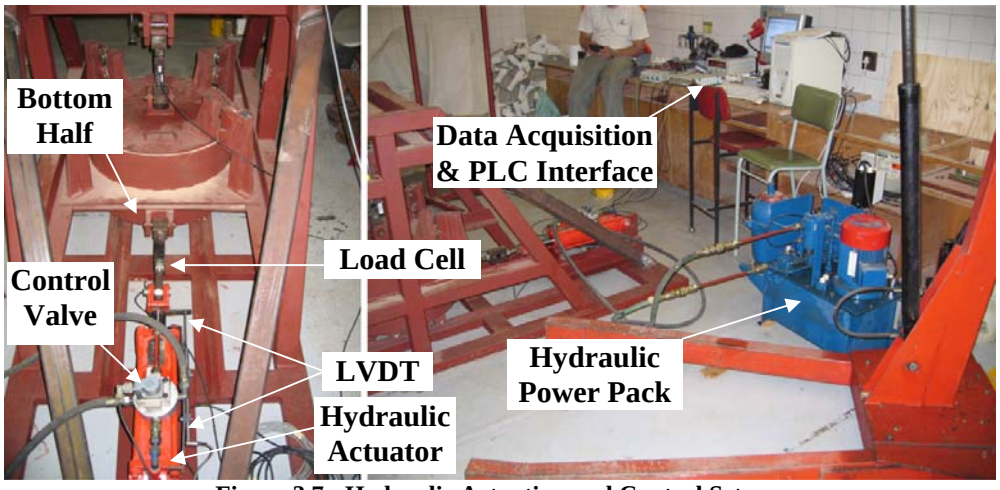

Figure 3.7 - Hydraulic Actuation and Control Set-up

Data Acquisition

Both the normal and shear loads on the sample were recorded with HBM S9 50 kN load cells. The vertical displacement of the lid, as well as the horizontal displacement of the bottom half, was recorded with an HBM WA L linear variable differential transducer (LVDT). All four of these sensors were connected to an HBM Spider8 datalogger and the data acquisition was performed by means of the HBM Catman software (at a sampling frequency of 50 Hz).

3.3.2 Conducting the DST

General Preparation

Prior to the direct shear test the container is carefully filled with the bulk material under investigation. The filling method used for this project entailed filling the container layer by layer (using a steel bucket), each time levelling the packing. No compaction was performed. When the container is filled to its brim and the final levelling done, the sample height is measured and the lid carefully placed on top of the sample. Care should be taken when placing the lid in order to minimise any unnecessary compaction effects.

With the lid in place the load cell and vertical displacement LVDT are attached to the lid (Figure 3.8). This is done by slowly lowering the linkage (with the weights, if present) until the sensors can be connected to the lid. At this point the linkage is kept stationary and the sensors connected to the data acquisition interface and the load cell zeroed. Then the linkage is very slowly lowered further to rest under its own mass on the lid via the load cell. At this point the LVDT is also zeroed and the sample height measured again. Following these steps enables the load cell reading to represent the normal load on the sample due to the linkage mechanism (and additional weights, when added). In further data processing the weight of the lid on the sample is added to this reading. Any displacements of the lid during the DST will also be recorded by the LVDT in order to observe the dilation and contraction of the sample. Tilting of the lid during the DST can be observed (Härtl and Ooi, 2008), but this was not investigated in this project. To minimise any excessive tilting effects, the lid guides were incorporated in the design (Figure 3.5), hence only one LVDT was necessary for the measurement of lid displacement.

The rod of the hydraulic cylinder (with the second load cell attached to the clevis) is slowly extended until the load cell can also be connected to the bottom half of the container. The second LVDT, which is fixed to the hydraulic cylinder body, is then also connected to the clevis (Figure 3.7). Both of these sensors are then zeroed.

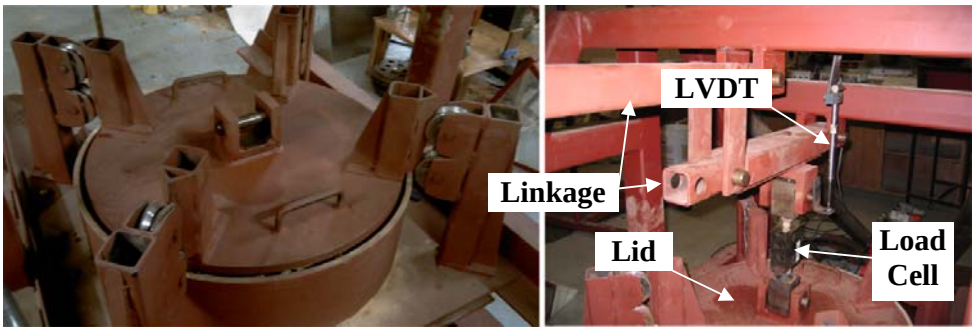

Figure 3.8 - Lid on Packing and Connected to Load Cell and LVDT

Performing a Test Run

Using the PID and PLC interface, the hydraulic cylinder is retracted at a horizontal velocity of 1 mm/s over a distance of 70 mm. This action pulls the bottom half of the container towards the hydraulic cylinder, thus inducing the shear effect in the bulk material while the data is recorded. The displacement of the bottom half and lid after the test can be seen in Figure 3.9.

Figure 3.9 - Bottom Half and Lid Displacement After Direct Shear Test

When the test run is finished, the lid is removed and the bottom half pushed back to its original position, so that it is lined up with the top half again. The sample is mixed to loosen it up and to prepare it for the next test run (Figure 3.10). The preparation steps are then repeated, with different weights at the end of the linkage and another test is run. Four such test runs are performed to constitute a complete DST. For a material batch, three DST's are conducted to ensure repeatability (as discussed in Chapter 4).

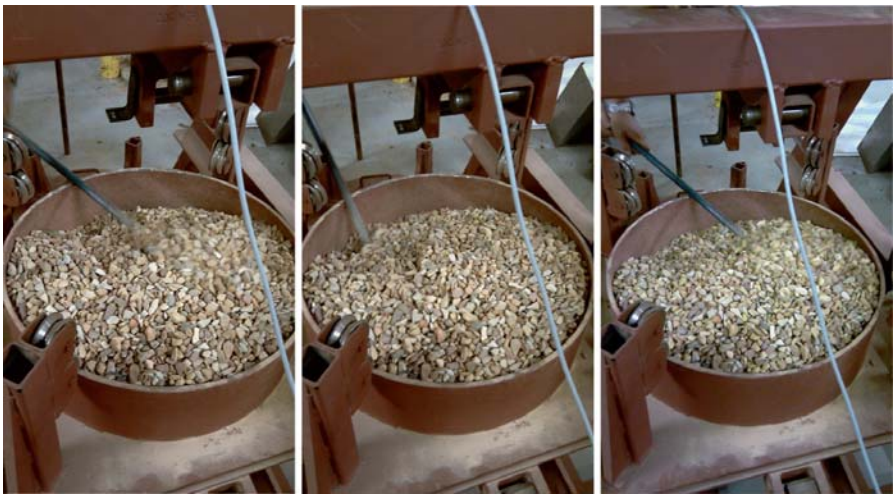

Figure 3.10 - Sample Being Mixed

Data Processing Considerations

The data recorded with the four sensors are used to determine the bulk shear and normal stresses, along with the subsequent bulk shear and normal strains. The derivation of the normal and shear stresses in the sample is discussed below.

From the general layout of the system it is clear that, in theory, as the bottom half moves it attempts to shear the sample in half along the ideal shear line (the horizontal shear plane). The fixed top half attempts to restrict the sample from moving along with the bottom half, effectively shearing the sample in the opposite direction. The lid, linkage and weights apply a normal load on the sample. The total normal load that the sample experiences is determined as follows:

$$F_n = F_n^{recorded} + F_l \tag{3.3}$$

Here, $F_n^{recorded}$ is the reading of the load cell that measures the normal load on the sample due to the linkage mechanism and weights. F_l is the load on the sample as applied by the lid's weight. The actual shear load that the sample experiences is determined as follows:

$$F_s = F_s^{recorded} - F_{rf} \tag{3.4}$$

where $F_s^{recorded}$ is the reading of the load cell that measures the shear load on the sample as induced by the displacement of the hydraulic cylinder. F_{rf} is the friction force due to the rolling friction of the wheels as they move on the tracks during the shear displacement. This rolling friction force is determined as follows:

$$F_{rf} = \mu_{rf}(F_n + F_{bh} + F_m) \tag{3.5}$$

Here, F_m is the weight of the bulk material in the container and F_{bh} is the load on the tracks of the bottom half of the container. It should again be noted that the top half is fixed to the frame of the set-up and is therefore not considered. It was assumed that the interface between the material and the container walls is frictionless (to simplify the experimental data processing). In Equation 3.5, μ_{rf} is the estimated rolling friction coefficient for the steel castor wheels on the tracks during movement. The estimation of the rolling friction coefficient is discussed in more detail in Appendix B. It should also be noted that F_l and F_{bh} are both constant, while F_m remains constant for a specific test run. The cross-sectional area, A, of the container is used to determine the induced shear stress, σ_s, and normal stress, σ_n, in the sample:

$$\sigma_n = \frac{F_n}{A} \tag{3.6}$$

$$\sigma_s = \frac{F_s}{A} \tag{3.7}$$

Data and Results Representation

The normal strain, ε_n, as a function of the shear strain, ε_s, that the sample undergoes can be seen in Figure 3.11. As the shear strain develops, the sample experiences an initial inter-particle collapse and bulk contraction, typically over the first 4% to 6% shear strain. After that the sample dilates again in a largely linear fashion as the shear strain increases.

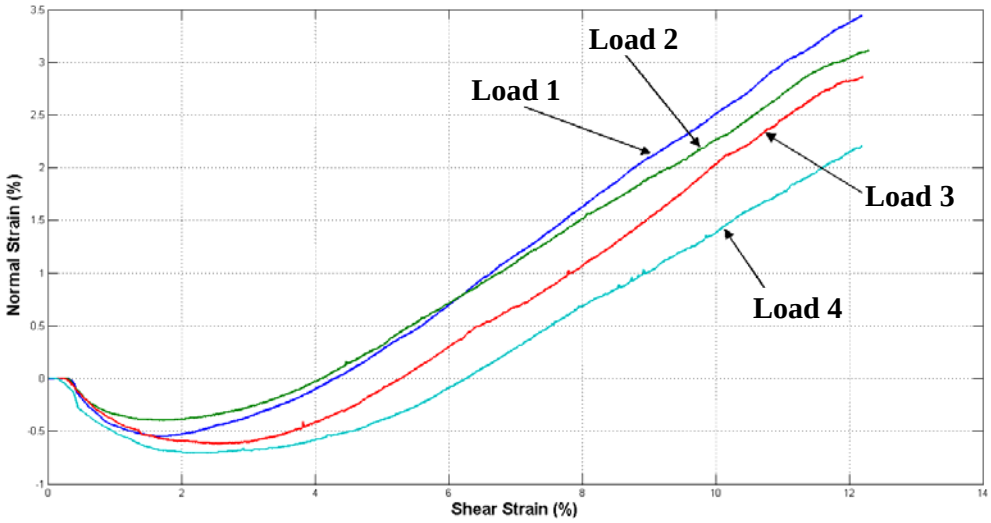

Figure 3.11 - Bulk Normal Strain in the Sample for Different Normal Loads

For the lowest normal load, the sample shows a more dilative behaviour. As the normal load increases, the sample shows a larger degree of contraction prior to dilation. Yan (2008a) recorded a similar behaviour. This behaviour can be attributed to the tendency of the particles to be crushed during shear under high

normal loads. When crushing (or particle breakage) occurs, more inter-particle collapse takes place, resulting in the sample to contract more. Under lower normal loads, particle interlocking occurs more readily as opposed to particle breakage. This ultimately causes the sample to dilate more during the shear action (Lee *et al.* 2008).

The typical normal stress on the sample, for different normal loads, as a function of the shear strain can be seen in Figure 3.12.

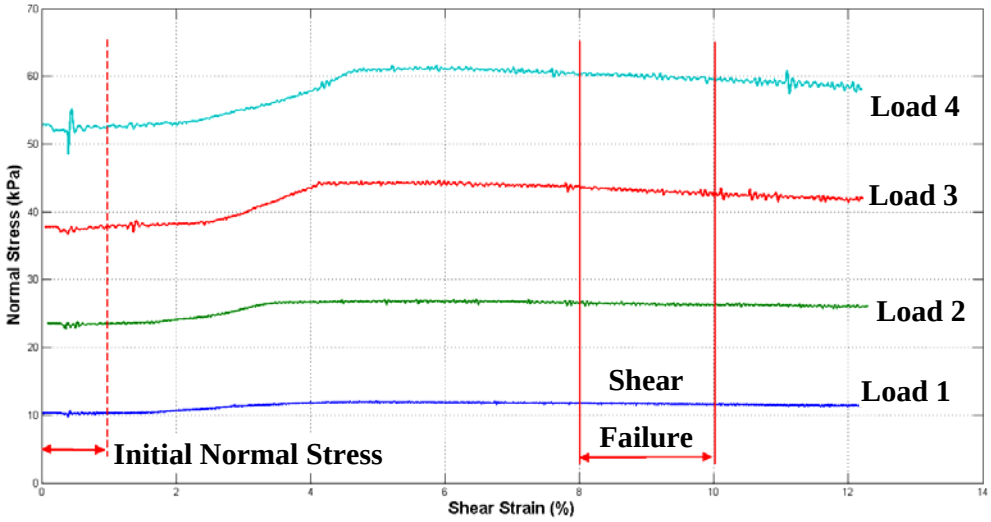

Figure 3.12 - Bulk Normal Stress in the Sample for Different Normal Loads

The initial normal stresses induced in the samples (by the linkage mechanism, weights and lid) are visible in the early development of the shear strain (between 0% and 1% shear strain). From 1% to 5% shear strain the normal stress increases. It is clear that this increase becomes larger as the initial normal load increases. This behaviour is not generally expected since the lid and linkage mechanism apply a dead load on the sample. However, as the shear strain develops, the lid displaces due to the dilatancy effect of the material. The region of the increase in normal stress corresponds with that of the initial normal contraction of the sample (as seen in Figure 3.11).

After approximately 5% shear strain, the normal stress stabilises for the rest of the shear strain evolution. This corresponds with the linear dilation of the sample in the vertical direction. For higher normal loads however, the normal stress shows a slight decrease as the shear strain develops. In this region the lid experiences an upward displacement as the sample dilates during shear strain progression.

The shear stresses induced in the sample for the different normal loads can be seen in Figure 3.13. As the shear strain develops, the shear stresses increase gradually until a peak (residual or limiting) region is reached, typically between 8% and 10% shear strain. At this region the sample is said to have undergone

shear failure (Härtl and Ooi, 2008). It can also be observed that the peak shear stresses increase with an increase in the normal load on the sample, which illustrates the stress dependency of bulk materials clearly.

In general it is expected that a well defined peak stress will be observed as the normal load increases, as seen in Figure 3.2a, since a higher normal stress will ultimately result in a denser packing. However, this expected behaviour is applicable to finer materials such as sand, soils and powders that are fundamentally more dense than coarse aggregate, due to their low voids ratios (Head, 1988). Even at high normal loads, coarse aggregates will not show the same levels of porosity and voids ratio as finer materials. Thus the general shear stress behaviour of the material tested in this project will not show a distinctive peak stress but rather a residual stress, even at increasing normal loads. Lee *et al.* (2008) also found this behaviour after direct shear tests were conducted on coarse aggregates.

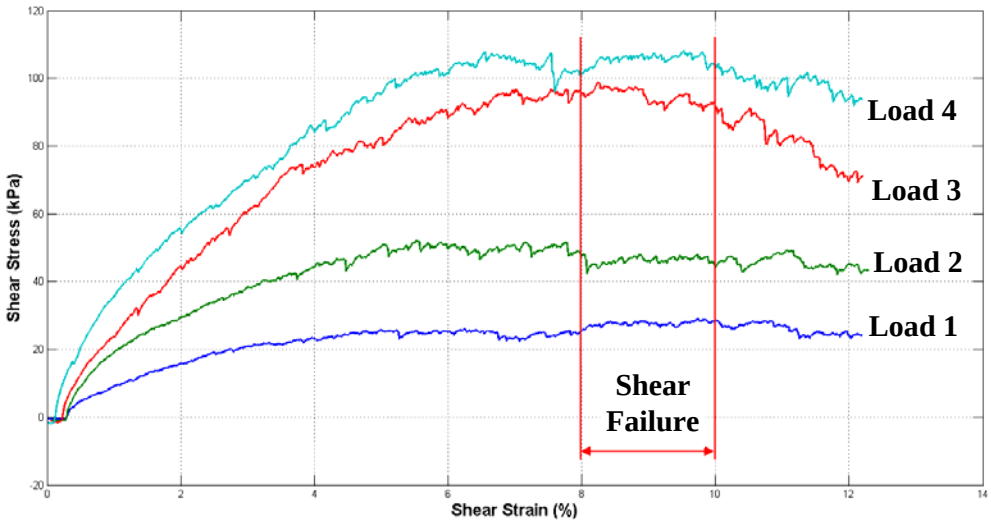

Figure 3.13 - Bulk Shear Stress in the Sample for Different Normal Loads

Since the residual shear stress region appears to be between 8% and 10% shear strain, the average of the shear stresses within this region is calculated for each of the four normal load cases, in order to obtain the shear stresses at failure. The same is done for the normal stresses on the sample (Figure 3.12). The four average residual shear stresses are plotted against their respective normal stresses, as shown in Figure 3.14, to obtain the shear envelope for the sample.

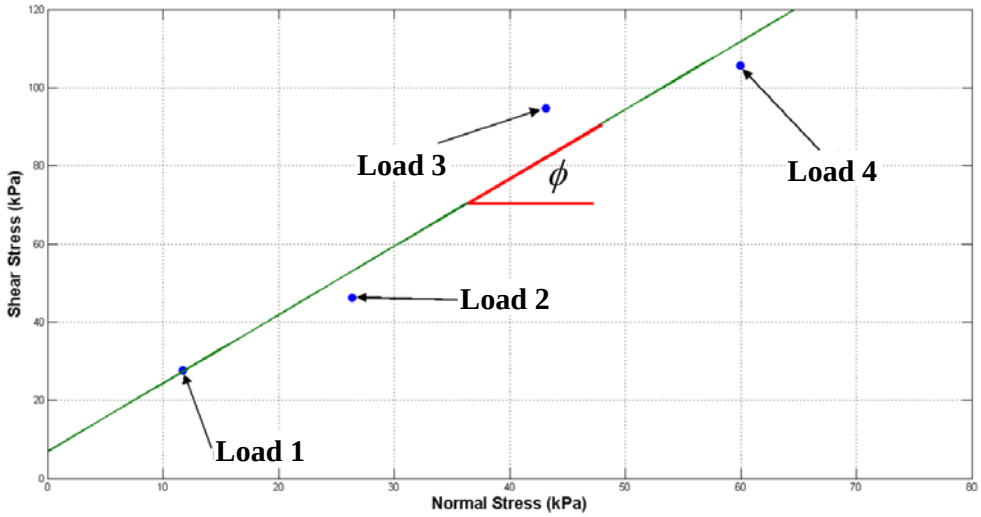

Figure 3.14 - Experimental Shear Envelope

Compared to the theoretical expectation, it can be seen that the data points do exhibit an approximated linear relation between the shear and normal stresses. The gradient of the fitted line is then used to calculate the internal friction angle, ϕ, of the sample using Equation 3.2.

In Figure 3.15 the normal displacement of the lid, d_n, is also plotted against the shear displacement of the bottom half of the container, d_s. This yields a similarly shaped graph as in Figure 3.11, showing displacements instead of strains.

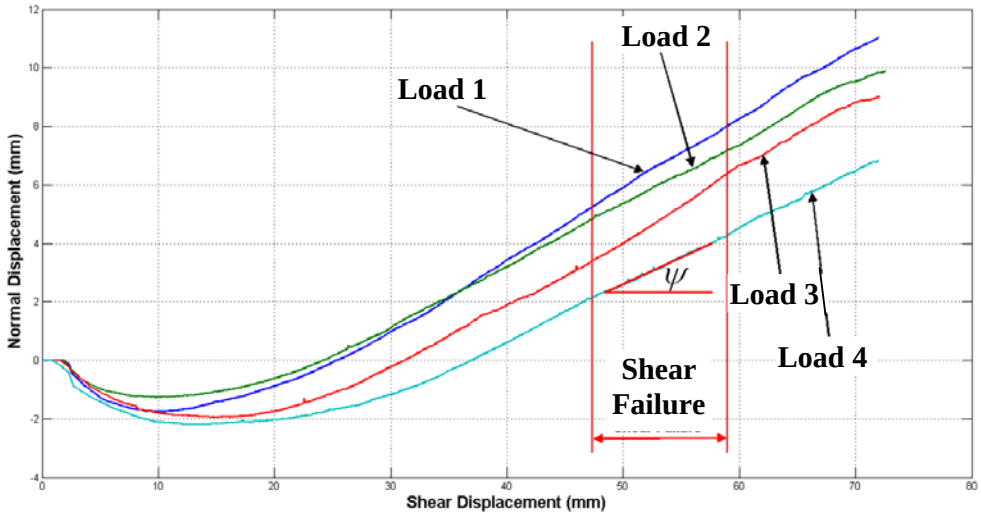

Figure 3.15 - Lid Displacement versus Bottom Half Displacement

The gradient of the graph between 8% and 10% shear strain (that is, between 47.2 mm and 59 mm shear displacement) was taken to determine the angle of dilatancy, ψ (Equation 3.8), according to the discussions by Alejano and Alonso

(2005). The angle of dilatancy is used as an additional bulk property to evaluate the calibration results (see Chapter 4).

$$\psi = \tan^{-1}\left(\frac{d_n}{d_s}\right) \tag{3.8}$$

Additional tests were performed to investigate the effect of the shear velocity and the starting position of the bottom half on the internal friction angle. These tests are discussed in more detail in Appendix C. It was found that no significant effects were induced by these changes in the DST set-up. The abovementioned test parameters and procedures for the DST were thus deemed appropriate for this project.

3.4 The Confined Compression Test

The macro stiffness (or bulk elasticity) characteristics of a packing of bulk material can be obtained in the form of the confined Young's Modulus which is derived from the results of the so-called confined compression test (also referred to as the CCT). Another bulk parameter that indicates the stiffness characteristics of a packing is the bulk stiffness and can be directly related to the confined Young's Modulus.

The large scale shear box was designed to enable the CCT to also be performed with the same test set-up. This allows for the overall experimental procedure to be executed more effectively. In this section a brief background into the CCT is discussed along with how it was implemented in the context of the large scale shear box set-up for this project.

3.4.1 Theoretical Background

A typical CCT consists of a bulk material sample that is contained in a cylindrical container. A lid is then placed on top of the sample in the container to apply a normal load on it, in the vertical direction. A schematic of the set-up can be seen in Figure 3.16. The set-up does not allow for the sample to undergo any bulk lateral strains (in the *x*- and *y*-directions). Only a bulk longitudinal strain is experienced due to the normal load.

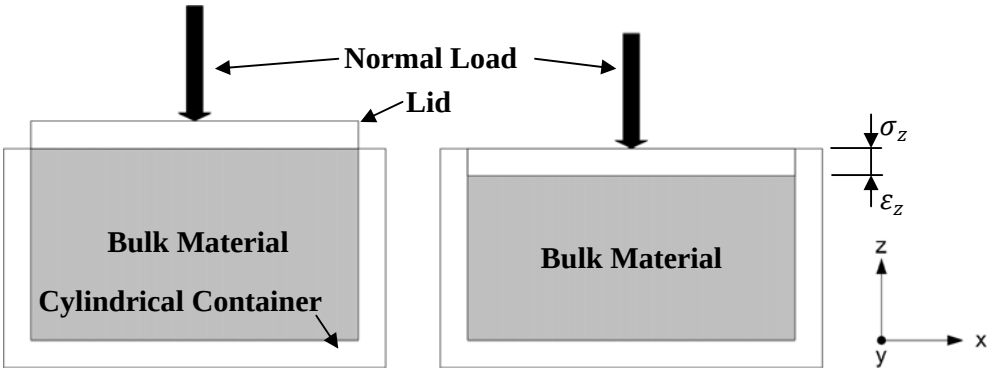

Figure 3.16 - Confined Compression Test Schematic

If the bulk material is approximated as an isotropic medium, after which it is subjected to a uniform compression, the confined Young's Modulus (also known as the bulk modulus) is defined as follows:

$$E' = E\left(\frac{1-\upsilon}{(1+\upsilon)(1-2\upsilon)}\right) \tag{3.9}$$

where E is the Young's modulus of the material and υ is the Poisson's ratio. Now consider the longitudinal stress in the medium, based on general solid mechanics theory:

$$\sigma_z = \frac{\upsilon E}{(1+\upsilon)(1-2\upsilon)}\left(\varepsilon_x + \varepsilon_y + \varepsilon_z\right) + \frac{E}{1+\upsilon}(\varepsilon_z) \tag{3.10}$$

Since $\varepsilon_x = \varepsilon_y = 0$, Equation 3.10 can be reduced to the following:

$$\sigma_z = E\varepsilon_z\left(\frac{\upsilon}{(1+\upsilon)(1-2\upsilon)} + \frac{1}{1+\upsilon}\right) \tag{3.11}$$

$$\sigma_z = E\varepsilon_z\left(\frac{1-\upsilon}{(1+\upsilon)(1-2\upsilon)}\right) \tag{3.12}$$

By substituting Equation 3.9 into Equation 3.12 it is seen that the confined Young's modulus can be approximated as follows:

$$E' = \frac{\Delta\sigma_z}{\Delta\varepsilon_z} \tag{3.13}$$

The normal load is applied and increased to a certain maximum load, after which it is reduced again to a zero load. This loading (and unloading) process constitutes one compression cycle, which is repeated a number of times (typically two to three times) to complete the CCT. The normal load and resulting normal displacement are recorded and the bulk longitudinal stress and strain (σ_z and ε_z respectively) calculated and plotted, as in Figure 3.17. Using the conventions in Section 3.2, σ_z and ε_z are also represented by σ_n and ε_n respectively.

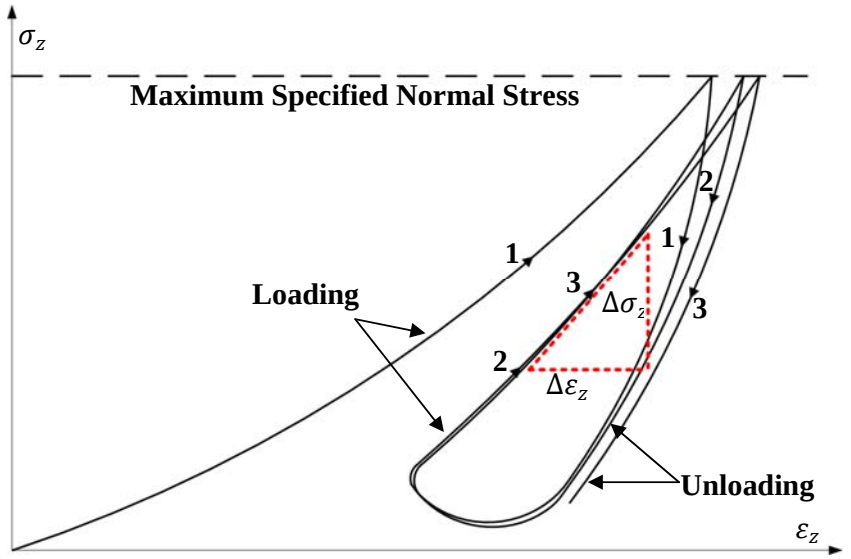

Figure 3.17 - Theoretical Compression Cycles from a Confined Compression Test

As can be seen in Figure 3.17 the first compression cycle does not exhibit the same behaviour as the remaining compression cycles. This is due to the packing not being fully compacted prior to the test and subsequent inter-particle movements taking place. During the subsequent cycles the packing is adequately compacted to allow for a largely linear relation between the stress and strain for the loading part of each cycle. The slopes of each of these loading parts are used to derive the average confined Young's Modulus for the packing (see Equation 3.13 and Figure 3.17).

The average bulk stiffness (k_b) of the packing can be derived from the average confined Young's Modulus by using the initial height of the packing (H) and the cross-sectional area of the container (A),

$$k_b = \frac{A}{H} E' \tag{3.14}$$

The CCT procedure along with the relevant data processing will be discussed in more detail in Section 3.4.2.

3.4.2 Conducting the CCT

When the container of the large scale shear box is filled with the material, using the same filling procedure as for the DST, the packing is carefully levelled and the initial height measured. The lid is then placed on top of the packing. The linkage mechanism is then linked with the lid through the 50 kN load cell and an LVDT. The typical configuration is the same as in Figure 3.8.

The normal load on the sample and the lid displacement for only the lid and linkage mechanism is recorded. Then a 10 kg weight is carefully added to the linkage (see Figure 3.18) after which the normal load and lid displacement is measured again. The load on the linkage is increased in increments of 10 kg until a maximum of 40 kg is reached. This 40 kg weight results in maximum normal stress on the packing of approximately 65.6 kPa, which was implemented directly in PFC^{3D} for the CCT simulations (Chapter 4). Then the weight is decreased in increments of 10 kg until only the linkage is left. This then represents one normal loading and unloading cycle, hence one full compression cycle. This compression cycle is then repeated twice to complete the CCT, taking the necessary recordings at each weight increment. A total of three CCT's are typically performed to ensure repeatability.

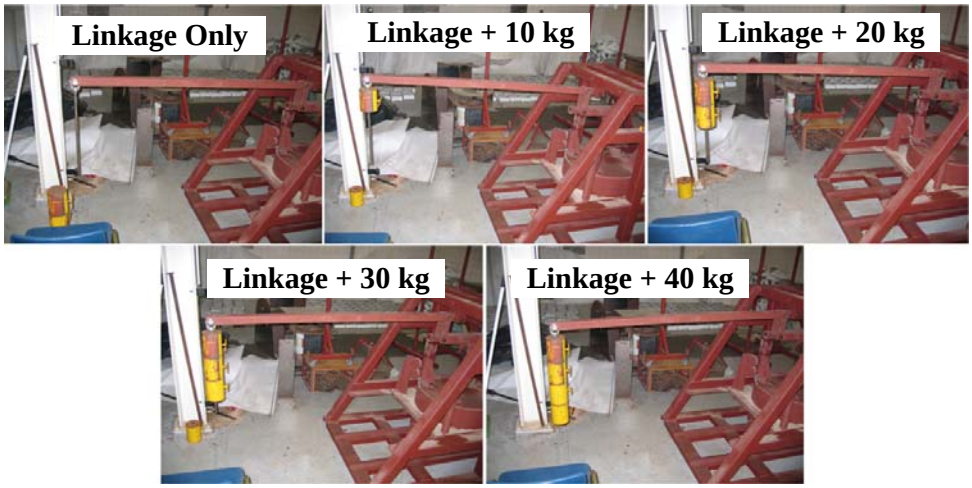

Figure 3.18 - Incremental Increase of Normal Load on Sample

The raw data of the CCT is processed using Matlab to calculate the bulk normal stress (using the cross-sectional area of the container) and the bulk normal strain (using the initial height of the packing). A typical plot of the normal stress versus the normal strain on the packing, for one CCT, can be seen in Figure 3.19. Note the three compression cycles.

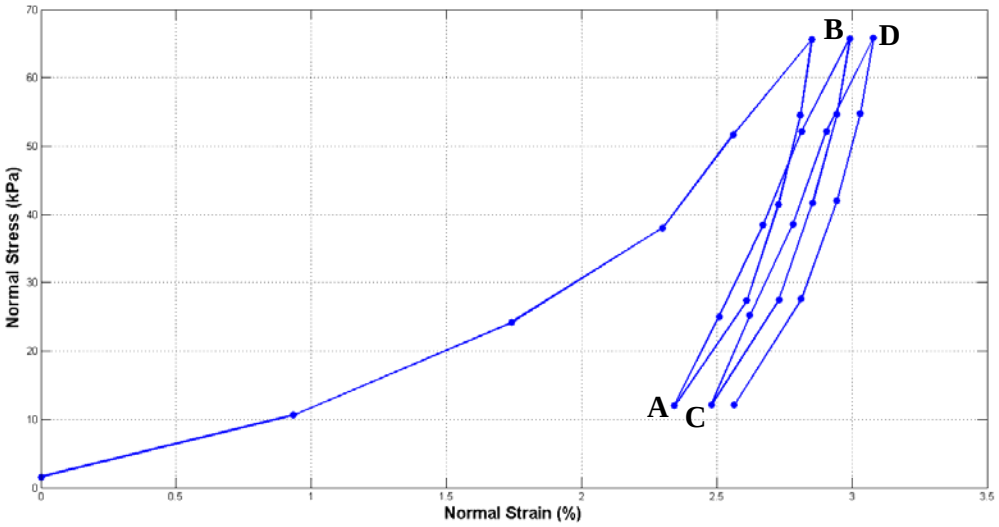

Figure 3.19 - Typical Experimental Compression Cycles for a Confined Compression Test

During the first cycle, as expected, the packing settles and collapses under the normal load (due to inter-particle slip). For the second and third cycles the normal stress shows the desired linear relation to the normal strain (during the loading parts AB and CD).

Using the definitions of the confined Young's Modulus in Section 3.4.1 and Equation 3.13, the confined Young's Modulus for this test is obtained by calculating the average of the gradients for the second and third compression cycles' loading parts (AB and CD). This average, along with the average for the other two CCTs, are used to obtain the average confined Young's Modulus for the bulk material.

The initial height of the packing prior to each CCT, with the lid in place (and no linkage attached to the lid), is used along with the cross-sectional area of the container to obtain the bulk stiffness for that particular CCT (see Equation 3.14) from its confined Young's Modulus. The average of the three estimations are then used as the overall bulk stiffness estimation of the packing.

3.5 Concluding Remarks

To account for the coarse crushed aggregate in this project, the large scale shear box was designed. The large scale shear box set-up was designed to be able to perform the direct shear test as well as the confined compression test. The most prominent bulk material characteristics in this project, in the form of bulk friction and elastic properties, were investigated using these tests and the procedures discussed in this chapter. In the next chapter these experimental results, obtained in the calibration of the DEM micro properties for the coarse aggregate, are discussed in more detail. The integration of the experimental work in the overall calibration procedure is also presented.

4. Bulk Material Calibration Procedure

4.1 Introduction

The DST and CCT procedures presented in Chapter 3, were used as the basis of the calibration procedure. The results obtained from these tests were ultimately replicated in the numerical components of the procedure, in order to calibrate the input parameters.

4.1.1 Experimental Work

The experimental work of the calibration procedure was divided into four categories, namely the direct estimation and initial bulk property categories, followed by the confined compression test and the direct shear test. The procedure is summarised in Figure 4.1.

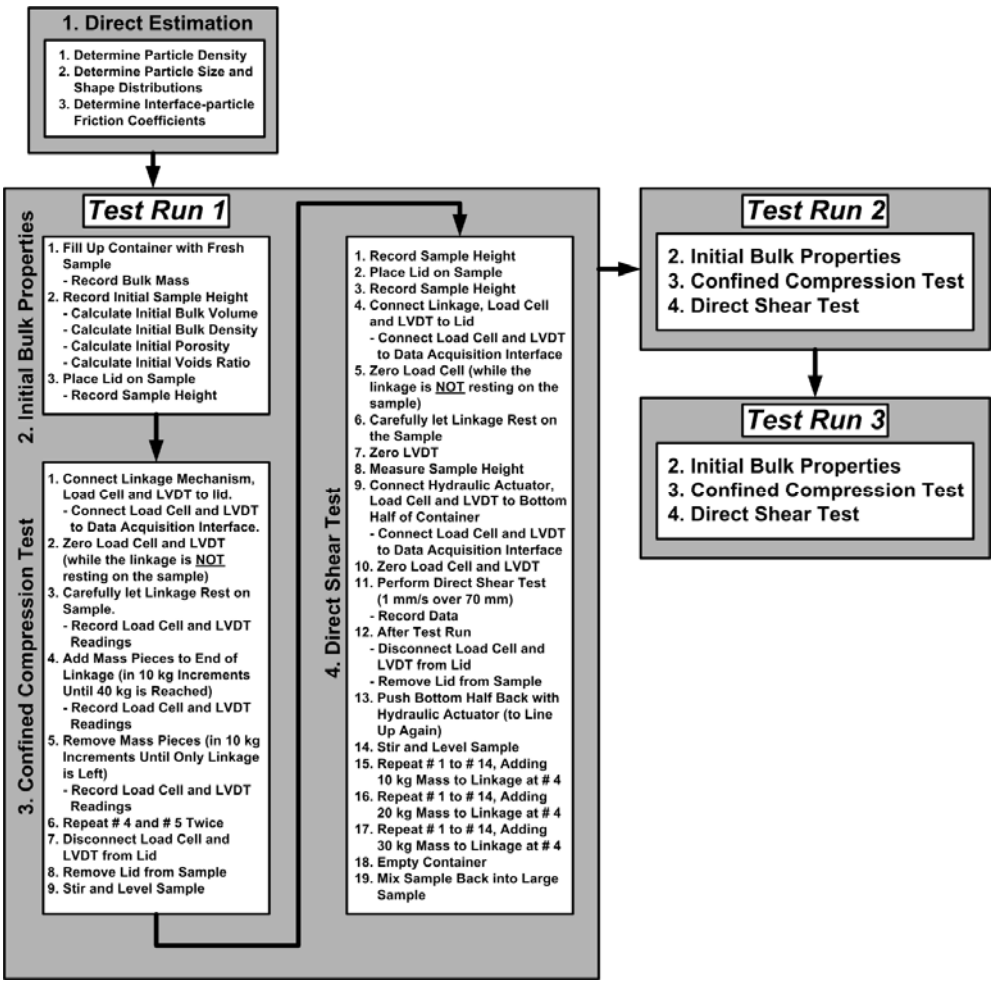

Figure 4.1 - Complete Experimental Procedure

The initial bulk property measurements, as well as the CCT and DST were all conducted in the same session. The large scale shear box has thus been developed as to allow for the bulk density, porosity and voids ratio to be measured before the CCT is conducted. When the CCT was completed, the DST was performed. Allowing for all of the considered bulk properties to be measured in one session ultimately improved the flow of the experimental work for the calibration process. It also facilitated all of the bulk properties to be measured for the same sample, thus eliminating the effect of using different samples during the same session. A second and third session were also performed (with a different sample from the same material batch) to ensure repeatability. The direct estimation category was conducted independently before the primary experiments were conducted. This category entails the measurement of the particle density, ρ_p (an initial estimation, as discussed later in this chapter), particle-wall friction coefficient, μ_{pw}, together with the particle size and shape distribution. The main purpose of the direct estimation category was to obtain these properties for direct input into PFC^{3D} without resorting to an actual iterative calibration process to obtain them. The results obtained from the four categories are summarised in Table 4.1.

Table 4.1 - Results from Experimental Procedures

Category	Property	Use
Direct Estimation	Particle Density, ρ_p	Compare to DEM Results
	Particle Size and Shape Distribution	Direct input to DEM
	Particle-wall Friction Coefficients, μ_{pw}	
Initial Bulk Properties	Initial Bulk Volume, V_b	Compare to DEM Results
	Initial Height, H	
	Bulk Mass, m_b	
	Initial Bulk Density, ρ_b	**Calibrate DEM Particle Density, ρ_p**
	Initial Porosity, n	Compare to DEM Results
	Initial Voids Ratio, e	
CCT	Maximum Normal Stress, σ_n (65.6 kPa)	Direct input to DEM
	Confined Young's Modulus, E'	**Calibrate DEM Particle Stiffness, k_p**
	Bulk Stiffness, k_b	Compare to DEM Results
DST	Load 1, σ_n (10.5 kPa)	Direct input to DEM
	Load 2, σ_n (24.0 kPa)	
	Load 3, σ_n (38.3 kPa)	
	Load 4, σ_n (52.4 kPa)	
	Internal Friction Angle, ϕ	**Calibrate DEM Inter-particle Friction, μ_{pp}**
	Angle of Dilatancy, ψ	Compare to DEM results

The critical bulk parameter obtained from the initial bulk property category is the bulk density, ρ_b, which was used to calibrate the particle density, ρ_p. From the CCT category the confined Young's Modulus, E', was obtained and used to calibrate the particle stiffness, k_p. The internal friction angle, ϕ, was obtained from the DST and used to calibrate the inter-particle friction coefficient, μ_{pp}. The remaining bulk properties (as in Table 4.1) were used for comparison purposes after calibration. System parameters such as the normal stress cases for the CCT and DST were recorded for direct implementation in PFC^{3D}.

4.1.2 Numerical Work

To simulate the bulk properties measured in the experiments, DEM simulation codes for use in PFC^{3D} were developed by means of the FISH programming language. The inputs for these simulations consist of, amongst others, the micro properties that aim to characterise the numerical version of the physical material. These micro properties needed to be calibrated to enable the resulting simulated bulk properties to resemble the experimental bulk properties. This calibration strategy entailed the iterative altering of the micro properties until the simulated bulk property was close enough to its experimental counterpart. This strategy is discussed in more detail in the remainder of this chapter.

The simulation procedure was divided into three categories, the first one being the simulation of the bulk density, porosity and voids ratio (also referred to as the BDPVR simulations). The second category is the simulation of the confined Young's Modulus and bulk stiffness (the CCT simulations) and the third category is the internal friction angle and angle of dilatancy (the DST) simulations. Each category consists of a preparation component, in which the model is prepared for the actual simulation. Then the actual simulation of the applicable bulk property is conducted. Lastly the desired responses for the simulations are extracted for further data processing using Matlab and MS Excel.

The flow of the experimental work was replicated in the flow of the simulations. Firstly the BDPVR simulations were conducted. Then, using the same model, the CCT simulations are performed, followed by the DST simulations. This procedure constitutes the full DEM replication of an experimental test run (Figure 4.1).

4.1.3 The Calibration Procedure

The BDPVR simulations were run to iteratively calibrate the particle density, while the CCT and DST simulations were used to calibrate the particle stiffness and inter-particle friction coefficient respectively. The calibration procedure for this project can be seen in more detail in Figure 4.2. In this figure the incorporation of the experimental procedures and results into the DEM iterations can clearly be seen.

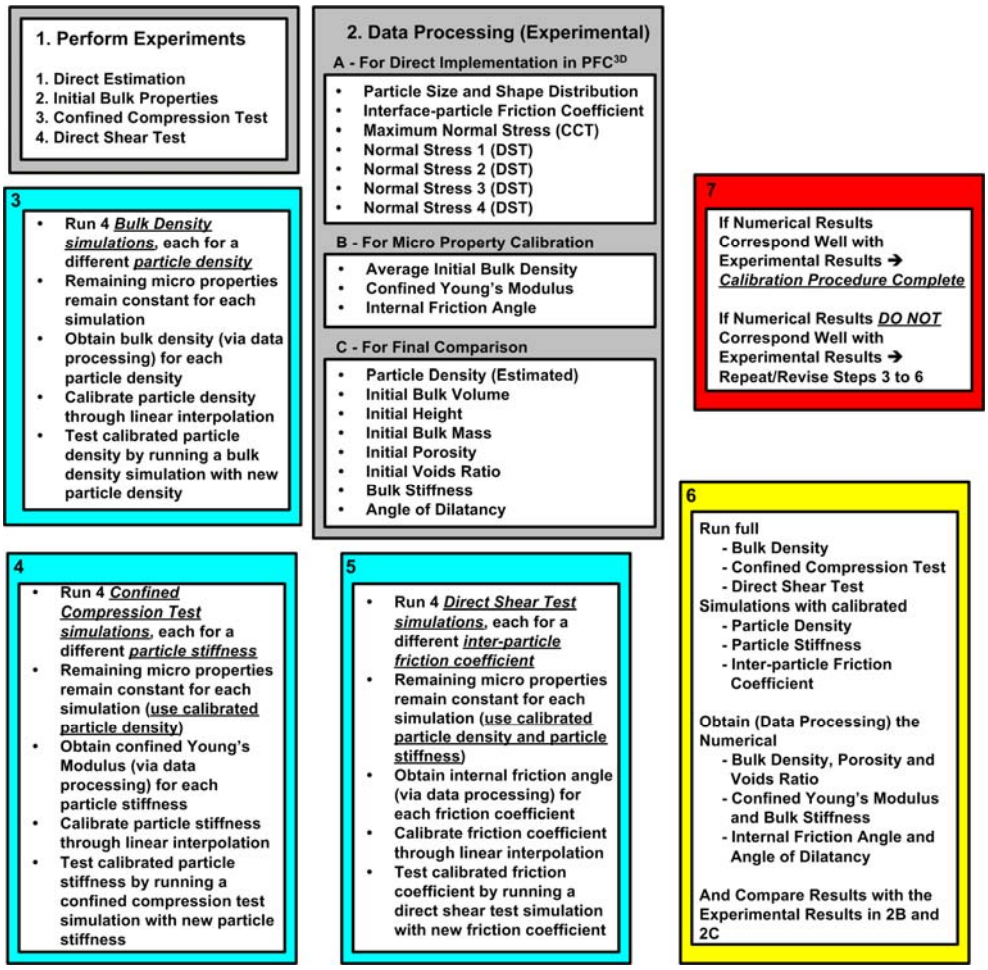

Figure 4.2 - Complete Calibration Procedure Outline

For each of the three iteration steps (3, 4 and 5), all of the other relevant input micro properties were kept constant with only the applicable micro property being varied. When this calibrated property was obtained, the simulation was run again at this new value to evaluate its reliability. If an adequate result was obtained, the next set of iterations was then performed and the entire process repeated for that parameter.

Upon completion of the iterations and their reliability checks, the complete set of calibrated micro properties was used in a final simulation run and all of the subsequent results compared to the experimental results. This ultimately served as the final check to evaluate the calibration procedure's performance. If a good correlation is observed between the experimental and numerical results after this final check, the calibration procedure can be regarded as successful. Otherwise the calibration procedure should be repeated in its entirety, or the process revised, in order to obtain improved results.

In this chapter the abovementioned calibration strategy, as implemented in this project, is comprehensively discussed in the context of its experimental and numerical aspects. The order of the discussions as per section, corresponds with how the calibration strategy was approached and illustrates clearly how the experimental and numerical work were integrated.

4.2 Particle Size and Shape Distribution

Due to time constraints and the unavailability of advanced techniques, the particle size and shape distributions were obtained through visual inspection. In future research more accurate techniques to quantify these properties need to be developed and implemented. To estimate the particle shape and size distribution the following approach was used:

Eight random samples of particles from the larger bulk material sample were collected, with each random sample consisting of three particles. The shape of each particle was visually inspected and recorded. Then the dimensions of each particle were measured according to its shape. Since both the shape and size interpretation are very subjective, it was decided to use a quick inspection and identify a maximum of three shapes in the samples. It was then assumed that those are the only three shapes present in the larger sample, to simplify the interpretation. The particles in the eight random samples were then categorised into these shapes.

The material that was used for this project is a coarse crushed aggregate (rock) from a roller mill with an aperture of 25 mm between the rollers (Dymond, 2007). The three shapes that were identified from this material are a so-called pyramid shape, an elongated shape and a largely spherical shape, as seen in Figure 4.3. After the eight samples' particles were categorised accordingly, the size of each particle was estimated using the particular shape's DEM equivalent. The DEM replication of the particle shapes were done by means of the clump logic in PFC^{3D}. The clump representations of the particle shapes can be seen in Figures 4.3 and 4.4. The implementation of these DEM replications is discussed in more detail in Section 4.5.4.

The elongated particles were represented by two spheres clumped together, while the pyramid shaped particles were represented by four spheres clumped together as shown in Figure 4.4. Where the particle shape was largely spherical, representation by means of a perfect sphere in PFC^{3D} was deemed appropriate.

Figure 4.3 - Particle Shapes with Superimposed Clump Equivalents

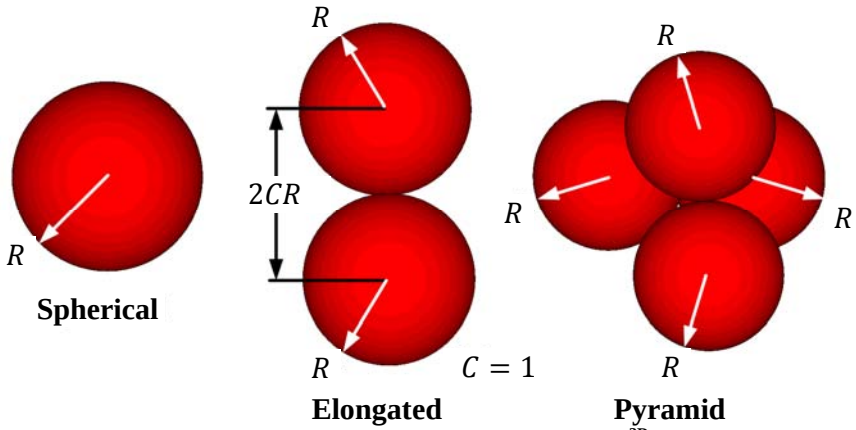

Figure 4.4 - Clumps Implemented in PFC^{3D}

It should be noted that the results from this approach are very subjective. The results therefore only served as a basic indication of the shape and size distribution of the packing from which the equivalent numerical parameters were replicated in PFC^{3D}. Using the abovementioned classification scheme, the size distributions in Table 4.2 were obtained. These size distributions were implemented directly in PFC^{3D} and Gaussian distributions of the radii were generated accordingly (see Section 4.5.4).

Table 4.2 - Size Distributions for Particle Shapes

Shape	R_{min}(mm)	R_{max}(mm)
Pyramid	7.5	10.5
Elongated	12.0	15.0
Spherical	15.0	16.2

It was found that the spherical particles comprised approximately 20.8% of the total sample of 24 pebbles, while the pyramid shape comprised 37.5% and the elongated shape 41.7%. As a simplification, it was thus assumed that the spherical particles take up 20.8% of the total volume occupied by the individual particles in the packing, with pyramid particles occupying 37.5% and the elongated particles 41.7%. Taking this into account the three different shapes were generated in PFC^{3D} according to these percentage volumes in order for them to add up to the total particle volume of 100%.

These particles were then settled under gravity and then levelled during the initial bulk property (BDPVR) simulations, as seen in Section 4.5.4. After levelling, the number of particles for the different shapes is as follows:

Table 4.3 - Particle Numbers After Levelling

Shape	# of Spheres	# of Clumps (Particles)
Pyramid	7 996	1 999
Elongated	1 454	727
Spherical	935	935
Total	**10 385**	**3 661**

Further considerations for the implementation of the particle size and shape distribution in the numerical work for this project are discussed in Section 4.5.4.

4.3 Particle-wall Friction Coefficient

Apart from the friction coefficient that describes the frictional behaviour between the individual particles in a packing (μ_{pp}), an additional friction coefficient was also needed to account for the interaction between the particles and the interfaces that they come into contact with (μ_{pw}). A basic experimental procedure was devised to estimate this particle-wall friction coefficient. For each interface material in this project a particle-wall friction coefficient was determined. The coefficients were then implemented directly in the applicable DEM simulations. In this section the experimental procedure is briefly discussed, together with the results obtained for the different interfaces.

The experiment consists of a particle that is placed on a flat surface of the interface material. The surface is then carefully tilted while the inclination angle is observed with a digital protractor. The angle at which the particle starts to slide down the surface is then recorded. The set-up for a particle-bare mild steel interface can be seen in Figure 4.5. The sliding angle, γ, is then used to calculate the particle-wall friction coefficient, μ_{pw}, for the particular material-interface combination,

$$\mu_{pw} = \tan\gamma \tag{4.1}$$

Figure 4.5 - Experimental Set-up for Particle-wall Friction Coefficient

For each material-interface combination ten measurements were taken for the sliding angle and the average determined from which the particular particle-wall friction coefficient was estimated.

It should be noted that this technique provided a very basic estimation of the particle-wall friction coefficient. A more robust method would be to measure the particle-wall friction angle and to derive the friction coefficient from that, using a modified version of the direct shear test set-up, as described in Section 3.2. Using this alternative method the particle-wall friction coefficient can be iteratively obtained in DEM from the experimental results. Since a normal load is applied to the material in this test, any stress dependencies of the results will be accounted for and more reliable results should be obtained. However, due to time constraints the particle-wall friction coefficients could not be derived using this approach and the basic procedure was used instead.

Five interface materials were considered for this project. For the large scale shear box the interface material was mild steel, coated with a primer to prevent excessive corrosion. This was the interface material applicable during calibration. Bare mild steel, plywood, rubber and plastic were the four remaining interface materials and were applicable in the verification experiments (Chapter 5). The particle-wall friction coefficients for the five materials were estimated and are summarised in Table 4.4. These coefficients were implemented directly in PFC^{3D} for their respective applications.

Table 4.4 - Particle-wall Friction Coefficient Estimations

Interface Material	γ (°)	μ_{pw}	Application
Plastic	33.9	0.67	Angle of Repose
Rubber	38.1	0.78	Anchor Pull
Plywood	40.6	0.86	Angle of Repose
Bare Mild Steel	28.4	0.54	Anchor Pull
Coated Mild Steel	31.7	0.62	CCT and DST

4.4 Damping and Wall Stiffness Characteristics

4.4.1 Damping Characteristics

In the linear contact model in PFC^{3D}, damping can be implemented in the form of local non-viscous damping and viscous damping, or a combination thereof. Other forms of damping can be implemented by means of more complex contact models. Itasca (2003) suggests that local non-viscous damping is inappropriate for systems where large numbers of particles are driven by specified velocity boundary conditions. Since the simulations developed for this project mostly entail moving wall boundaries (especially for the CCT and DST simulations), the local damping coefficients were set to zero and viscous damping used instead. This resulted in a more realistic energy dissipation.

In general, viscous damping is characterised by the critical damping ratio, ξ (Itasca, 2003). This critical damping ratio is specified in PFC^{3D}, in both the normal and shear directions. When $\xi = 1$, the system is said to be critically damped. For $\xi < 1$ the system is under damped, while for $\xi > 1$ the system is over damped. When handling the crushed aggregate samples, it was clearly observed that the particles exhibit a fairly high degree of damping. It was therefore assumed that the particles are slightly under damped, and the critical damping ratio was chosen to be 0.8 and implemented directly in PFC^{3D}. In future research more attention must be focussed on damping calibration.

4.4.2 Wall Stiffness

It was assumed that the wall stiffness, k_w, does not have a significant influence on the results for this project. A wall stiffness value was used that is larger than the anticipated particle stiffness values, with at most one order of magnitude, to ensure largely rigid interface walls. The value that was chosen for the wall stiffness is 10 MN/m and was implemented directly in PFC^{3D} for all of the simulations (in both the normal and shear directions).

4.5 Particle Density, Bulk Density, Porosity and Voids Ratio

The bulk density, porosity and voids ratio of a packing were used to determine the density of the particles as well as the accuracy of the obtained particle size and shape. These parameters could also be used to ensure consistent initial compaction characteristics for a packing prior to performing other tests, such as the CCT and DST. In this section the bulk density, porosity and voids ratio are discussed in the context of how they were applied to this project. A brief background into the concepts is given, as well as how they were obtained experimentally. This is then followed by a discussion of how these parameters were simulated in PFC^{3D} and ultimately used to iteratively calibrate the particle density.

4.5.1 Background

The bulk density can generally be defined as the mass of a bulk material sample divided by the bulk volume that the sample occupies (Head, 1989). The bulk volume also includes the voids and gaps between the particles. The bulk density is typically determined by filling a container of a known shape (for example cylindrical) with a bulk material up to a specified height (see Figure 4.6 for a two-dimensional container with a floor area of one unit). The bulk mass of the material that is placed in the container (m_b) is recorded and used, along with the specified height (which is used to obtain the bulk volume, V_b) to determine the bulk density, ρ_b (Equation 4.2).

$$\rho_b = \frac{m_b}{V_b} \tag{4.2}$$

As can be gathered from the abovementioned explanation, the particle density and the bulk density are not the same property, since the bulk volume includes the gaps between the particles while the particle density is determined using the volume occupied by the particles alone.

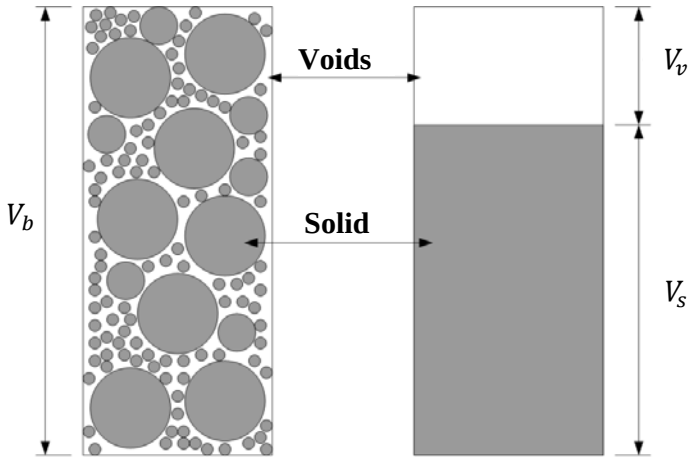

Figure 4.6 - Bulk Volume, Voids Volume and Total Solid Volume (Head, 1989)

According to Head (1989) the voids ratio, e, is defined as the ratio of the voids volume, V_v (that is the total volume of the gaps between the particles for a certain bulk volume), to the total solid volume, V_s, that the particles occupy alone within that same bulk volume (see Figure 4.6 and Equation 4.3).

$$e = \frac{V_v}{V_s} \tag{4.3}$$

The total solid volume is determined by placing the entire sample in water to obtain the displaced volume (and thus the total solid volume). In most cases however, it is rather cumbersome to determine the voids volume. It is also not always practical to submerge the entire sample in water to obtain the solid

volume. To overcome this, the voids ratio can also be calculated using the particle density together with the bulk density, as in Equation 4.4. A basic technique to estimate particle density, ρ_p, is discussed later in this section.

$$e = \frac{\rho_p}{\rho_b} - 1 \tag{4.4}$$

If the porosity, n, is known, the voids ratio can also be determined as follows:

$$e = \frac{n}{n-1} \tag{4.5}$$

The porosity, n, is defined in Head (1989) as the ratio of the voids volume to the bulk volume and is expressed as a percentage,

$$n = 100\left(\frac{V_v}{V_b}\right) \tag{4.6}$$

In cases where it is impractical to measure the voids volume, the voids ratio can be used to determine the porosity,

$$n = 100\left(\frac{e}{e+1}\right) \tag{4.7}$$

In the experimental work for this project the material was placed into a cylindrical container (the container of the large scale shear box). The bulk mass and initial filled height was used to determine an initial bulk density as in Equation 4.2. This was then used along with the particle density to calculate the initial voids ratio according to Equation 4.4. Then the initial porosity was calculated with Equation 4.7.

4.5.2 Experimental Procedures: Particle Density

The procedure to directly estimate the average particle density entails simply dividing the mass of a small sample of pebbles, m_s, by the volume of water, V_d, it displaces (see Equation 4.8). The size of the sample was chosen so that the mass is between 500 g and 1 000 g. This enabled a proper volume of water to be displaced.

$$\rho_p = \frac{m_s}{V_d} \tag{4.8}$$

The sample mass was measured with an electronic scale after which the same sample was placed in a measuring cylinder filled with water. The volume of the displaced water was recorded and, after the relevant data processing, the average particle density for that sample was calculated. It was assumed that the particles did not absorb any water during the short time the experiment was conducted. This procedure was repeated for ten samples and the resulting average determined

to obtain a more reliable indication of the particle density. The basic procedure for the experiment can be seen in Figure 4.7.

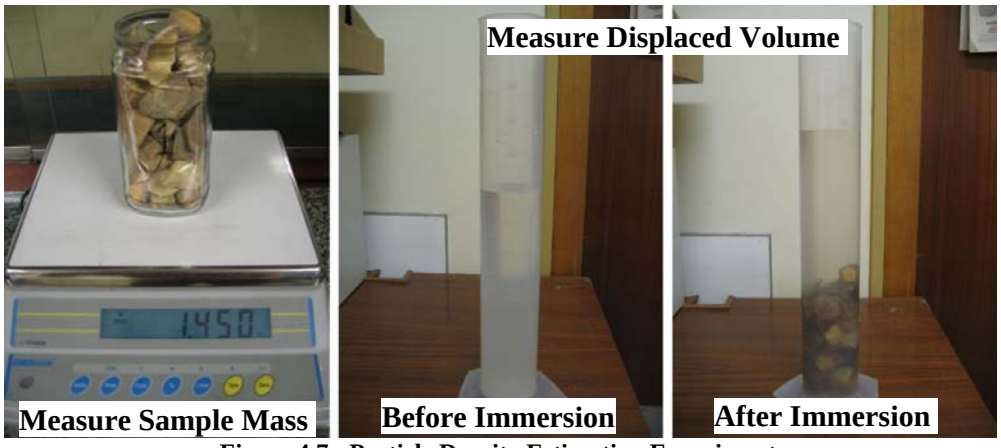

Figure 4.7 - Particle Density Estimation Experiment

With this direct estimation, an average particle density of approximately 2 586.5 kg/m^3 was obtained. This value was used as a comparison against the calibrated particle density, which is discussed in more detail in Section 4.5.4. It was also used to calculate the experimental voids ratio as per Equation 4.4.

4.5.3 Experimental Procedures: Bulk Density, Porosity and Voids Ratio

After lining the top and bottom half of the large scale shear box's container, it was carefully filled to its brim with the crushed aggregate. This was done by filling a steel bucket with the material, weighing the material, and then carefully pouring it into the container to enable a loosely compacted filling. These steps were repeated until the shear box was completely filled (Figure 4.8). The total mass of the material poured into the container was recorded as the bulk mass.

When the container was filled, the material was carefully levelled after which the initial height of the sample was manually measured and recorded. This initial height is defined as how deep the container is filled, measured from the bottom of the container. The lid was then carefully placed on top of the sample and further preparations done for the next step in the overall experimental procedure, the CCT.

Figure 4.8 - Filling of the Large Scale Shear Box

The total mass and the initial height of the sample were used to calculate the bulk volume and bulk density of the packing. Additionally, the directly estimated particle density was used to calculate the voids ratio, after which the porosity was also calculated (refer to Equations 4.2, 4.4 and 4.7). For the three overall experimental test runs concerning the crushed aggregate in this project, the initial bulk properties are as follows:

Table 4.5 - Initial Bulk Properties (Experimental)

	Run 1	Run 2	Run 3	Average
Total Mass (kg)	126.8	124.8	125.8	**125.8**
Initial Sample Height (m)	0.329	0.330	0.330	**0.329**
Bulk Volume (m^3)	0.090	0.090	0.090	**0.090**
Bulk Density (kg/m^3)	1 412.0	1 383.6	1 397.8	**1 397.8**
Porosity (%)	45.4	46.5	45.9	**45.9**
Voids Ratio	0.83	0.87	0.85	**0.85**

The average bulk density was used to calibrate the DEM particle density (see Section 4.5.4). The remaining initial bulk properties in Table 4.5 were compared to their DEM counterparts, as simulated with the calibrated micro properties, as a final check for calibration accuracy.

4.5.4 Numerical Procedures

The BDPVR simulations formed the first part of the simulations and were divided into three distinctive parts, namely the preparation part (where the particles were generated along with the container geometry), the simulation part (where the particles settled under gravity and the necessary bulk parameter computations were done) and the results extraction part (where the computed results and other responses were retrieved for further data processing).

Particle Generation

The very first step in setting up the model was to generate the particles that would ultimately resemble the real life sample. Here, the micro properties were specified in the form of the particle stiffness, inter-particle friction coefficient, particle density, local damping coefficients (if needed) and critical viscous damping ratios. The particle shapes were also specified (and the clumps constructed accordingly) along with the desired size distributions.

The particles were generated within a pre-determined volume (in random positions) so that the total volume of all the individual particles comprises 100% of this volume (regardless of the specified size and shape distributions). If more than one particle shape was present, the subtotal volume percentages of the individual shapes had to add up to 100%.

An automated code generator was used to create the necessary FISH code for particle generation. In this generator the abovementioned properties and inputs were specified. The code that was generated was then used in PFC^{3D} to generate the particles. This generator was used since thousands of particles are usually generated, making the individual tailoring of particle shape and size distributions very impractical. When the particles have been generated in PFC^{3D}, the model was saved for use in the next step, container generation.

Particle Size and Shape Considerations

The particle generation and the development of the subsequent bulk property simulation codes were done to account for the actual particle shapes that were identified for this project (see Section 4.2). The codes were therefore capable of simulating spherical, elongated and pyramid shaped particles, as in Figure 4.4.

The spherical particles are only characterised by the radii of their spheres. The minimum and maximum values (Table 4.2) were specified in the code generator. The ratio of the amount of spheres to that for the remaining shapes was also estimated and the subsequent volume percentage for the spheres was then specified in the code generator.

All four of the spheres comprising a pyramid clump have the same radius. The maximum and minimum radius values were also specified in the code generator, along with its relevant volume percentage. It should be noted that a Gaussian size distribution was generated from the specified minimum and maximum radii (for all of the considered particle shapes).

The elongated particles were constructed of two spheres clumped together. The DEM equivalent of the elongated particles assumed that the radii of the two spheres were the same (for a particular particle) as shown in Figures 4.3 and 4.4. This was done to simplify the experimental estimation of the size distributions. The codes were however implemented in such a way that the resulting experimental maximum and minimum radius be specified for each sphere within the elongated clump. This resulted in clumps with spheres that do not have the same radii. Although this deviates slightly from the initial assumption (equal radius within an elongated clump), the differences in radii were mostly marginal and thus of no concern. The maximum and minimum radii, as well as the volume percentage, were also specified for the elongated particles in the code generator.

The elongated clumps (also referred to as double clumps) were also characterised by the overlap between the two spheres. This was specified in the code generator. When no overlap was present, an overlap factor of $C = 1$ was used to enable a distance between the centres of the spheres equalling the sum of the radii (see Figure 4.4 for a double clump with no overlap and equal sphere sizes). If an overlap was present, then an appropriate overlap factor of smaller than 1 was used and subsequently multiplied with the sum of the two radii to obtain the distance between the sphere centres. The codes were developed to handle overlap factors between (and including) 0.5 and 1. The experimental particle shape characterisation as discussed in this chapter resulted in a DEM equivalent (for the elongated particles) that exhibited no overlap (Figure 4.4). In the design of experiments (DOE) investigations in Appendix A, a scenario was investigated where an overlap factor of 0.5 was also considered. Thus, for this project, only particles with no overlap ($C = 1$) and an overlap where $C = 0.5$ were generated for the double clumps. It should again be emphasised that the codes are capable to also account for overlap factors between 0.5 and 1. For the pyramid shaped particles no overlapping was considered.

Container Generation

Since the initial bulk properties were obtained when the bulk material sample was already in the container of the large scale shear box, the container geometry for the simulations was generated to resemble the experimental set-up. A FISH code was written in which the model (after particle generation) is restored, the container walls generated and the updated model saved again.

A top and bottom half were generated with a diameter of 590 mm and a 1 mm gap between the halves. The gap is approximately 165 mm from the bottom floor of

the container (which is halfway through the total sample and experimental container height of 330 mm). Additional walls were also created at the gap (on the outside of the container) to prevent any particles from falling out during the DST simulations. These container geometries were generated using cylindrical and flat (planar) walls in PFC^{3D}.

It should be noted that the pre-determined volume within which the particles were generated, starts approximately 100 mm from the floor of the container and extends to approximately 4 700 mm above the floor (as shown in Figure 4.9). The floor area of this volume is 200 x 200 mm. This was to allow for proper gaps between the particles when they were generated as well as to allow for them to settle under gravity. To enclose this volume, and to prevent any particles from escaping the computational domain, the top half of the container was generated to extend to a height of 5 000 mm, as opposed to just the experimental height of 330 mm. After the settlement under gravity, the sample was "levelled" at this desired height of 330 mm to resemble the experimental packing more realistically.

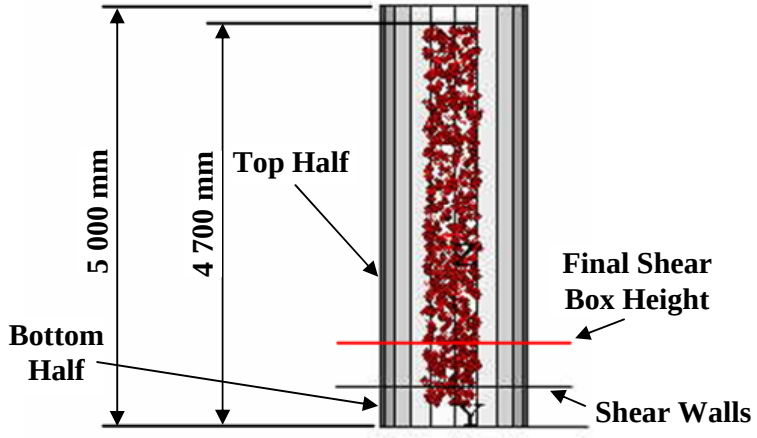

Figure 4.9 - Top Half Extension (To Fully Enclose Generated Particles)

For each wall that was generated, the appropriate particle-wall friction coefficient and wall stiffness was assigned. The experimental filling method used for this project entailed filling the container layer by layer (using a steel bucket), each time levelling the packing without compaction (Chapter 3). When observing the typical shear stress-strain curves from the experimental results in Chapter 3 and later in this chapter, the behaviour seems to be more in conjunction with a loosely compacted system. Härtl and Ooi (2008) observed the same behaviour but for a packing filled using the so-called rainfall filling method (where the particles are simply rained down in the container under gravity). Thus to ensure consistency between the experimental and DEM results for this project, the DEM simulations were prepared using the rainfall filling method.

Performing the BDPVR Simulation

The saved model after the particles and container walls have been generated was then restored for the BDPVR simulation to be conducted. Again, a FISH code was written which was used in PFC^{3D} to perform the simulation.

The main process that took place in this simulation is the settling of the particles under gravity in the container over a period of time (rainfall filling method), after which the packing was levelled at a desired height (in this case it is the experimental container height of 330 mm). It was allowed to settle again, to allow for any possible dynamic effects to damp out. The levelling was performed by deleting any sphere (from a spherical particle, or a clump) that had the *z*-position of its centre above 330 mm. The packing after the particles have settled can be seen in Figure 4.10, along with the packing after levelling at 330 mm.

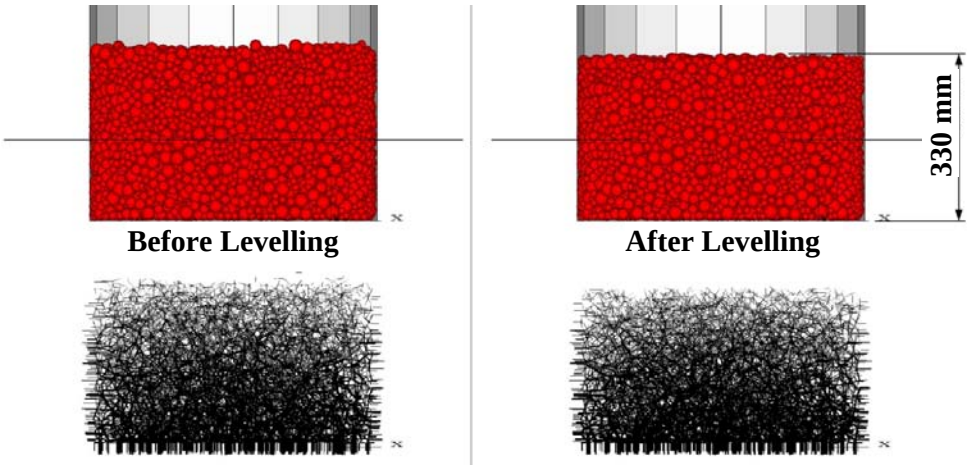

Figure 4.10 - DEM Packing Before and After Levelling

In Figure 4.10 the contact force chains between the particles can also be seen, indicating the increase in inter-particle contacts (in both the number of contacts and the magnitudes of the contact forces) towards the container floor.

After the levelling, the relevant initial bulk properties were computed. Firstly the initial height of the packing was determined. This was done by identifying the particle (sphere) that had the highest *z*-position above the floor of the container. Again it should be noted that this refers to the height of the centre of the sphere. This height was then taken and the radius of that particular sphere added, to obtain the initial numerical packing height, H. This, along with the cross-sectional area of the container, A, was used to calculate the bulk volume of the packing, V_b.

In PFC^{3D} the total mass of all the spheres in the packing can be computed by simply adding the individual masses of the spheres. In a similar fashion the total volume of the particles is computed by adding the individual sphere volumes.

When an overlap was present between two spheres, as in the case for the elongated clumps, the volume of this overlap had to be taken into account when computing the final total mass as well as the final total volume of the particles in the packing to gain a more accurate indication thereof. This overlap volume is in the form of a lens and was calculated as follows,

$$V_l = \frac{\pi}{12D}((R_1 + R_2 - D)^2)(D^2 + 2DR_2 - 3R_2^2 + 2DR_1 + 6R_2R_1 - 3R_1^2) \quad (4.9)$$

Here R_1 and R_2 are the radii of the spheres that the clump consists of and D the distance between the centres of the spheres, calculated with the overlap factor, C, as follows,

$$D = C(R_1 + R_2) \quad (4.10)$$

The total lens volume in the packing was obtained by adding these individual lens volumes. This total lens volume was then subtracted from the sum of the individual sphere volumes to determine the net total volume of the particles in the packing. Subsequently, the total lens volume was also used to determine the net total mass of all the particles in the packing by subtracting the mass of the lenses (total lens volume multiplied by particle density) from the sum of the individual sphere masses in the packing.

Using the definitions in Section 4.5.1, the bulk density of the packing was computed in the code using the net total mass and the bulk volume. Also, using Equations 4.4 and 4.7, the voids ratio and porosity were computed.

DEM Iterations and Results

The particle density was the first micro property to be calibrated. The bulk property from which this calibration was done is the bulk density. It should again be emphasised that, although the particle density was also measured directly (Section 4.5.1), the calibrated particle density was considered more reliable. The directly measured particle density was used as a comparison to the calibrated particle density.

The iterations were approached through varying the particle density over a range of 1 000 kg/m^3 to 10 000 kg/m^3, while all of the other parameters remained constant. For these iterations an inter-particle friction coefficient of 0.1, a particle-wall friction coefficient of 0.62, and a particle stiffness of 1 MN/m were used. The BDPVR part of the general simulation procedure was then run by implementing four different particle densities, namely 1 000 kg/m^3, 4 000 kg/m^3, 7 000 kg/m^3 and 10 000 kg/m^3. The particle size and shape distributions that were obtained in Section 4.2 were also directly implemented in these iteration simulations. The bulk densities that were obtained with the abovementioned micro property combinations can be seen in Table 4.6.

Table 4.6 - Simulated Bulk Densities

Particle Density (kg/m^3)	1 000	4 000	7 000	10 000
Bulk Density (kg/m^3)	560.6	2 232.1	3 926.9	5 617.1

The bulk densities are presented with relation to their respective particle densities in Figure 4.11. From this graph it is clear that the relation is very linear and a linear fit was applied to the data points to allow for an interpolation with which the calibrated particle density could be obtained.

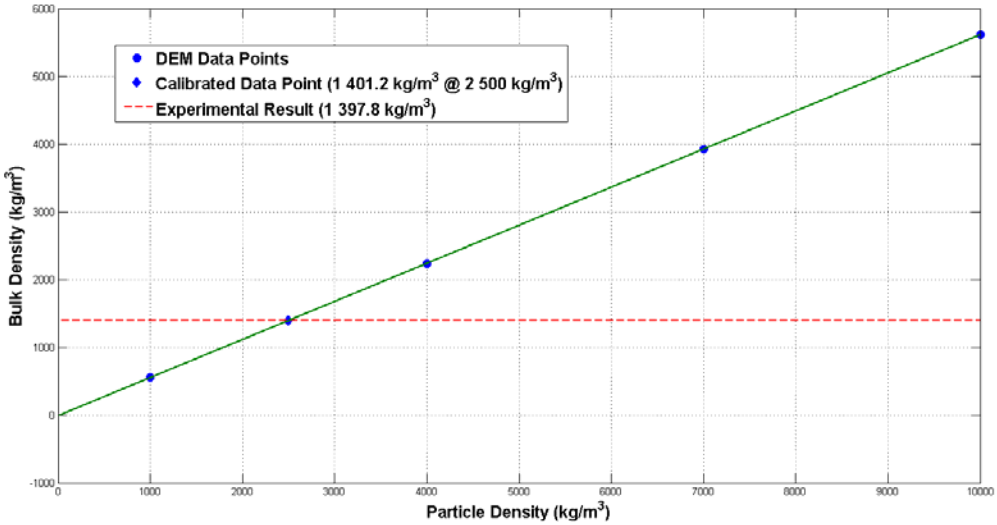

Figure 4.11 - Bulk Density versus Particle Density (Data Points and Linear Fit)

Through this linear fit it was found that a particle density of 2 500 kg/m^3 resulted in a bulk density of 1 397.8 kg/m^3 (which is the experimental bulk density).

This 2 500 kg/m^3 particle density was implemented, along with the other remaining properties used for these iterations, and the bulk density simulated again. The resulting bulk density obtained for this combination was 1 401.2 kg/m^3, which is still close to the experimental value (see Figure 4.11). The particle density is thus regarded as adequately calibrated for the crushed aggregate.

Also, the calibrated particle density of 2 500 kg/m^3 corresponds well with the experimental particle density of 2 586.5 kg/m^3 (from the direct measurements in Section 4.5.1). This is a strong indication that the particle size and shape distributions that were used for this project are also accurate.

4.6 Particle Stiffness

4.6.1 Experimental Results

The confined compression test was performed three times using the large scale shear box and procedure described in Chapter 3. One CCT was performed for each overall experimental procedure. The average confined Young's Modulus for the three runs is 8.69 MPa, while the average bulk stiffness is 7.22 MN/m. The confined Young's Modulus was used to calibrate the DEM particle stiffness, while the bulk stiffness was used as a calibration check.

4.6.2 Numerical Procedures

The second part of the simulations entailed the CCT simulations where the confined compression test was simulated.

Preparation of Model

The model at the end of the BDPVR simulation was restored and a lid was created (with the same wall stiffness and particle-wall friction properties as for the rest of the container). This lid was placed approximately 30 mm above the packing. This approach was followed to allow for the lid to slowly come into initial contact with the particles during the CCT simulation. In this way any excessive shock propagations through the packing would be prevented, as placing the lid at a position where immediate contact with particles is present will cause such a disturbance. When the lid was created and at its desired position, the model was once again saved for use in the next step, the actual CCT simulation.

Performing the CCT Simulation

The CCT simulation allowed the lid to displace up and down, at a constant velocity of 1 mm/s in both directions, to apply compression cycles on the packing. The lid first moves downwards until it touches the particles. It then continues to compress the particles until the maximum normal stress of 65.6 kPa is reached. The lid then changes direction and moves upwards (1 mm/s) until a normal force of zero is recorded on the lid. This constitutes one compression cycle of the CCT. This compression cycle is then repeated twice or three times depending on the investigation requirements. The FISH code for the CCT simulation was developed to allow for any number of compression cycles, although a conventional CCT only considers three to four cycles, as was done for this project.

A basic representation of the initial compression cycle can be seen in Figure 4.12. For subsequent compression cycles, steps b through d are repeated. The normal force on the lid (z-direction) was used to compute the normal stress (σ_n) induced in the packing during the CCT. The velocity of the lid, along with its vertical

position, was also recorded. The bulk normal strain that the packing experienced (ε_n) was calculated from the lid displacement.

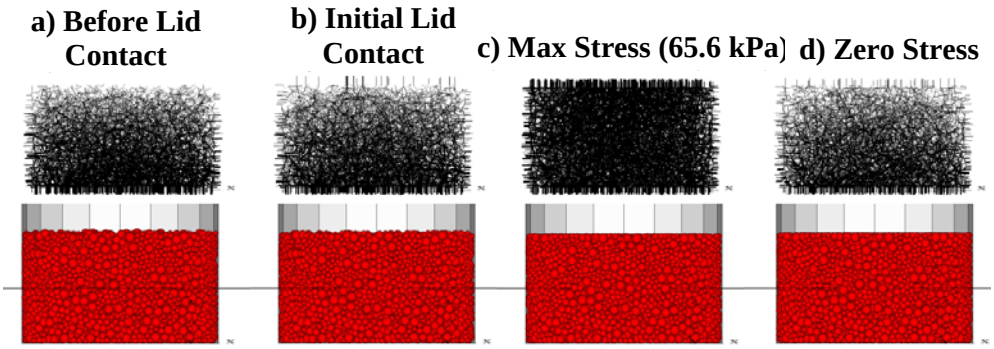

Figure 4.12 - Typical Compression Cycle During the Confined Compression Test

Data Processing and Results Representation

The normal stress is plotted against the normal strain for the first three compression cycles in Figure 4.13. Here the first compression cycle's initial compaction effect on the packing can clearly be seen (Loading 1). In the following compression cycles a more linear behaviour is observed for the loading parts of the cycles (Loading 2 and 3). The data was processed to plot the second, third and fourth compression cycles (as in Figure 4.14).

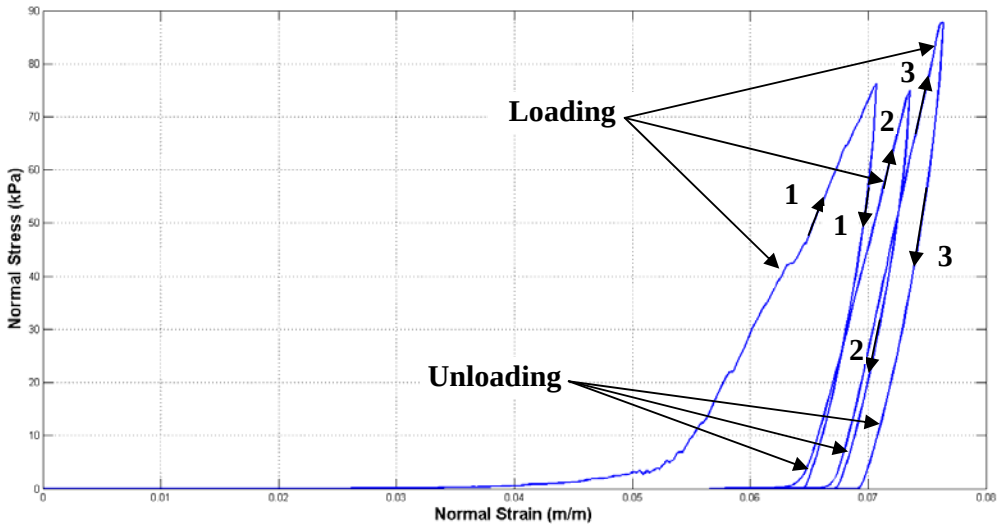

Figure 4.13 - Typical Compression Cycles from a CCT Simulation (First Cycle Included)

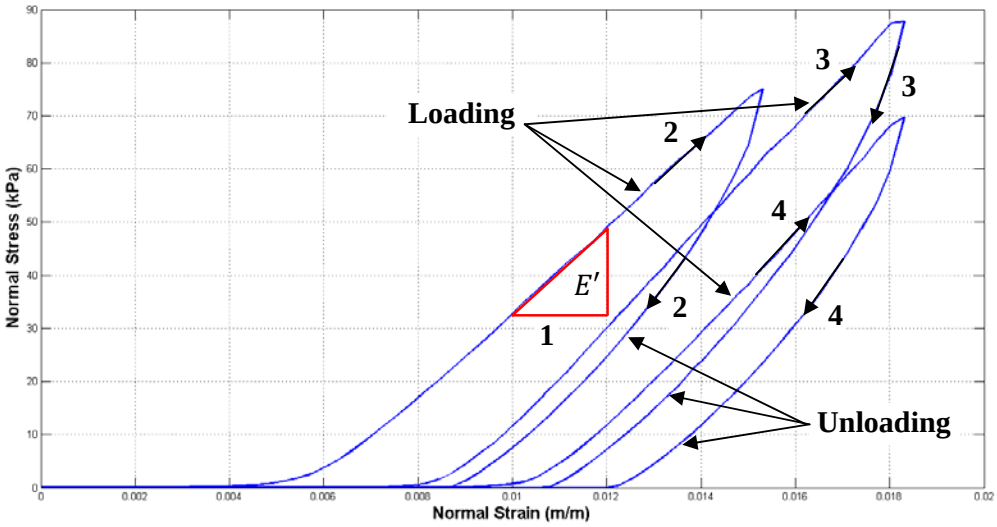

Figure 4.14 - Typical Compression Cycles from a CCT Simulation (First Cycle Omitted)

The loading parts of the second, third and fourth cycles (Figure 4.14) were used to determine the confined Young's Modulus for the particular CCT simulation. As can be seen, the loading parts are largely linear. Estimating the slope of this region would ultimately give the confined Young's Modulus. Taking the centre region of the loading part of a compression cycle (as seen in Figure 4.14 for the second compression cycle), the upper and lower data points for that region were recorded from the graph. The confined Young's Modulus for that compression cycle was then calculated as follows:

$$E' = \frac{\sigma_n^{upper} - \sigma_n^{lower}}{\varepsilon_n^{upper} - \varepsilon_n^{lower}} = \frac{\Delta\sigma_n}{\Delta\varepsilon_n} \tag{4.11}$$

This calculation was repeated for the remaining compression cycles and the average of the three values obtained to indicate the particular packing's simulated confined Young's Modulus. The bulk stiffness for each compression cycle was calculated as in Equation 4.12. Again, taking the average of the three values yielded the simulated bulk stiffness for the numerical packing under investigation.

$$k_b = \frac{A}{H} E' \tag{4.12}$$

DEM Iterations and Results

With the particle density calibrated (at 2 500 kg/m^3), the calibration process was then shifted to that of the particle stiffness calibration. The bulk property of interest here is the confined Young's Modulus. Four combinations of micro property values were again used and the confined compression test (CCT) simulations were conducted for each combination. The particle stiffness values used are 1 MN/m, 1.7 MN/m, 2.3 MN/m and 3 MN/m. Considering the flow of

the simulation procedure, the bulk density for each of the four combinations was also computed to evaluate any effects on it.

The calibrated particle density of 2 500 kg/m3 was used, along with an inter-particle friction coefficient of 0.1 and a particle-wall friction coefficient of 0.62. These properties remained constant while the particle stiffness values were changed between iterations. Furthermore a maximum normal stress of 65.6 kPa was simulated for the CCT simulations. The simulated confined Young's Moduli for the four combinations can be seen in Table 4.7.

Table 4.7 - Simulated Confined Young's Moduli

Particle Stiffness (MN/m)	**1.0**	**1.7**	**2.3**	**3.0**
Bulk Density (kg/m^3)	1 401.2	1 396.7	1 395.0	1 393.6
Confined Young's Modulus (MPa)	5.62	9.05	11.55	12.34

The bulk density was also calculated for each particle stiffness and it was found to vary by less than 3% over the range of stiffnesses tested. There was therefore no need to recalibrate the particle density once the particle stiffness was calibrated. Plotting the simulated confined Young's Moduli against their respective particle stiffnesses and fitting a linear curve through them, the following graph is obtained (Figure 4.15):

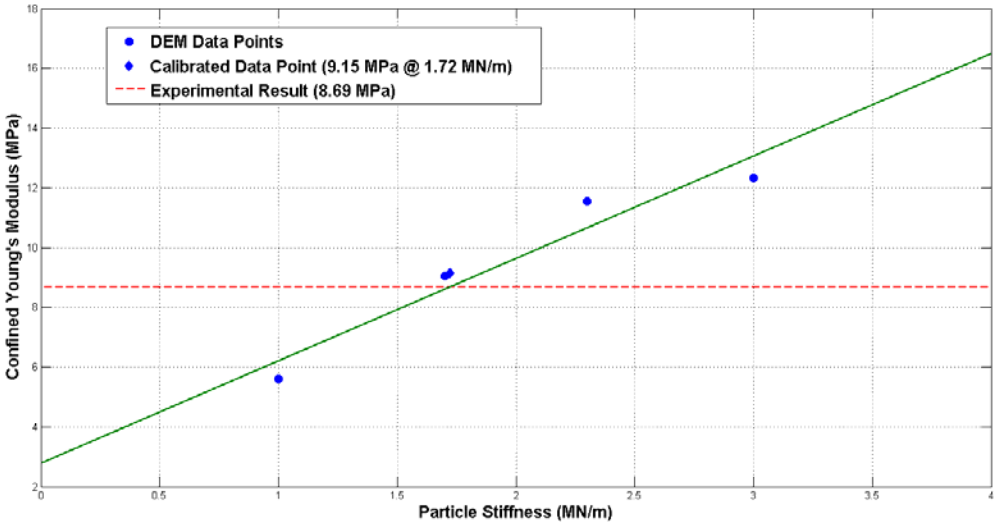

Figure 4.15 - Confined Young's Modulus versus Particle Stiffness (Data Points and Linear Fit)

The relation between the confined Young's Modulus and the particle stiffness was assumed to be linear. An interpolated particle stiffness of 1.72 MN/m seems to yield a numerical confined Young's Modulus that is the same as the experimental value, 8.69 MPa. This new particle stiffness of 1.72 MN/m was implemented in another CCT simulation without changing the other parameters. A simulated confined Young's Modulus of 9.15 MPa was obtained, along with a simulated

bulk density of 1 397.1 kg/m^3. Therefore the particle stiffness can be considered properly calibrated.

4.7 Inter-particle Friction Coefficient

4.7.1 Experimental Results

Using the large scale shear box and the test procedure in Chapter 3, the direct shear test was performed on the material. Again, a total of three DST's were conducted, one for each overall test run. An average internal friction angle of 60.6° was obtained for the three runs. Furthermore, an average angle of dilatancy of 13.2° was also obtained for the crushed rock aggregate in this project. The inter-particle friction coefficient was calibrated using the internal friction angle.

4.7.2 Numerical Procedure

The third and final part of the simulation work is that of the direct shear test (DST) simulations. The model, as saved after the lid was created (that is before the CCT simulation was performed) was also restored for use in the DST simulations. The DST simulations were once again divided into three steps, the preparation part (also known as the initial compression), and the simulation part (where the actual direct shear test is simulated) followed by the extraction of the results. This sequence was conducted a total of four times, one for each of the applied normal loads on the packing (as discussed in Chapter 3). In the preparation part of the DST simulation, the packing was compressed to that particular run's desired normal load. This load was then maintained on the packing as the actual shear action was simulated.

Preparation of Numerical Sample

A copy of the saved model after the lid was created 30 mm above the packing was restored for the preparation of the packing for the DST simulation. The preparation process entailed the lid being displaced downwards at a velocity of 1 mm/s until a maximum normal load of 65.6 kPa on the packing was reached. The lid was then moved upwards at 1 mm/s to a normal force of zero. Then a last downward compression (at 1 mm/s) was performed to the desired normal load for that specific run. When the desired normal load was reached the lid was stopped and the model saved. This process was then repeated until four saved models were obtained (one for each of the four normal loads required to simulate the DST).

Performing the DST Simulation

To perform the DST simulation for one normal load case, the prepared model with its applied normal load was restored. Since the lid came to a sudden stop after compressing the packing, the system needed to stabilise by allowing any shock propagations through the packing to damp out. This was achieved by slightly

adjusting the lid's position as the propagations damp out, while still maintaining the specified normal load for that particular model. In the FISH code for the DST simulation, a servo function was written to accomplish these lid adjustments.

When the prepared model was restored, the system was allowed to stabilise for 20 simulated seconds using the servo function to maintain the relevant normal load. Twenty seconds were deemed an adequate stabilising time for packings with large inter-particle friction coefficients. After the 20 second stabilisation, all of the walls that constitute the bottom half of the container were displaced horizontally (in the *x*-direction) at a velocity of 1 mm/s, to induce the shear effect in the packing. This displacement took place over a simulated time of 70 seconds, to result in the 70 mm total shear displacement.

As the shear displacement progresses the packing will contract and expand vertically, as explained in Chapter 3. Here the servo function was used again, displacing the lid accordingly, in order to maintain a constant normal load on the packing during the simulation. In Figure 4.16 the packing before the DST simulation was started (after the packing has stabilised under the applied normal load) can be seen, along with the packing at the end of the simulation.

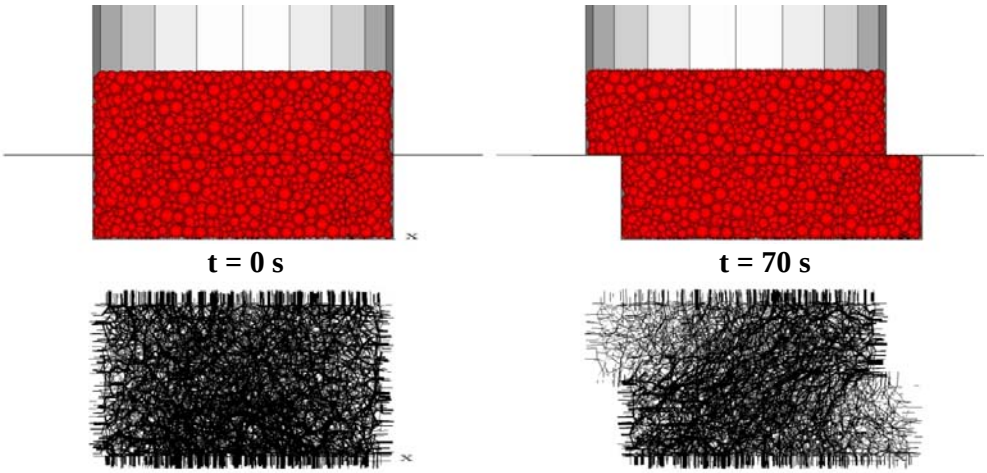

Figure 4.16 - Packing Before and After DST Simulation

The abovementioned description is applicable to one normal load application. This process was then repeated for the remaining normal loads in order to complete the full DST simulation.

Data Processing and Results Representation

The normal force on the lid, its vertical position, the net horizontal bulk force on the floor (and cylindrical part of the bottom half) and their horizontal position were the most important results considered for the data processing in the DST simulations. The lid force and position were used to calculate the bulk normal stress, σ_n, and bulk normal strain, ε_n, in the same fashion as for the CCT

simulation. The initial packing height, in this case, was taken as the height of the packing at the end of the 20 second stabilisation period.

The net horizontal bulk force (in the direction of shear) on the cylindrical wall of the bottom container half was added to the net horizontal bulk force on the floor, to estimate the total shear force that the packing was subjected to. It was then divided by the cross-sectional area of the container to obtain the bulk shear stress on the packing, σ_s. The net forces in the other directions were considered to have a negligible effect on the bulk shear stress in the packing.

The bulk shear strain, ε_s, was obtained by expressing the horizontal shear displacement of the bottom container half as a percentage of the container diameter. Plotting the typical shear and normal stresses against shear strain (for the four different applied normal loads), yields the following (Figures 4.17 and 4.18):

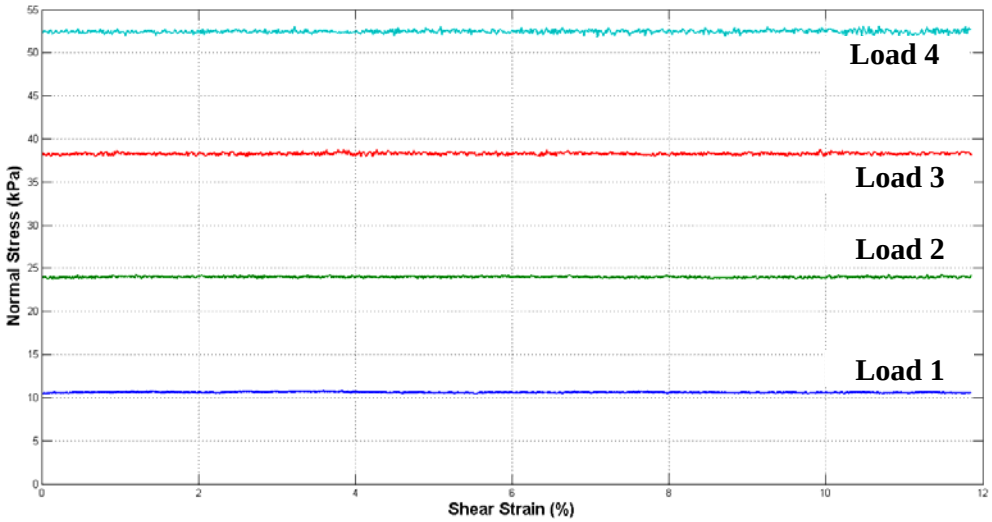

Figure 4.17 - Simulated Normal Stresses for Different Applied Normal Loads

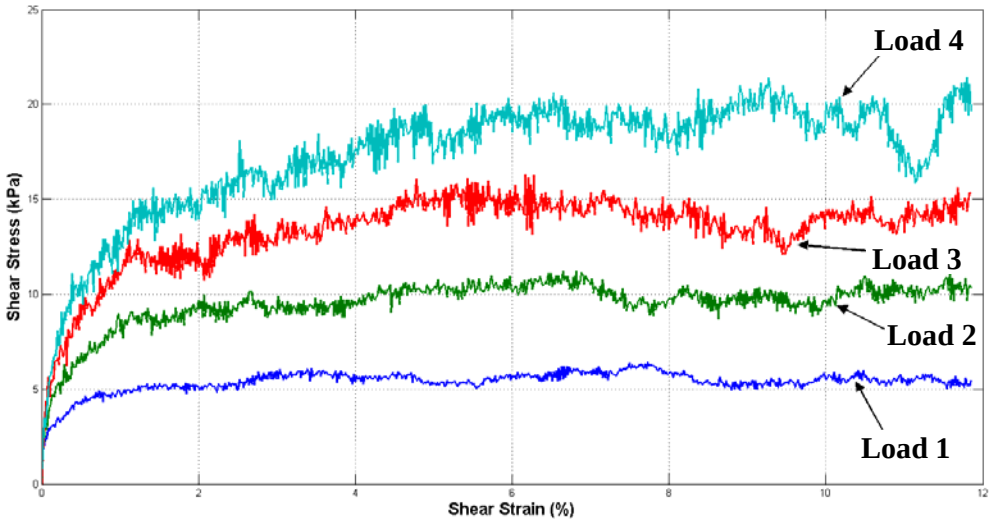

Figure 4.18 - Simulated Shear Stresses for Different Applied Normal Loads

From these plots it is clear that the frictional effects, between the particles and between the particles and the relevant walls, caused the plots to exhibit a degree of scatter in the data points. In the figures above, this scatter does not pose any problems. However, when particles with higher inter-particle friction coefficients are simulated, this scatter can become more significant, making the interpretation of the data more challenging. To account for this, it was deemed necessary to smooth the data by using the moving average method, with a span of 21 data points. This was then implemented for all of the DST simulation data in this project with regard to the normal and shear bulk stresses of the packing. The smoothed plots for the data in Figure 4.18 can be observed in Figure 4.19.

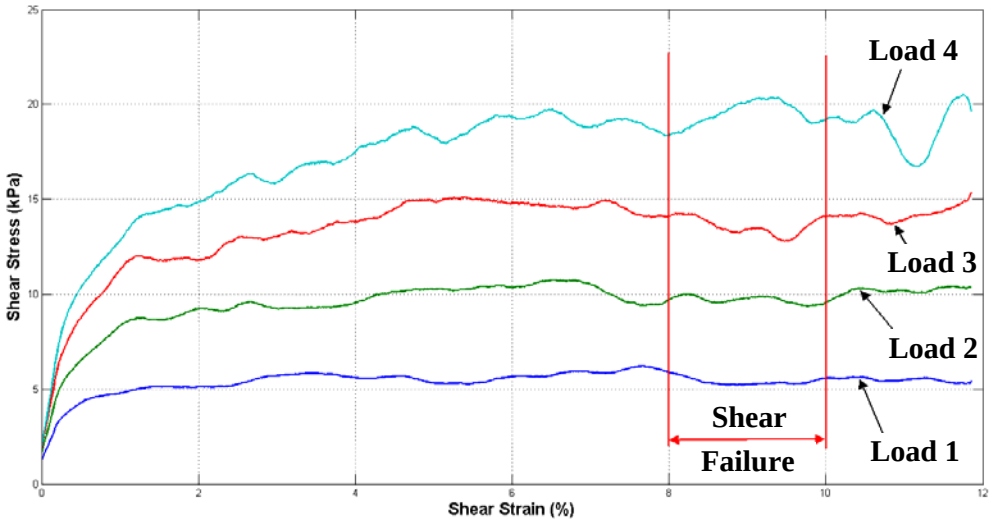

Figure 4.19 - Smoothed Shear Stresses for Different Applied Normal Loads

In Figure 4.17 it can be seen that servo function performed very well in keeping the normal stresses induced on the packing, constant through the simulation. It can

also be seen that the indicated normal stress values (for each normal load case) correspond with the initial normal stress regions in Figure 3.12 in Chapter 3, which is supposed to be the case since that region in the experimental curves was used as the input for the DST simulations (also see Table 3.1).

As was done for the experimental data processing, shear failure was assumed to have taken place between 8% and 10% shear strain. The average of the data points between 8% and 10% shear strain was thus taken to obtain the average shear and normal stresses (for each normal load case). A typical plot of the four average shear stresses against their corresponding average normal stresses can be seen in the shear envelope in Figure 4.20. As for the experimental work, a linear fit through these points was also generated. The slope of this linear fit was also used to determine the simulated internal friction angle, ϕ, of the particular packing, also using Equation 3.2 in Chapter 3.

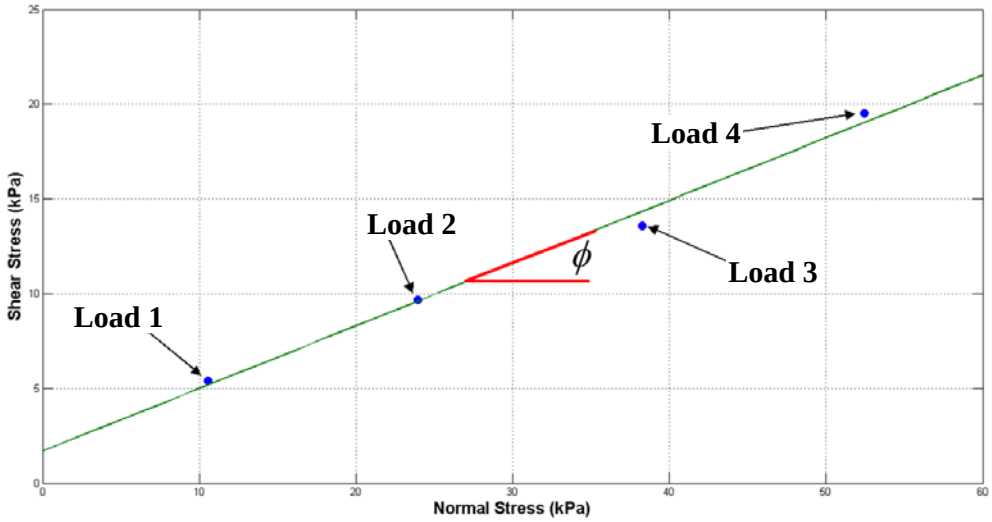

Figure 4.20 - Simulated Shear Envelope

In Chapter 3 the estimation of the experimental angle of dilatancy was discussed. By plotting the displacement of the lid against the shear displacement of the bottom half and obtaining the average gradient of the graph between 8% and 10% shear strain, the angle of dilatancy can be estimated. However, when plotting the same results from the DST simulations, the following representation is obtained (Figure 4.21):

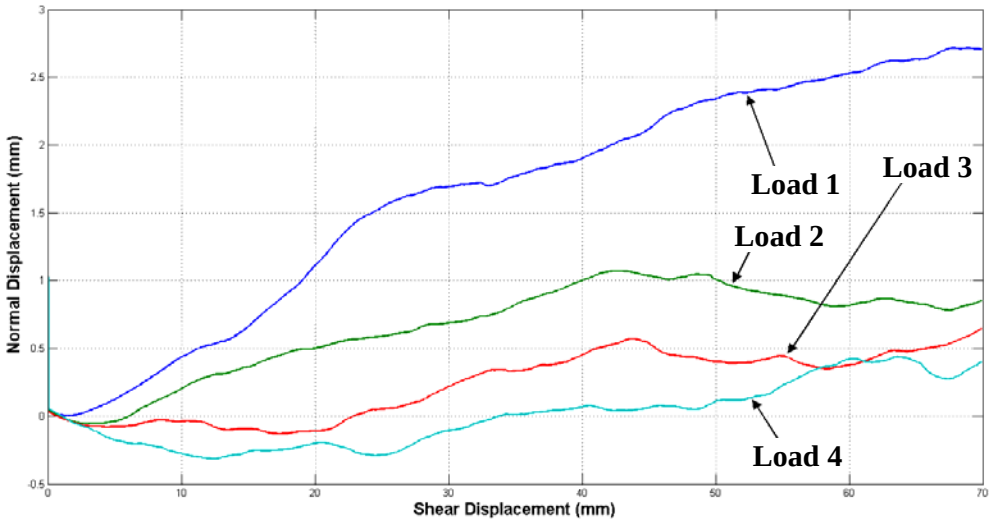

Figure 4.21 - Simulated Lid Displacement versus Bottom Half Displacement

Here the initial contraction before the packing starts to expand in a linear fashion, as seen in Figure 3.15, cannot be clearly observed. The linear region used to calculate the gradient between 8% and 10% shear strain also appears not to be replicated in the DST simulation. This can be attributed to the round edges of the clumps, in comparison with the sharper edges of the actual material, that allow for easier inter-particle slip to occur. This ultimately causes the simulated packing contraction and expansion to be inconsistent as the shear displacement develops. Where linear behaviour is observed, the gradients are significantly lower than for the experimental results. The decreasing dilative behaviour, as the normal load increases, can however still be observed, albeit not in the clearly defined nature of the typical experimental results. As a parameter to implement in bulk material calibration, the angle of dilatancy depends largely on the accuracy with which the particle shapes are defined. Since the particle shapes for this project have been simplified to a large extent, the angle of dilatancy was thus not used as a critical bulk parameter.

DEM Iterations and Results

The final component of the calibration iterations was the calibration of the inter-particle friction coefficient by means of the direct shear test simulations. The bulk property under question here is, of course, the internal friction angle. Using the calibrated particle density and particle stiffness, five combinations were simulated, each for a different inter-particle friction coefficient.

For each of the five combinations the calibrated particle density (2 500 kg/m^3) and particle stiffness (1.72 MN/m) were used along with the particle-wall friction coefficient of 0.62. The five inter-particle friction coefficients that were used are 0, 0.1, 0.5, 0.8 and 1. The four normal load cases on the packing, relevant to the

DST, were also implemented for each combination (Table 3.1). The simulated internal friction angles for the five combinations can be seen in Table 4.8.

Table 4.8 - Simulated Internal Friction Angles

Inter-particle Friction Coeff	0.0	0.1	0.5	0.8	1.0
Bulk Density (kg/m^3)	1 461.2	1 397.1	1 395.6	1 395.6	1 395.2
Confined Young's Mod (MPa)	9.31				
Internal Friction Angle (°)	9.9	18.3	35.0	51.2	77.7

The scenario for zero inter-particle friction was performed as an additional test to investigate the effect of a frictionless material. It was found that the bulk density for this material is higher than that of a material that does exhibit some degree of friction. This does make sense since the frictionless particles will slide more readily between each other, under gravity, to result in a more densely compacted packing. For the other materials with an inter-particle friction coefficient of 0.1 and higher, the bulk density did not change significantly and still remained very close to the experimental bulk density of 1 397.8 kg/m^3. Considering that most materials will exhibit a mentionable degree of inter-particle friction, it can be safely assumed that the inter-particle friction does not substantially affect the bulk density of the packing.

For the zero inter-particle friction coefficient the confined Young's Modulus was also simulated. A value of 9.31 MPa was obtained, which is also close to the experimental result of 8.69 MPa. Therefore the confined Young's Modulus for a packing appears not to be significantly affected by the inter-particle friction coefficient, at least for low friction materials.

When plotting the internal friction angles against the inter-particle friction coefficients, it is found that the experimental internal friction angle of 60.6° is numerically obtained using a linearly interpolated inter-particle friction coefficient of 0.86 (see Figure 4.22). The result with zero inter-particle friction was run to estimate the interlocking effect. Although not practically possible, it might help to classify particle shapes in the DEM. This is not further used in this study, but might be useful as a calibration method in future work.

When this newly calibrated inter-particle friction coefficient of 0.86 was used to simulate the internal friction angle again, a simulated internal friction angle of 61.2° was obtained. This angle is very close to the experimental result of 60.6°.

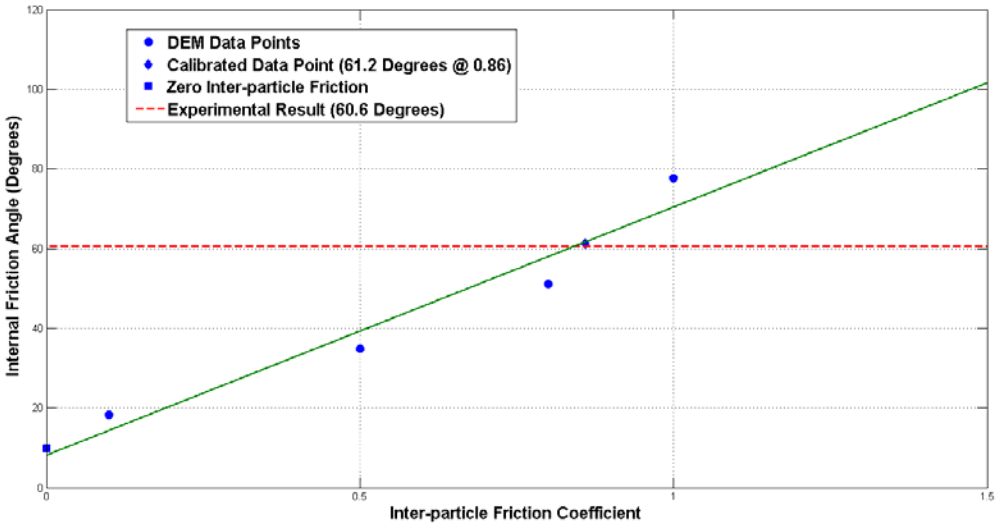

Figure 4.22 - Internal Friction Angle versus Inter-particle Friction Coefficient (Data Points and Linear Fit)

4.8 Concluding Remarks

The micro properties that were obtained through the numerical iterations, along with the other properties that were obtained more directly are summarised in Table 4.9. These values are thus seen as the calibrated micro properties that should allow for the DEM replication of the crushed aggregate that was investigated in this project.

These micro properties were all used in a final round of simulations as a final check to see whether the calibration procedure yielded adequate results. The BDPVR simulations were run, after which the CCT and DST simulations were conducted.

Table 4.9 - Final DEM Input Parameter Calibration Results

Micro Parameter		Result		
Particle Shape Distribution		Pyramid	Elongated	Spherical
Particle Size Distribution	R_{min} (mm)	7.5	12.0	15.0
	R_{max} (mm)	10.5	15.0	16.2
	% Vol	37.5	41.7	20.8
Local Damping Coefficient				0.0
Viscous Damping Ratio, ξ				0.8
Particle-wall Friction Coefficient, μ_{pw}				0.62
Wall Stiffness, k_w (MN/m)				10.0
Particle Density, ρ_p (kg/m^3)				2 500
Particle Stiffness, k_p (MN/m)				1.72
Inter-particle Friction Coefficient, μ_{pp}				0.86

The bulk properties that were used in the calibration procedure were again simulated. The other bulk properties that were obtained experimentally (see Table 4.10) were also compared to their DEM counterparts. The purpose of this was to compare the entire range of bulk properties considered in this project, from both an experimental and numerical point of view, using the calibration procedure's results. The simulated bulk properties, compared to the experimental results, are as follows:

Table 4.10 - Final Comparison of Bulk Properties (DEM versus Experimental)

Parameter	DEM	Experimental	% Variation
Initial Bulk Volume, V_b (m^3)	0.094	0.090	4.74
Initial Height, H (m)	0.340	0.329	4.74
Bulk Mass, m_b (kg)	131.6	125.8	4.63
Initial Bulk Density, ρ_b (kg/m^3)	1 395.8	1 397.8	0.09
Initial Porosity, n (%)	44.2	45.9	3.94
Initial Voids Ratio, e	0.79	0.85	7.06
Confined Young's Modulus, E' (MPa)	6.95	8.69	20.0
Bulk Stiffness, k_b (MN/m)	5.59	7.22	22.6
Internal Friction Angle, ϕ (°)	61.2	60.6	0.99
Angle of Dilatancy, ψ (°)		13.2	

The initial bulk volume, sample height and bulk mass show a variation of between 4.6% and 4.8% between the experimental and numerical results. A very good correlation was obtained between the experimental and numerical results for the initial bulk density (less than 1% variation).

For the initial porosity a variation of less than 4% was applicable, with a 7% variation for the initial voids ratio. Considering the discrepancies between the numerical and physical particle size and shape distributions, these variations can still be regarded as within acceptable limits.

A fairly large discrepancy between the experimental and numerical results for the confined Young's Modulus can be observed (20%). This is due to the experimental procedure for the CCT, with its discrete intervals of load application and recording (see Chapter 3), as opposed to the more continuous load application in the corresponding simulations. The 23% variation for the bulk stiffness results can also be attributed to this.

Inconsistent initial height values that were used to obtain the average DEM bulk stiffnesses can also be a cause of the large discrepancies between the DEM and experimental bulk stiffness values. By refining the experimental procedure for the CCT, the reliability of the results can be improved significantly.

The internal friction angle shows a very good correspondence between the experimental and numerical results (less than 1% variation). Since the frictional behaviour of a bulk material packing is one of the most significant bulk

characteristics, this serves as an indication that the general calibration process was properly executed and that reliable results were indeed obtained.

Due to the difficulty in obtaining numerical angles of dilatancy, these parameters were not used in the comparisons of the experimental and numerical bulk properties.

Considering the very small variations between the experimental and numerical bulk densities, as well as internal friction angles, the calibration procedure and its end results can be regarded as satisfactory. As a further calibration verification, the calibrated micro properties were implemented in a series of angle of repose and anchor pull test simulations. The results were compared to their experimental equivalents in a final evaluation of the calibration procedure's reliability. This verification is discussed in Chapter 5.

5. Verification of Calibration Procedure

5.1 Introduction

With the calibration procedure completed, the results needed to be verified before implementing them in other simulations. A verification test procedure is needed to process the material, after which the procedure is replicated in the DEM, using the calibrated micro properties. Should the numerical and experimental results correspond satisfactorily the calibration procedure can be regarded as successful. If not, the calibration procedure should be repeated or revised.

The need for the verification of a material calibration is also frequently overlooked. It is thus essential that a calibration procedure is accompanied by a proper verification procedure. Since bulk material behaviour is largely application dependent, the calibration procedure and especially the test parameters depend on the parameters of the application which needs to be simulated. A verification test procedure is consequently needed that corresponds well with the application for which the calibration is performed.

In this project two verification tests were implemented, namely the angle of repose test and the so-called anchor pull-out test. For the purposes of this project, the application for which the calibration was done was assumed to be similar to that of a system consisting of an anchor that is pulled from a packing of bulk materials. The angle of repose test was taken as an independent additional test.

This chapter describes the concepts of both the angle of repose and anchor pull-out tests. The experimental tests are discussed along with their DEM replications. For the angle of repose simulations the calibrated micro properties were implemented in an attempt to validate the results. Additionally the effect of inter-particle friction on the angle of repose was investigated. In the case of the anchor pull-out simulations the calibrated micro properties were also implemented after which the sensitivity of the results for inter-particle friction and particle stiffness were investigated. Furthermore the effect of system parameters such as anchor pull velocity and material packing depth were explored.

5.2 The Angle of Repose Test

The angle of repose, α, for a bulk material sample can be defined as a measure of inclination of the free surface to the horizontal of a bulk solid pile (Ileleji and Zhou, 2008). It is a very important macro parameter that is used to characterise the behaviour of bulk materials and depends largely on micro properties such as sliding and rolling friction, particle density together with size and shape distribution (Zhou *et al*. 2002). It is generally obtained by allowing a sample of bulk material to form a pile and then measuring the resulting angle of repose as in Figure 5.1.

The pile can be formed by discharging the bulk material from a hopper, or funnel, onto a fixed bed, or to discharge the material such as to form free-standing pile (Figure 5.1a). These angles of repose are known as static angles of repose (Ileleji and Zhou, 2008).

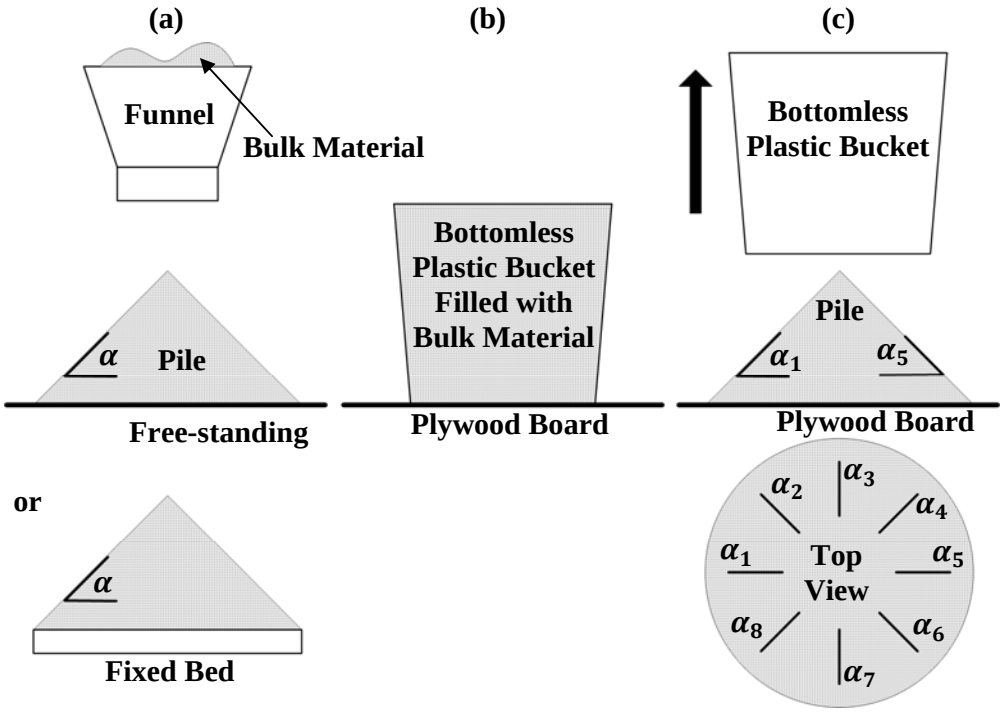

Figure 5.1 - Schematic Representation of (a) Static Angle of Repose and (b, c) Experimental Procedure

Other methods to obtain the angle of repose include tilting a rectangular box filled with bulk material and then measuring the angle at which the material starts to slide, or avalanche (sliding angle of repose) and measuring the angle formed by material in a revolving cylinder. These angles of repose are known as dynamic angles of repose (Ileleji and Zhou, 2008) and can be seen in Figure 5.2. According to (Ileleji and Zhou, 2008) the static angle of repose is, in general, lower than the dynamic angle of repose.

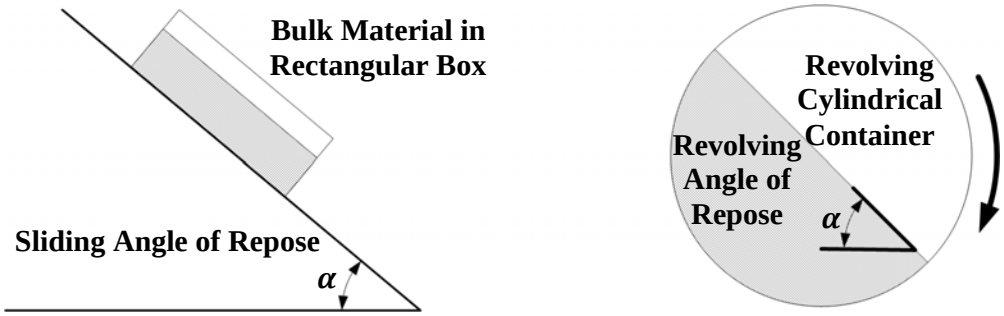

Figure 5.2 - Schematic Representation of Dynamic Angle of Repose (Sliding and Revolving)

These differences between the static and dynamic angle of repose tests and the parameters that have an effect on the results make the correct definition and interpretation of the angle of repose very challenging. Also, the angle of repose can only be considered as a relative and qualitative data set, which makes the interpretation thereof even more challenging (Ileleji and Zhou, 2008). The ease of measuring an angle of repose makes it a useful test to obtain basic estimations of the behaviour of a bulk materials sample. However, the angle of repose is a subject of great debate among researchers as to its usefulness as a flow property. At best the angle of repose, regardless of the method used, provides the relative behaviour of a bulk material under a number of test conditions and is applicable to a specific bulk material handling scenario (Ileleji and Zhou, 2008). Thus, when the angle of repose is used, the method of acquiring it should be relevant to the scenario that is to be investigated.

Since the angle of repose is found to be strongly dependent on micro friction properties and particle shape, it is a popular test to calibrate these parameters for use in subsequent simulations. When considering the abovementioned challenges in an angle of repose, focus could rather shift from using the angle of repose test as a calibration tool, to using it as a verification of the calibration procedure. It is presumed to verify the particle size and shape distribution together with the inter-particle friction. Since the specific way in which the angle of repose test is executed might influence the results, the numerical simulations should closely follow the experimental procedures. With this taken into account, an angle of repose test was devised for this project and then implemented numerically and experimentally in a controlled and repeatable fashion.

5.2.1 Experimental Procedures

An experimental procedure was devised in which the sample is contained in a bottomless, tapered cylindrical container. This container is then slowly lifted allowing the material to flow out from underneath the bottom opening and to form a free standing pile. The angle of repose, as defined, is then estimated using an electronic protractor. A schematic of the experimental procedure can be seen in Figure 5.1b and 5.1c.

For this project the cylindrical container was a bottomless plastic bucket which was placed on a plywood board that served as the floor. The bucket has a bottom diameter of 260 mm, a top diameter of 290 mm and a height of 370 mm. The container was then manually and very slowly lifted to form the pile, as shown in Figure 5.3.

Figure 5.3 - Angle of Repose Test in Progress

The angle of repose was then measured using the electronic protractor, at eight different sections of the pile (see Figures 5.1c and 5.4). The average of the eight values was taken as the angle of repose for the sample. For the crushed aggregate the average angle of repose was found to be 40°. The eight measurements used to obtain the average are shown in Table 5.1.

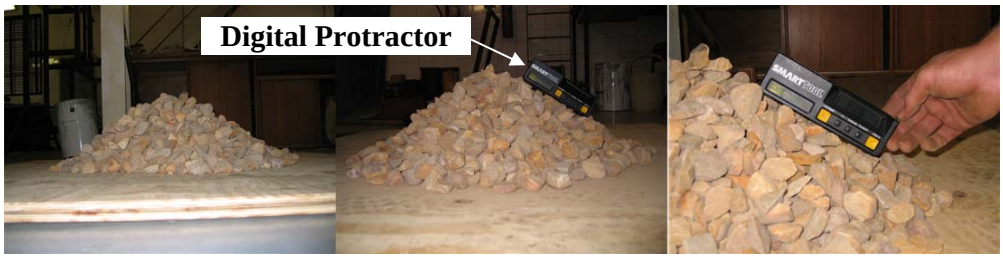

Figure 5.4 – Experimental Angle of Repose

Table 5.1 - Experimental Angle of Repose Measurements

Angle	α_1	α_2	α_3	α_4	α_5	α_6	α_7	α_8	α_{exp}^{avg}
Measurement (°)	36.8	38.5	33.6	37.5	46.1	40.4	47.3	41.1	40.0

5.2.2 Numerical Procedures

The experimental test set-up was replicated in PFC^{3D}. The calibrated micro properties as in Table 4.9 were used, with particle-wall friction coefficients of 0.67 and 0.86 for the plastic and plywood interface respectively (Table 4.4). A vertical velocity for the container was specified at 5 mm/s, commencing after the packing was allowed to settle under gravity and levelled to the experimentally filled height of 370 mm. The typical progression of the simulation can be seen in Figure 5.5.

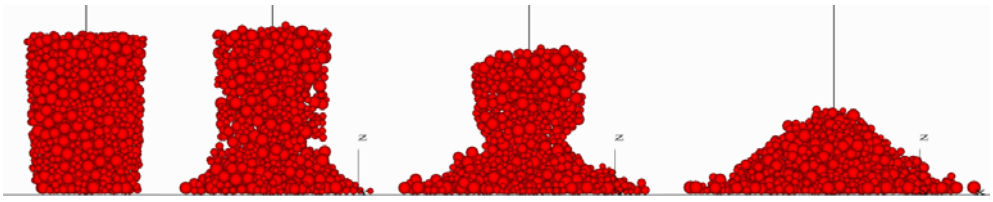

Figure 5.5 – Angle of Repose Simulation in Progress (Bucket not Shown)

The angle of repose was then obtained by means of visual inspection from the final figures created by the simulation. The final front and side views of the pile were used as in Figure 5.6, after which the average of the four readings were taken as the numerical angle of repose (see Table 5.2).

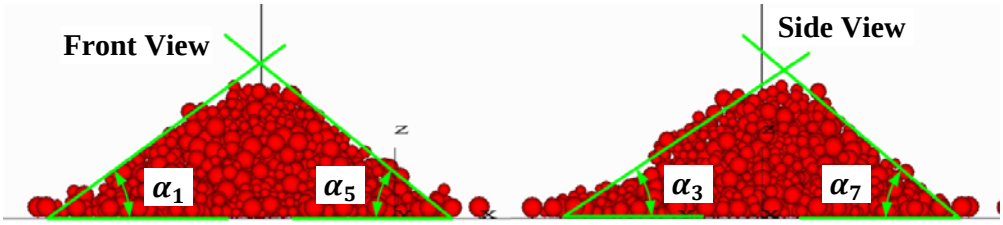

Figure 5.6 – Numerical Angle Repose Estimation

Table 5.2 – Numerical Angle of Repose Estimation

Angle	α_1	α_5	α_3	α_7	α_{num}^{avg}
Estimation (°)	43.0	36.0	38.0	36.0	38.0

5.2.3 Comparison between Experimental and Numerical Results

In Figure 5.7 the angle of repose, as obtained in PFC^{3D}, is indicated along with the experimental angle of repose. As can be seen, the experimental and numerical angles of repose correspond very well. The numerical angle of repose of approximately 38° is considered sufficiently close to the experimental angle of 40°.

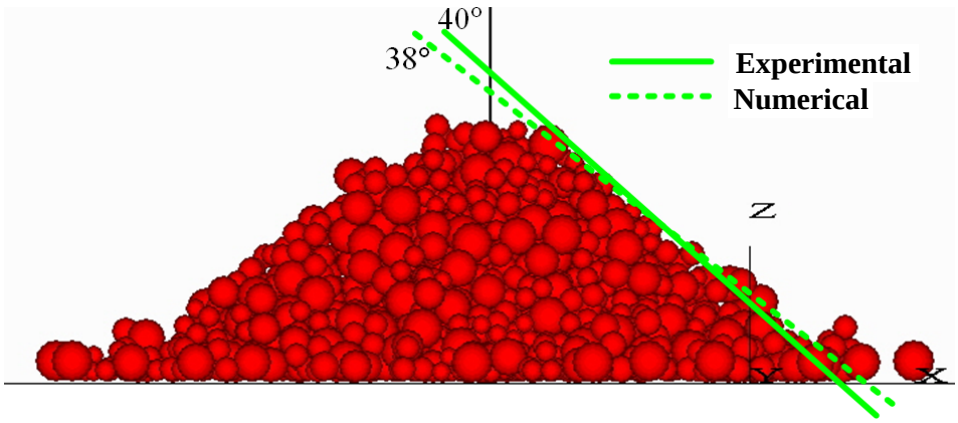

Figure 5.7 – Experimental and Numerical Angles of Repose

With the abovementioned taken into account it is found that, as far as the angle of repose test is concerned, the calibration procedure can be regarded as successful. It also serves as an indication that the angle of repose test can be effectively used as a calibration verification tool, as opposed to being used purely for calibration purposes.

Again it should be mentioned that the verification tests used depend on the application for which the material is calibrated. Since the angle of repose is largely friction and particle size (and shape) dependent, using it as a verification tool will, at best, aid in verifying the calibration of the friction and particle size and shape. Thus, it can safely be concluded that these micro properties have been calibrated to the desired accuracy.

5.2.4 The Effect of Inter-particle Friction on the Angle of Repose: A Sensitivity Analysis

In the previous section, it was shown that the calibrated micro properties used in the simulation could accurately predict the experimental angle of repose. However, since the angle of repose did not form part of the original calibration procedure, the effects of the different micro properties on the angle of repose are not available. In this section, an additional investigation was performed in which the effect of the inter-particle friction on the angle of repose was determined. In the verification it was found that, if looking at friction alone, the inter-particle friction coefficient of 0.86 resulted in an angle of repose of 38°, which is close to the experimental result of 40°. Further simulations were done where the inter-particle friction was varied (while keeping the remaining properties constant as in Table 4.9) and the resulting angles of repose obtained. The friction coefficients and resulting angles of repose can be seen in Figure 5.8 and Table 5.3.

Table 5.3 - Inter-particle Friction and Resulting Numerical Angle of Repose

Inter-particle Friction Coefficient	0.1	0.3	0.5	0.65	0.86	1.0
Angle of Repose (°)	12	25	36	36	38	40

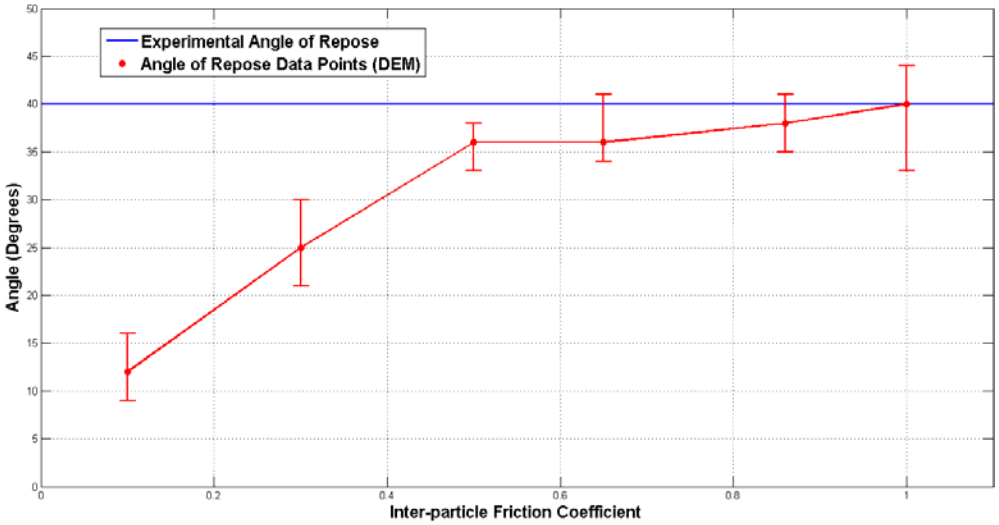

Figure 5.8 - Angles of Repose for Different Inter-particle Friction Coefficients

For the given particle size and shape distribution it was found that the inter-particle friction coefficients from 0.5 and upwards all resulted in numerical angles

of repose within 10% of the experimental result. When the inter-particle friction coefficient goes below 0.5, the numerical angle of repose decreased more rapidly, as shown in Figure 5.8. Thus, the inter-particle friction can be divided into two clear regions. Nakashima *et al*. (2011) also found two inter-particle friction regions for spherical particles that were used to model Toyoura sand: the lower region being where the inter-particle friction significantly affects the angle of repose and the higher region where the inter-particle friction has a much smaller effect on the angle of repose.

Since the angle of repose does not appear to change significantly at the high inter-particle friction region (for a certain particle size and shape distribution), it can be assumed that the angle of repose depends more on the particle size and shape distribution in this region. Dymond (2007) used the same material as used in this project and found that an inter-particle friction coefficient of 0.5 resulted in a numerical angle of repose which was for all practical purposes close enough to the experimental result of 40°. This corresponds well with the results obtained here and shown in Figure 5.8. Dymond (2007) used the angle of repose as part of his calibration procedure and ended up using an inter-particle friction coefficient of 0.5 as opposed to the value of 0.86 obtained in this project through direct shear tests. Dymond (2007) then used the calibrated micro properties to model dragline excavator bucket filling. Although he obtained satisfactory results, all the results indicated that the numerical material showed less resistance to bucket digging compared to the experimental results and observations. One reason for this might be that the inter-particle friction coefficient of 0.5 was too low, although the angle of repose test indicated that it might be accurate enough.

This could indicate that the angle of repose test is not a reliable test to calibrate micro friction properties for materials that exhibit high frictional and/or interlocking behaviour and that a test such as the direct shear test, in combination with an angle of repose test, would be more robust and reliable. If Dymond (2007) used an inter-particle friction coefficient of 0.86, his bucket filling results might have been even more accurate.

The specific inter-particle friction coefficient that divides the friction domain into its two regions is not entirely clear or predictable. Since this phenomenon appears for spherical particles as well as clumped particles, the exact point where the domain is split seems to be dependent on the particle size and shape distribution. How the particle size and shape distribution influences this point needs to be further investigated. This supports the suggestion that the angle of repose test might not be an appropriate test to directly calibrate the micro friction properties. As a verification tool, the angle of repose test can still prove to be useful. More research on the effect of particle size and shape distribution and its combined effect with inter-particle friction on the angle of repose is needed to support this conclusion.

5.2.5 Concluding Remarks: Angle of Repose Test

The angle of repose simulation using the calibrated micro properties resulted in an angle of repose that is within 5% of the experimental result. Based on this, the calibration procedure was successful and the angle of repose test can be seen as a useful verification tool.

There are two regions of inter-particle friction effects on the angle of repose, namely a lower friction region where it has a significant effect on the angle of repose and a higher friction region where the effect becomes minimal. This hampers the ability of the angle of repose test to directly calibrate the friction properties, since the exact division of the friction domain depends on a different micro parameter. This parameter is assumed to be the particle size and shape distribution; however more research is needed in this regard. Should this be the case, the angle of repose could be used to calibrate particle shape and size distribution more effectively. As far as the calibration of micro friction properties is concerned, the use of the direct shear test is proposed as the more reliable method, while the angle of repose test can be used to verify the results.

5.3 The Anchor Pull-out Test

The second verification test is a generic anchor pull-out test devised to resemble a typical application of bulk materials handling. The test entails embedding, or anchoring a structure in a packing of bulk material and then slowly pulling it out of the packing while measuring the resistance force of the material on the anchor as it is pulled out. This force is typically plotted against time or displacement and information such as the peak anchor force and force decay curve, retrieved.

In this project, the calibration procedure was performed with the anchor pull-out test in mind. Consequently, the normal stresses applied in the direct shear test were estimated to be within the range of stresses that the material in the anchor pull test might experience. Thus, by comparing the numerical results (using the calibrated micro properties) to the experimental results, the calibration procedures could be validated.

Most of the calibration process focused on the calibration of the inter-particle friction coefficient and particle stiffness. To make sure that the calibration procedure resulted in the correct values for these two properties, a sensitivity analysis was performed in which the inter-particle friction and particle stiffness were varied. Furthermore the effect of system parameters such as packing height and anchor pull velocity were also investigated.

5.3.1 Experimental Procedures

The experimental set-up with dimensions can be seen in Figure 5.9. The system consisted of a bin, in which an anchor was placed vertically. While keeping the

anchor stationary (and vertical) the bin was slowly filled with the bulk material under investigation, to a specified height, thus embedding the anchor in the material. The anchor was constructed from square tubing (50 x 50 x 3 mm), cut to a length of 1 000 mm, with a 110 x 110 x 5 mm mild steel plate welded to the one end (see Figure 5.9).

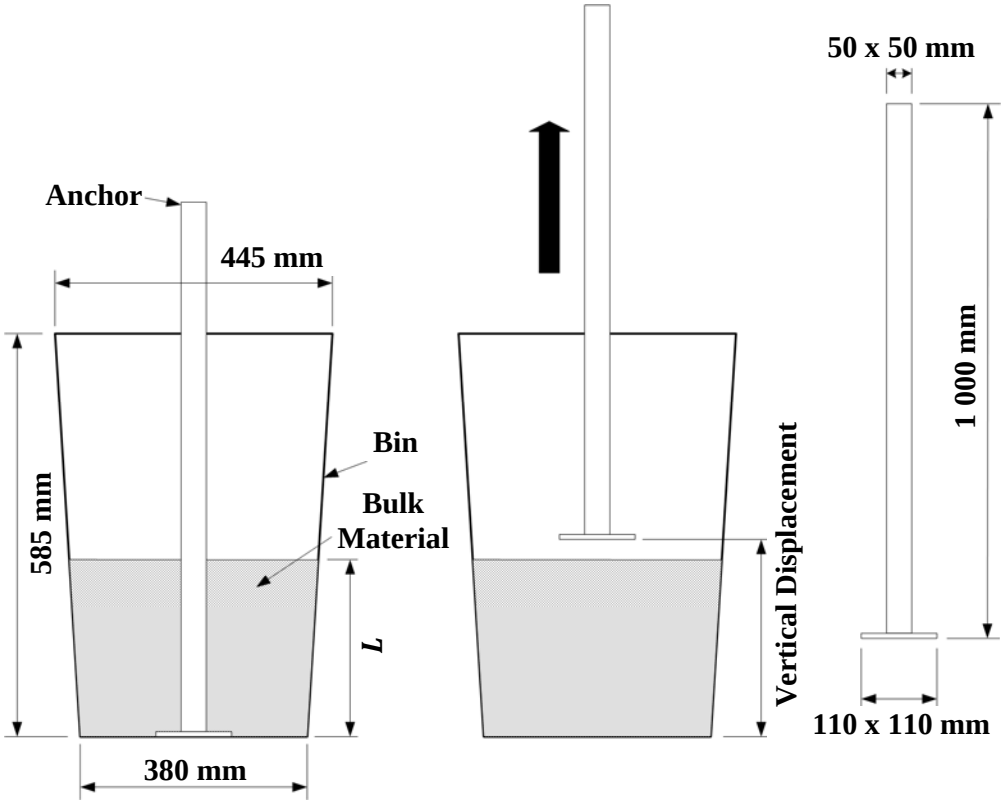

Figure 5.9 - Schematic Representation of Anchor Pull-out Test Set-up

A load cell was connected to the anchor, after which the anchor was pulled out of the packing with an overhead crane at a specified velocity. The resistance force as exerted on the anchor was recorded. The experimental set-up prior to execution can be seen in Figure 5.10. Four combinations of anchor velocities and packing heights were implemented in the test as shown in Table 5.4. Each combination was repeated three times to obtain an average result and to validate the repeatability of the experiments.

An HBM S9 50kN load cell was used, as used in the direct shear test, along with the HBM Spider8 data logger. The two anchor velocities were obtained from the vertical velocities of the overhead crane.

Table 5.4 – Packing Height and Anchor Velocity Combinations

Combination	Packing Height, *L* (mm)	Anchor Velocity (mm/s)
A	170	27
B	170	153
C	320	27
D	320	153

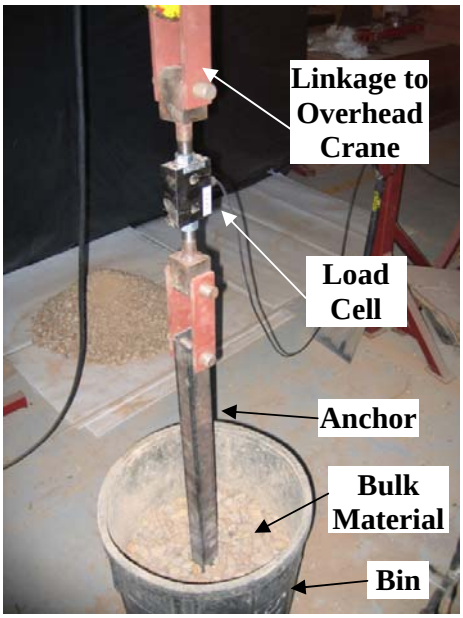

Figure 5.10 - Experimental Set-up Prior to Test

5.3.2 Numerical Procedures

The experimental set-up (Figure 5.9) was replicated in PFC^{3D} using the calibrated micro properties in Table 4.9). The particles were allowed to settle under gravity and then levelled to the specified packing height. The anchor was then accelerated to the desired velocity over a time period of 1 second after which the velocity was kept constant. The acceleration was implemented to resemble the initial acceleration of the overhead crane.

The typical progression of the anchor pull simulation can be seen in Figure 5.11. The combinations that were simulated are A and C (including the sensitivity analyses), together with D (to obtain system parameter effects).

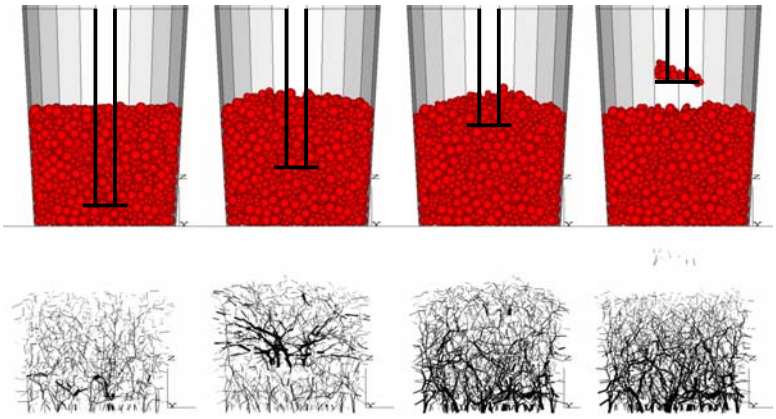

Figure 5.11 - Anchor Pull-out Test Simulation in Progress (with Contact Force Chains)

5.3.3 Comparison between Experimental and Numerical Results

For comparison purposes, only the experimental and numerical results of combinations A, C and D were considered. In Figure 5.12 the results for Combination A are shown, while the results for Combinations C and D can be observed in Figures 5.13 and 5.14.

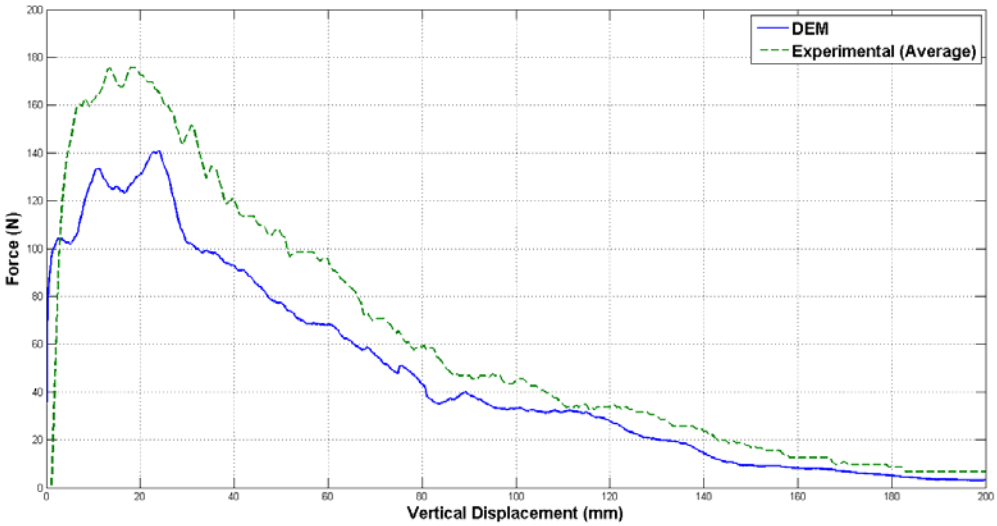

Figure 5.12 – Average Anchor Pull-out Test Results (Combination A)

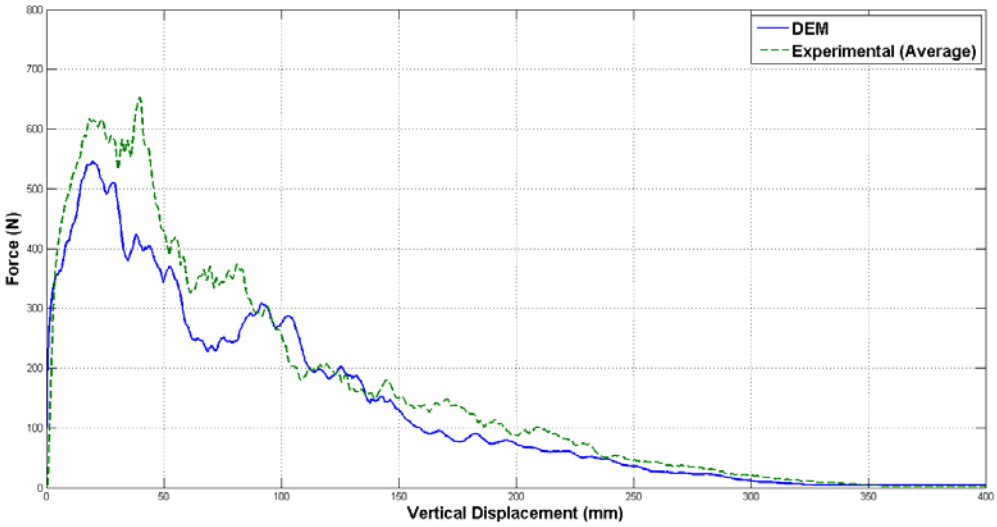

Figure 5.13 – Average Anchor Pull-out Test Results (Combination C)

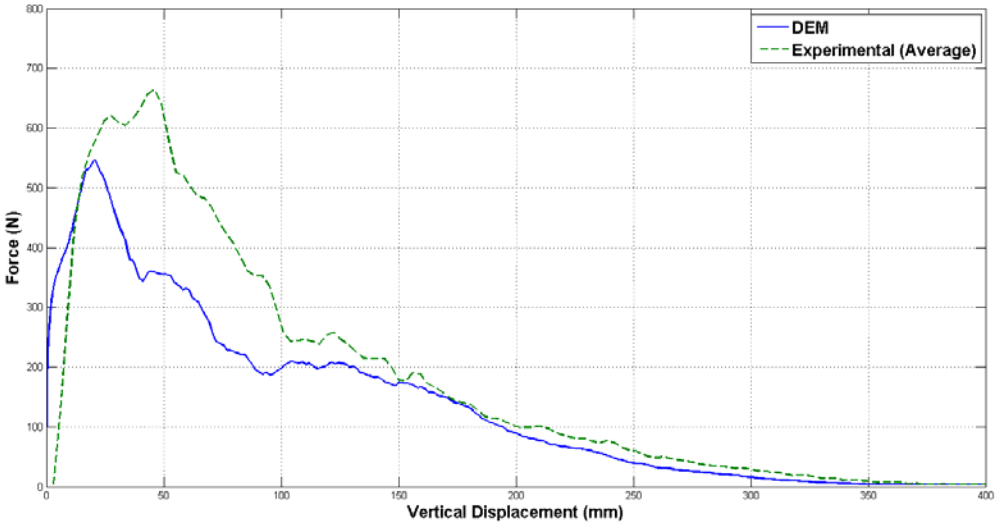

Figure 5.14 – Average Anchor Pull-out Test Results (Combination D)

It can be observed that the general trend of the numerical anchor force resembles that of the experimental force. Firstly, an initial phase is identified where the force increases rapidly towards a peak after which it decreases towards zero as the anchor is displaced vertically and the resulting load, due to the bulk material, decreases.

Since the initial phase of the displacement occurs very rapidly and entails a significant dynamic effect, it was not focused on in the subsequent analysis. However, the peak force and the decay of the force with increasing vertical displacement were used for comparison purposes.

From Figures 5.12, 5.13 and 5.14 it is seen that the peak force obtained numerically was lower than the experimental peak force for all three combinations. Regardless of the peak force, the force decay curves for the experimental and numerical results appeared to correspond well for all three cases. The offset in the decay curves between the numerical and experimental results can be attributed to the different peak forces. The experimental and numerical peak forces for the three combinations are summarized in Table 5.5.

Table 5.5 - Peak Anchor Forces

Combination	Peak Anchor Force (N)		% Variation
	Experimental	DEM	
A	175.6	140.8	19.8
C	652.6	545.5	16.4
D	664.6	546.1	17.8

The smallest percentage variation in the peak anchor force between the numerical and experimental results was obtained for Combination C (with a packing height of 320 mm and anchor velocity of 27 mm/s). Furthermore the force decay curves correspond very well between the experimental and numerical results for Combination C (Figure 5.13). The remaining combinations exhibited larger discrepancies between the numerical and experimental results. When the higher anchor velocity was implemented in PFC^{3D} (Combination D) a larger dynamic effect was present, which could result in the larger discrepancy between the numerical and experimental results. Also, for a lower packing depth (Combination A), the numerical result showed a larger discrepancy due to a large dynamic effect. This can be attributed to the global damping characteristics of the packing that will differ from one with a higher packing depth, due to fewer particles and therefore fewer contacts that are present. More research is needed to determine the cause of these larger discrepancies.

With the abovementioned taken into account, it can be concluded that, for a slower anchor velocity and deeper packing, the numerical and experimental results for the anchor pull test correspond very well. For the other scenarios where a higher velocity and lower packing depth were implemented, the numerical and experimental results do not show the same similarity. However, the overall similarity of the numerical and experimental results for the anchor pull-out test can still be regarded as adequate, given the limitations of the numerical damping implementations. All the calibration tests (CCT and DST) assumed quasi-static conditions, and it was assumed to be independent of the damping ratio used. Using higher anchor velocities might induce dynamic effects not accurately modelled by the damping ratio used while with lower anchor velocities, the damping effects might not be so dominant, hence the more accurate numerical results. In future work, a method of calibrating the damping ratio should be included in the calibration procedure.

Since the numerical results for the anchor pull-out test, using the calibrated micro properties, correspond satisfactorily with the experimental results, the calibration procedure in general can be regarded as successful. To further validate the calibration process, a sensitivity analysis was done where the particle stiffness and inter-particle friction were varied from the calibrated values in an attempt to obtain micro property sensitivities of an anchor pull-out test simulation.

5.3.4 Micro Property and Test Parameter Sensitivity

For the sensitivity analysis, the effects of inter-particle friction and particle stiffness on the numerical anchor pull-out test results were investigated. The relevant micro properties were varied while the remaining properties were kept the same as the calibrated micro properties. Furthermore the effect of the packing depth and anchor velocity on the numerical anchor pull-out test results was also investigated. This was done by comparing the results from Combinations A, C and D directly, using the same (calibrated) micro properties.

Particle Stiffness

The particle stiffness values were varied from the calibrated value of 1.72 MN/m to 1.0 MN/m and 2.3 MN/m respectively. The anchor pull-out test simulations were then performed for both Combinations A and C.

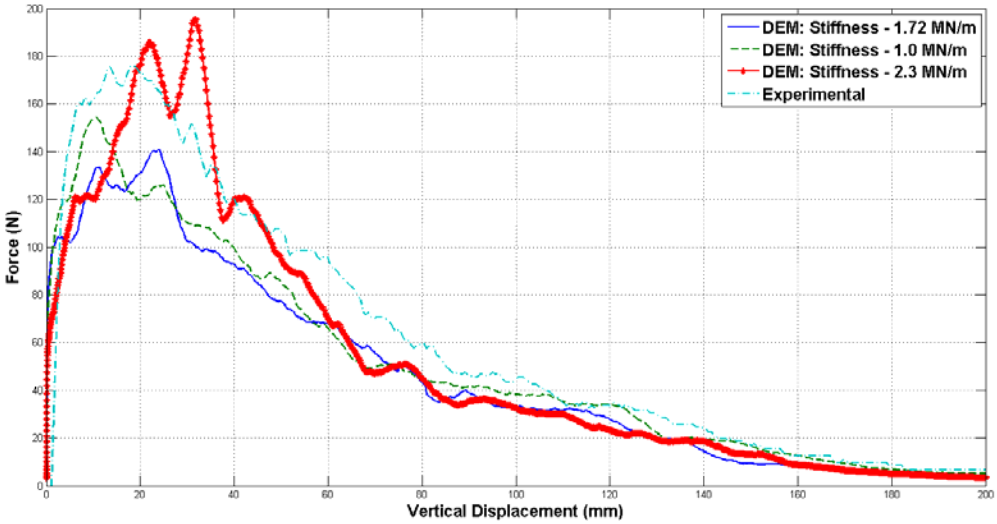

Figure 5.15 - Stiffness Sensitivity (Combination A)

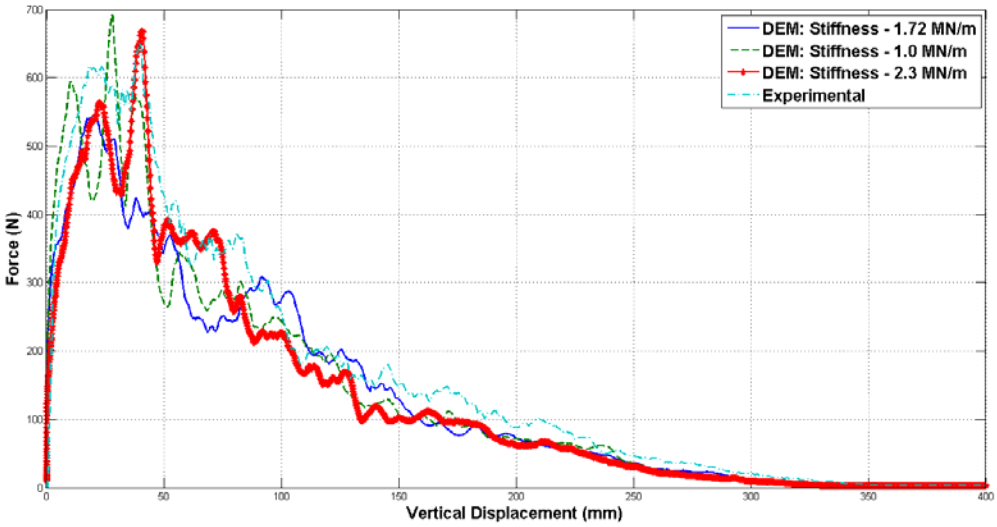

Figure 5.16 - Stiffness Sensitivity (Combination C)

From Figures 5.15 and 5.16 it appears that the stiffness sensitivity increases with a decrease in packing depth. The sensitivities also seem to affect the peak forces more than the decay curves for both cases to the point that the sensitivity of the decay curve to particle stiffness is negligible. In Table 5.6 the peak forces and percentage variations (from the experimental result) for both combinations are shown.

Table 5.6 - Particle Stiffness Sensitivity

	Experimental (N)	DEM					
		1.72 MN/m		1.0 MN/m		2.3 MN/m	
		Force (N)	%	Force (N)	%	Force (N)	%
A	175.6	140.8	19.8	154.5	12.0	195.3	11.2
C	652.6	545.5	16.4	692.6	6.1	668.3	2.4

In both cases it can be seen that, as the particle stiffness is changed, the peak anchor force moves closer to the experimental peak force than that of the calibrated stiffness. This could be an indication that the validity of the calibrated particle stiffness is questionable when considering the peak forces. Should the decay curves with their limited sensitivity be considered, the calibrated particle stiffness of 1.72 MN/m could still be regarded as valid. The negligible sensitivity of the decay curves to stiffness could also be used as an indication that the anchor pull-out test is not sensitive to particle stiffness, regardless of the visible peak force sensitivity.

Inter-particle Friction

For the inter-particle friction sensitivity analysis, friction coefficients of 0.5 and 1.0 were implemented as a variation from the calibrated value of 0.86. Again, the

simulations were performed for both Combinations A and C (see Figures 5.17 and 5.18).

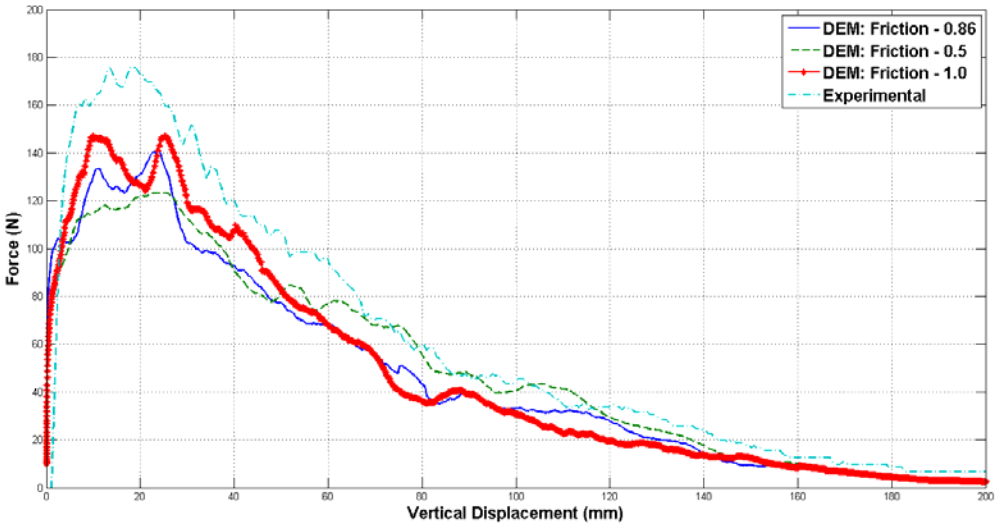

Figure 5.17 – Friction Sensitivity (Combination A)

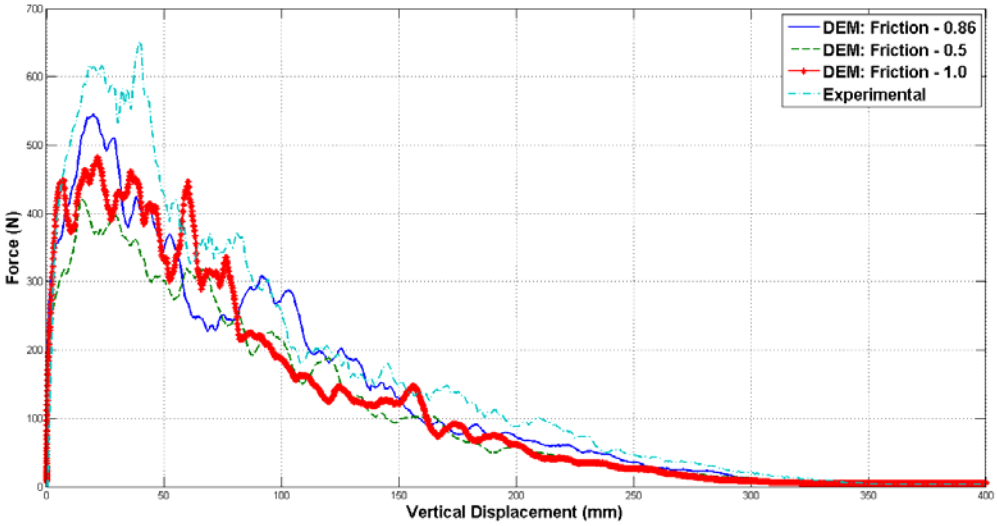

Figure 5.18 - Friction Sensitivity (Combination C)

From Figures 5.17 and 5.18, the inter-particle friction appears to have an effect on the anchor pull-out simulation results. A clear variation in peak anchor force can be observed. However, the decay curves do not seem to be affected significantly by the friction. A summary of the peak anchor forces and percentage variations from the experimental result are shown in Table 5.7.

Table 5.7 - Inter-particle Friction Sensitivity

	Experimental (N)	DEM					
		0.86		0.5		1.0	
		Force (N)	%	Force (N)	%	Force (N)	%
A	175.6	140.8	19.8	123.6	29.6	147.2	16.2
C	652.6	545.5	16.4	421.4	35.4	481.6	26.2

From Table 5.7 it can, in general, be concluded that if the inter-particle friction is changed from the calibrated value, the peak force moves further away from the experimental peak force. It can therefore be established that there is a substantial sensitivity for inter-particle fiction and that the calibrated friction gives a peak force, and subsequent decay curve that is closest to the experimental result. Taking this into account the calibrated inter-particle friction coefficient of 0.86 can also be regarded as valid.

Anchor Velocity and Filled Depth

From the numerical anchor pull-out test results in Figure 5.19 it can be seen that, for a certain packing depth, the anchor velocity has a negligible effect on the peak anchor force (as seen for Combinations C and D). The decay curves also seem not to be affected significantly.

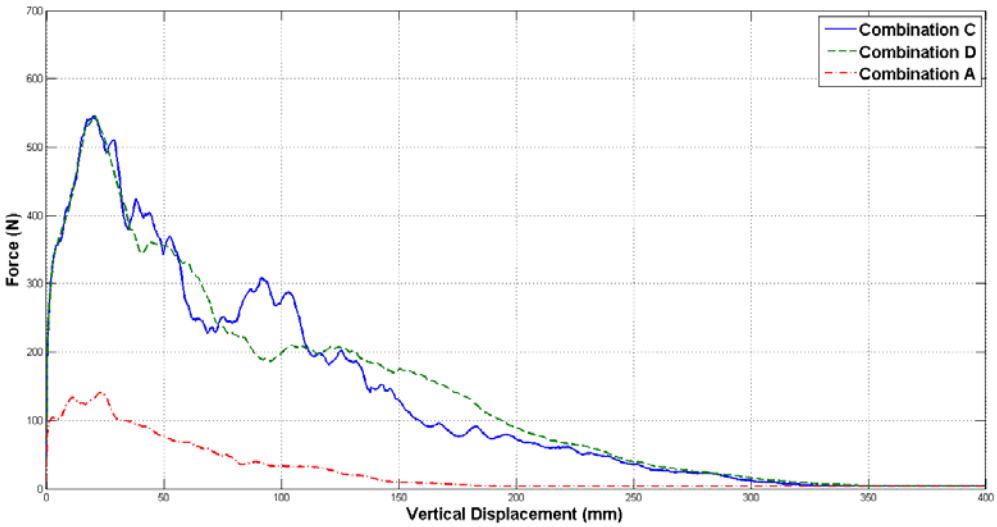

Figure 5.19 - Numerical Anchor Pull-out Results

For a certain anchor velocity, a change in the packing depth appears to affect the peak anchor force substantially while the decay curve also seems to change (see Combinations A and C). The same trend can be observed in Figure 5.20, for the experimental anchor pull-out test results. Thus, for the packing depths, anchor velocities and bulk material under investigation, it can be concluded that the anchor pull-out test is more sensitive for the packing depth than the anchor velocity. More research is however needed to verify this.

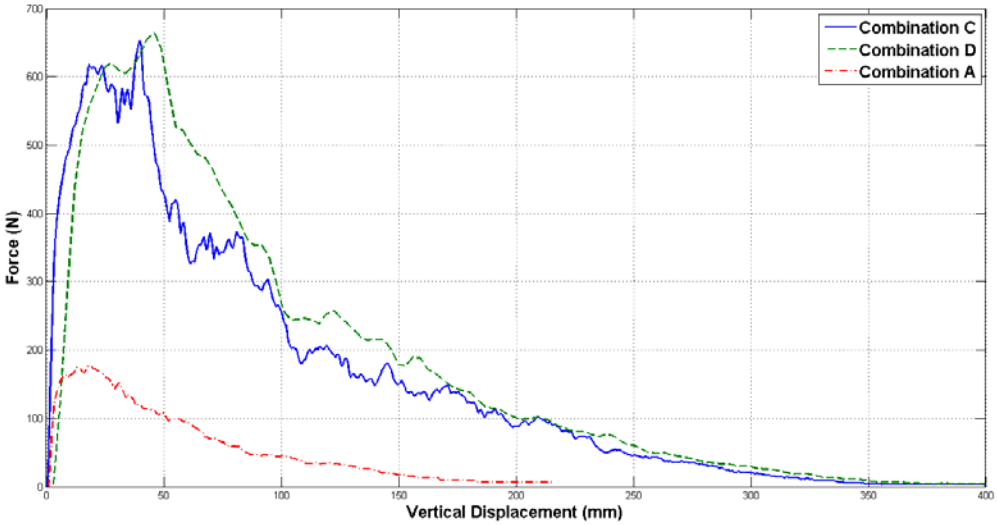

Figure 5.20 - Experimental Anchor Pull-out Results

5.3.5 Concluding Remarks: Anchor Pull-out Test

For the three scenarios (A, C and D) of packing depth and anchor velocity, the anchor pull-out test simulations using the calibrated micro properties, produced results that correspond well to the experimental results. Considering the numerical limitations of the simulations (in terms of the damping characteristics), this serves as an indication that the calibration procedure was successful.

To further investigate the validity of the calibrated micro properties and the applicability of the anchor pull-out test as a verification tool, a sensitivity analysis was done. The sensitivity of the numerical anchor pull-out test results to particle stiffness and inter-particle friction was investigated.

It was found that the anchor pull-out test is not significantly sensitive to particle stiffness under the specific test conditions. Thus, the ability of this test to verify the calibrated particle stiffness could be regarded as not being sufficient enough.

As far as the inter-particle friction is concerned, a clear sensitivity was observed in the anchor pull-out test. The calibrated friction, along with the other calibrated properties, produced a numerical result closer to the experimental result than for the other friction coefficients. This friction sensitivity is expected due to the anchor pull-out test effectively being a dry bulk flow application and that dry bulk flow is dominated by inter-particle friction. As a tool to verify the calibrated micro friction, the anchor pull test can be very useful.

In general, the sensitivity of the anchor pull-out test simulation to the micro properties appears to be substantial enough to support it in its ability as a verification tool. Should a good correspondence be obtained between

experimental and numerical results (using the calibrated micro properties), the sensitive nature of the anchor pull-out test can provide added assurance that the calibrated micro property values are indeed reliable.

Taking this into account for the calibration procedure for this project, the DEM input parameter values obtained can thus be considered reliable and valid for further use in other simulations.

6. Conclusions

The discrete element method (DEM) is widely used to model bulk materials handling. However, the accuracy of the models is dependent on the input parameters and specifically the material properties. There are no standardised methods or procedures for obtaining the parameter values for a given material. The main objective of this project was to calibrate the DEM input parameters for a given coarse aggregate with particle sizes up to 40 mm as typically found in the mining and quarrying industries.

A large scale shear box with a diameter of 590 mm and a height of 330 mm was developed and used to perform direct shear tests on the material. The design of the shear box was such that confined compression tests could also be conducted using the same apparatus.

With the shear box as the main experimental apparatus, a calibration procedure was devised and implemented. This included the direct measurement of the particle size, particle density, the material bulk density and hence the porosity. The different particle shapes were identified through visual inspection. The shear box was used to obtain the confined Young's Modulus and the internal friction angle of the material.

DEM models, equivalent to the experimental set-up, were then developed. Through an iterative procedure, the input parameter values were varied one at a time, and the bulk response recorded. The calibrated set of parameter values was defined as the set that resulted in a bulk response closest to the experimental measurements. The bulk density could be accurately modelled within 1% of the measured value, the porosity within 4%, the confined Young's Modulus within 20% and the internal friction angle within 1% of the measured values.

The calibrated input parameter values were then verified through a series of verification experiments and simulations. An anchor pull-out test was used to measure the vertical pull-out force of an anchor imbedded in the material. A very good correlation between the experimental and DEM results was obtained. A sensitivity analysis was also conducted in which the simulations were repeated using input parameter values higher and lower than the calibrated values. The overall results from the calibrated set of parameter values compared best to the experimental results and confirmed the accuracy of the calibration procedure.

A further verification of the calibration procedure was performed in the form of angle of repose experiments and simulations. Again, a good correlation between the experimental and numerical results was obtained. An observed sensitivity of the simulated angle of repose for the input parameter values provided an additional indication that the calibration results were indeed accurate.

The combination of the test equipment developed, the calibration procedure and the DEM models developed form a useful tool for the calibration of DEM input parameters. The benefits of efficient calibration strategies for industry and advanced academic research are significant. Using the outcomes of this project, further research and development can be done to evolve these technologies to the extent where engineers in the bulk material handling industries can use it to design, model and optimise equipment and processes.

Appendix A: A DOE Micro Property Effects Study

A.1 Introduction

The numerical component of a bulk material calibration process is hampered by the computationally intensive iterations in which the relevant micro properties are "optimised". As explained in Chapter 4, the micro properties for this project were obtained by means of manual iterations based on linear interpolations. However, a more efficient iterative approach is needed to optimise the micro properties more quickly.

A popular technique to obtain numerical responses that can provide more insight into the bulk behaviour is by using the so-called design of experiments (DOE) methods. A properly implemented DOE approach should enable the researcher to better understand the effects of the micro properties that need to be optimised on the relevant bulk property. This can ultimately form the basis from which a more efficient optimisation approach can be developed to obtain the appropriate micro properties. Curry *et al.* (2009) proposes such a systematic approach in which a design of experiments series of tests is performed (using DEM) to determine the appropriate micro properties for a certain bulk parameter. This bulk parameter is also measured experimentally to obtain an objective function for an optimisation scheme. In the optimisation scheme a number of DEM simulations are executed and the results compared to the objective function. The micro properties are then also varied according to the optimisation algorithm until the difference between the DEM result and the objective function is minimised (Curry *et al*. 2009).

In a DOE investigation a response, or dependent variable, is measured or simulated in a controlled manner. This controlled manner entails performing the measurement or simulation by controlling a number of independent variables, or factors. According to the general DOE strategy, different combinations of factor levels (values) are implemented, each time obtaining the response for that combination. These factor level combinations are more commonly known as treatment combinations. With the responses known for the different treatment combinations, the effect of each independent variable on the response can be determined. The effects can be used to derive analytical models, or the empirical data used to good effect in further design optimisation. Design of experiments can be generalised as a method for doing an experiment in a pattern instead of one at a time, with the benefit of obtaining more and better information from the data than from more conventional experimenting. It could also be described as "statistically optimised experimentation" (Del Vecchio, 1997).

In this project a half fractional factorial design (of a 2^4 full factorial design) was implemented to numerically obtain the effects of the particle density, particle stiffness, inter-particle friction and particle-wall friction on the bulk density, porosity, Confined Young's Modulus and internal friction angle of a bulk material sample. The effects were then used to derive linear regression models with which

the behaviour of the mentioned bulk parameters can be predicted more effectively. The linear regression models obtained were then tested to evaluate their ability to predict the bulk behaviour.

The focus for this part of the project was only to implement a design of experiments analysis to identify the important micro parameters that affect certain bulk parameters. The subsequent optimisation of the micro properties, in order to calibrate them, was not done due to time constraints. In further research more emphasis can be placed on the formal optimisation of the micro properties.

In this appendix the half fraction factorial design approach is discussed, along with its implementation for this project. The effects of the micro properties on the applicable bulk parameters and the linear regression models are covered in detail, together with the regression model evaluations. Furthermore the effects of particle size and shape, container size and shear velocity (in the case of the direct shear test) on the mentioned bulk parameters are also discussed.

A.2 Half Fraction Factorial Design, ANOVA and Regression Analysis

To determine the most prominent factors that have an effect on the bulk responses that form part of the investigation, the very popular DOE approach of factorial design was used. This procedure is also known as a screening procedure. In this section the concepts behind factorial design are briefly discussed. Furthermore the technique of half fraction factorial design is also discussed in the context of how it was applied in this investigation. The effects of the various factors on the responses were determined and the results used to generate multiple linear regression models. Additionally, formal statistical analysis could be done on the models in the form of analysis of variance (ANOVA) in an attempt to test the capabilities of the regression models as estimators of the examined processes (responses).

A more detailed explanation into design of experiments (focussing on full factorial and half fraction factorial designs) and regression analysis can be found in Vining (1998) and Del Vecchio (1997).

A.2.1 Full Factorial Design

In order to determine the relationship between a number of micro properties on a certain bulk material property, the most appropriate strategy would be to systematically manipulate the micro properties and then to observe the response (Vining, 1998). The micro properties are known as the factors (variables, or more specifically design variables or independent variables), while the bulk property is called the response (dependent variable). The manipulation of the factors needs to take place according to a well defined strategy, which is determined by the experimental design. The most important goal of this strategy is to single out the

effects due to each factor (Vining, 1998). The specified values of the factors as they are manipulated in the experiment are called the levels. Normally, two to three levels are used per factor. In the case of two levels, we may designate them as a high level (or +1, in experimental design units) and as a low level (-1). A so-called treatment combination is a specific, distinct combination of the levels for each factor. Each time a treatment combination is implemented, it is called an experimental run, and a series of runs constitutes an experimental design (Vining, 1998).

If it is expected that there are *k* factors that may have an influence on a process, an experimental design can be planned in which two levels per factor are implemented. This experimental design is known as a 2^k full factorial design, where the "2" indicates the number of levels implemented and *k* indicates the number of factors considered. This means that there is a total of 2^k distinct treatment combinations, since a full factorial consists of every possible treatment combination of the two levels for the *k* factors (Vining, 1998). To illustrate this, assume that there are three factors (*A*, *B* and *C*) that influence a certain bulk property, *y*. If we implement two levels per factor, the experimental design becomes a 2^3 full factorial design, with eight distinct treatment combinations. The eight distinct treatment combinations can be observed in Table A.1, in design units.

Table A.1 - Treatment Combinations for a 2^3 Full Factorial Design in Design Units

Runs	*A*	*B*	*C*	*y*
1	+1	+1	+1	y_1
2	-1	+1	+1	y_2
3	+1	-1	+1	y_3
4	-1	-1	+1	y_4
5	+1	+1	-1	y_5
6	-1	+1	-1	y_6
7	+1	-1	-1	y_7
8	-1	-1	-1	y_8

When the eight runs have been executed and the responses obtained, the effects of the factors on the response can be calculated as in Equation A.1 (in the case of factor *A*):

$$\text{Effect of } A = \frac{y_1 - y_2 + y_3 - y_4 + y_5 - y_6 + y_7 - y_8}{4} \qquad \text{(A.1)}$$

Here, the signs of the design unit in the particular column (column *A*) are multiplied with the response for each corresponding run. These eight products are then added together and the total divided by four (since we have $2^3 = 8$ treatment combinations). The effects of factors *B* and *C* are also calculated in the same fashion.

In many cases it is found that the factors can interact, that is the effect of a factor depends on the level used for another factor. To account for possible factor interactions, Table A.1 above can be expanded to include the different factor interactions (see Table A.2).

Table A.2 - Full Factorial Design (2^3) Expanded to Include Factor Interactions

Runs	*A*	*B*	*C*	*AB*	*AC*	*BC*	*ABC*	*y*
1	+1	+1	+1	+1	+1	+1	+1	y_1
2	-1	+1	+1	-1	-1	+1	-1	y_2
3	+1	-1	+1	-1	+1	-1	-1	y_3
4	-1	-1	+1	+1	-1	-1	+1	y_4
5	+1	+1	-1	+1	-1	-1	-1	y_5
6	-1	+1	-1	-1	+1	-1	+1	y_6
7	+1	-1	-1	-1	-1	+1	+1	y_7
8	-1	-1	-1	+1	+1	+1	-1	y_8

Here, *AB* designates the interaction between factors *A* and *B*; *AC* the interaction between *A* and *C* and *BC* the interaction between *B* and *C*. These are also known as second-order interactions. *ABC* implies the interaction between factors *A*, *B* and *C* (third-order interaction). The design units for the interaction columns are obtained by multiplying the design units of the underlying columns (the columns making up the particular interaction) with each other. The effect of each interaction can also be calculated as was done for the main factor effects.

The quantified effects can be represented visually by means of a so-called scree plot, where all of the effect values are plotted relative to one another. This allows for a useful manner to identify any significant factors and interactions (Del Vecchio, 1997). Another technique to visually represent the effects is the normal probability plot, which is also very useful when there is not an appropriate error term in subsequent regression analysis (Vining, 1998). It is also a powerful technique if the assumption of effect sparsity holds true, which means that we rarely expect all of the effects to be large in absolute value, or of equal absolute size (Vining, 1998). These visual aids are very useful to single out the most important factors (and possible interactions) from the least important ones.

The results typically obtained can be used to formally construct a linear regression model for the process (or bulk property) as a linear function of its factors. A linear regression model that supports a 2^3 factorial design has the following form:

$$y_i = \beta_0 + \beta_A x_{iA} + \beta_B x_{iB} + \beta_C x_{iC} + \beta_{AB} x_{iA} x_{iB} + \beta_{BC} x_{iB} x_{iC} + \beta_{AC} x_{iA} x_{iC} + \beta_{ABC} x_{iA} x_{iB} x_{iC} + \varepsilon_i \qquad i = 1,2,\ldots,8 \qquad \text{(A.2)}$$

Where

- y_i is the response estimation for the i^{th} run.
- β_0 is the y-intercept, which is the average of the responses.
- β_A is the regression coefficient associated with factor *A*.

- β_B is the regression coefficient associated with factor *B*.
- β_C is the regression coefficient associated with factor *C*.
- β_{AB} is the regression coefficient associated with the two-factor interaction *AB*.
- β_{BC} is the regression coefficient associated with the two-factor interaction *BC*.
- β_{AC} is the regression coefficient associated with the two-factor interaction *AC*.
- β_{ABC} is the regression coefficient associated with the three-factor interaction *ABC*.
- x_{iA} is the value of factor *A*, for the i^{th} run.
- x_{iB} is the value of factor *B*, for the i^{th} run.
- x_{iC} is the value of factor *C*, for the i^{th} run.
- ε_i is the random error associated with the i^{th} run.

In order to properly account for random error, ideally, more than one run per treatment combination should be performed. This form of replication is not always possible due to time constraints and other economic reasons. A useful characteristic of the full 2^k factorial designs is that they exhibit hidden replication (Vining, 1998). This is based on the concept that, for a full factorial design, there is at least one factor (or interaction) of which the effect is not important. Since we do not know which factor it is at initial planning, we still include it in the design. Thus by including this factor we provide for replication in the experiment. This then allows for the effect of that insignificant factor to be used to approximate an error term in the regression model.

To formally test the regression model in its capability to predict the response at hand, an analysis of variance (ANOVA) investigation can be done on the data. This will ultimately show if the model is appropriate, that is if there is at least one factor that does affect the response and if so, which one it is.

When we have continuous factors in our investigation, we are often interested in what the responses are for factor settings in between those used for the experiment (in other words, in between the -1 and +1 levels). This can be done by adding so-called centre runs to the design. As the name implies, centre runs use the levels for the factors in the exact centre of the experimental region (Vining, 1998). The exact centre is the average of the low and high levels. Centre runs are used for a variety of reasons according to Vining (1998), including to serve as a reality check (to see if the response does behave as expected within the experimental range). Other uses are to provide replication to enable us to estimate an error term and also to check for possible curvature (non-linear behaviour).

In this investigation a centre run evaluation was performed afterwards in an attempt to identify any possible non-linear behaviour and to check the regression models' prediction capabilities.

A.2.2 Half Fraction Factorial Design

When working with full 2^k factorial designs it can be seen that as the number of factors, *k*, increase, the number of runs also increases significantly. This can result in very large numbers of runs, even for relatively small numbers of factors which (more often than not) prohibits full factorial design due to economical and time constraints.

To reduce the total number of treatment combinations, fractional factorial designs can be used. In fractional factorial designs the basic factorial structure of the experiment is still preserved (Vining, 1998). As explained in Vining (1998), factional factorial designs use the "main effects" principle to reduce the number of treatment combinations. This principle states that main effects tend to dominate two-factor interactions, two-factor interactions tend to dominate three-factor interactions, and so on. Full 2^k factorial designs allow us to estimate all of the interactions. As *k* gets larger, more of these interactions become less important. Fractional factorial designs essentially sacrifice the ability to estimate the higher-order interactions in order to reduce the number of treatment combinations (Vining, 1998).

Using the "main effects" principle, the highest order interaction is generally regarded to be insignificant. With this in mind, half fractions are used to extend the number of factors in a design. For example, a half fraction of the 2^4 (that is, a 2^{4-1}) design can be generated from a 2^3 full factorial design. This is illustrated in the following scenario.

Consider the 2^3 full factorial design as in Table A.2. If we assume that the three-factor interaction, *ABC*, is not important (the "main effects" principle), then we can use the *ABC* column to determine the settings for a fourth factor *D*. We make *D* = *ABC*, as in Table A.3, thus aliasing *D* with the *ABC* interaction. Under modulo 2 arithmetic, the defining interaction is *ABCD* (Vining, 1998).

Table A.3 - Full Factorial Design (2^3) with Added Factor to form Half Fraction Design (2^4)

Runs	*A*	*B*	*C*	*AB*	*AC*	*BC*	*D* (=*ABC*)	*y*
1	+1	+1	+1	+1	+1	+1	+1	y_1
2	-1	+1	+1	-1	-1	+1	-1	y_2
3	+1	-1	+1	-1	+1	-1	-1	y_3
4	-1	-1	+1	+1	-1	-1	+1	y_4
5	+1	+1	-1	+1	-1	-1	-1	y_5
6	-1	+1	-1	-1	+1	-1	+1	y_6
7	+1	-1	-1	-1	-1	+1	+1	y_7
8	-1	-1	-1	+1	+1	+1	-1	y_8

By following this approach, we added another factor to the design, while keeping the total number of experimental runs the same. Since we have four factors that are considered in a structure normally associated with three factors, it is important

to note that there is aliasing that takes place in the design (Vining, 1998). If two factors (or interactions) are aliased, the estimates of their effects are the same. We thus cannot uniquely estimate either. With *ABCD* as the defining interaction, we say that it is aliased with the intercept (of the regression model) and we have sacrificed it (we have lost our ability to estimate its effect). We can use modulo 2 arithmetic to construct an alias structure for the abovementioned half fraction factorial design (see Table A.4). Note that $I = ABCD$ reads "*ABCD* is aliased with the intercept", as in Vining (1998). Also note the aliasing between factor *D* and the *ABC* interaction, as discussed earlier.

Table A.4 - Alias Structure for 2^4 Half Fraction Factorial Design

I	=	*ABCD*
A	=	*BCD*
B	=	*ACD*
C	=	*ABD*
D	=	*ABC*
AB	=	*CD*
AC	=	*BD*
BC	=	*AD*

From Table A.4 it is seen that the interactions with which the main factors and second-order interactions in the design are aliased with are not present in the design, as is evident from Table A.3. We thus do not have to be able to estimate them, according to the design. It is also seen that the main effects are not aliased with any second-order interactions or vice-versa. The alias structure tells us the largest regression model that we can estimate from the experiment. For this case we can have a term associated with the intercept, *I*, the main effects (*A*, *B*, *C*, and *D*) and the second-order interactions (*AB*, *AC* and *BC*). The second-order interactions with *D* and the higher-order interactions (third-order and fourth-order) cannot be estimated due to aliasing (Vining, 1998). Since it is generally assumed that higher-order interactions are not important, this does not pose a problem. In its final form, the half fraction of the 2^4 design can be represented as follows (note the eight distinct treatment combinations for the four factors, highlighted in gray, in Table A.5):

Table A.5 - Final Half Fraction Factorial Design (2^4)

Runs	***A***	***B***	***C***	***D***	***AB***	***AC***	***BC***	***y***
1	+1	+1	+1	+1	+1	+1	+1	y_1
2	-1	+1	+1	-1	-1	-1	+1	y_2
3	+1	-1	+1	-1	-1	+1	-1	y_3
4	-1	-1	+1	+1	+1	-1	-1	y_4
5	+1	+1	-1	-1	+1	-1	-1	y_5
6	-1	+1	-1	+1	-1	+1	-1	y_6
7	+1	-1	-1	+1	-1	-1	+1	y_7
8	-1	-1	-1	-1	+1	+1	+1	y_8

The main effects for the four factors (*A*, *B*, *C* and *D*) and the three second-order interactions (*AB*, *AC* and *BC*) can be determined as explained earlier in this section. The results can also be used to derive a multiple linear regression model, for the process, as dictated by the aliasing limitations.

For this project a half fraction of the 2^4 design (2^{4-1}) was generated from a full 2^3 factorial design and this design was implemented for a number of responses. Four factors were thus considered. The effects of the main factors and their relevant second-order interactions were calculated as explained earlier. Visual representation of the effects was performed by means of scree plots and normal probability plots. Then, using multiple linear regression analysis, regression models were generated for these responses that include terms associated with all the relevant factors and second-order interactions. The concept of centre runs was also implemented to test the regression models.

To further test the capabilities of the regression models to estimate the responses at hand, formal analysis of variance (ANOVA) could be used. However, since the models for this project have as many regression coefficients as there are experimental runs (that is, eight) it was not possible to estimate an error term. This did not allow for any formal tests or analyses to be performed. Using the concept of hidden replication, where it is assumed that there is at least one factor (or interaction) that is not important in the design, those terms associated with insignificant effects were then used to account for random error in the process.

Del Vecchio (1997) also highlights that an underlying assumption of ANOVA is a uniform level of variability throughout the experimental volume. This implies that the standard deviation of the response is the same for all experimental conditions. Since this is mostly not true in practise, the interpretation of the data can be affected (Del Vecchio, 1997). Taking this into account, the regression models in this investigation were thus not formally tested using ANOVA, where parameters such as the coefficient of determination (R^2), *t*- and *F*-statistics typically provide more insight into the capabilities of the regression models. In future work a more comprehensive investigation into the use of these advanced techniques in the development of regression models can be conducted. The main aim of this investigation was to obtain the most prominent micro parameter effects on the relevant bulk properties and to construct basic regression models from which more advanced future work can be done. A very basic evaluation of the regression models' performance was thus deemed adequate (as seen later in this appendix).

A.3 Micro and Bulk Properties and Simulation Parameters

The same micro and bulk properties were considered for the DOE investigation as that for the calibration procedure in Chapter 4. Four micro properties were used, namely the particle density, ρ_p, inter-particle friction, μ_{pp}, particle-wall friction, μ_{pw}, and particle stiffness, k_p. The effects of particle size and shape as well as container size and shear velocity (in the case of the direct shear test) were

determined in a separate investigation. The bulk properties are the bulk density, ρ_b, confined Young's Modulus, E', and internal friction angle, ϕ, as in the calibration procedure. Additionally the porosity, n, was also considered among the bulk parameters. The voids ratio, bulk stiffness and angle of dilatancy were not considered due to their conceptual dependence on the other bulk parameters.

The simulations, and subsequent data processing, used to determine the abovementioned bulk properties are the same as used for the calibration procedure (Chapter 4). However, for this investigation spherical particles with a constant radius of 20 mm were used in PFC^{3D} and the cylindrical container radius and packing height were changed to 200 mm and 370 mm respectively.

For each micro property two levels were implemented, resulting in a total of 16 (2^4) treatment combinations, or unique set of micro property values. Using the approach of half fraction factorial design the total number of treatment combinations was reduced to 8 (2^{4-1}). The levels for each micro property are shown in Table A.6:

Table A.6 - Micro Property Assignments and Levels

Factor	Micro Property	Low Level (-1)	High Level (+1)
A	ρ_p (kg/m^3)	2 000	20 000
B	μ_{pp}	0.05	0.5
C	μ_{pw}	0.01	0.045
D	k_p (MN/m)	1.0	2.0

For the eight treatment combinations the following properties remained constant (Table A.7):

Table A.7 - Additional Simulation Parameters

Wall Stiffness (MN/m)	10
Particle Shape	Spherical
Particle Radius (mm)	20
Average Number of Particles	836
Container Radius (mm)	200
Packing Depth (mm)	370
Lid Velocity (CCT) (mm/s)	1
CCT Normal Force (N)	8 415
Shear Velocity (DST) (mm/s)	0.3
Shear Displacement (mm)	39
DST (Initial Compression) (N)	8 415
DST 1st Load (N)	1 885
DST 2nd Load (N)	3 495
DST 3rd Load (N)	5 105
DST 4th Load (N)	6 760

A.3.1 Design of Experiments Summary

The half fraction of the 2^4 design, as implemented for this investigation, is shown in Table A.8. Note the eight distinct treatment combinations of the levels for the four factors.

Table A.8 - Half Fraction Factorial Design (2^4) for Micro Property Effect Investigation

	In Natural Units				In Design Units (Levels)						
	A	***B***	***C***	***D***	***A***	***B***	***C***	***AB***	***AC***	***BC***	***D (ABC)***
	ρ_p	μ_{pp}	μ_{pw}	k_p							
0000	2 000	0.05	0.01	1.0	-1	-1	-1	+1	+1	+1	-1
1001	20 000	0.05	0.01	2.0	+1	-1	-1	-1	-1	+1	+1
0101	2 000	0.5	0.01	2.0	-1	+1	-1	-1	+1	-1	+1
1100	20 000	0.5	0.01	1.0	+1	+1	-1	+1	-1	-1	-1
0011	2 000	0.05	0.045	2.0	-1	-1	+1	+1	-1	-1	+1
1010	20 000	0.05	0.045	1.0	+1	-1	+1	-1	+1	-1	-1
0110	2 000	0.5	0.045	1.0	-1	+1	+1	-1	-1	+1	-1
1111	20 000	0.5	0.045	2.0	+1	+1	+1	+1	+1	+1	+1

In Table A.8, each run is designated by four digits. The first digit represents the level for factor *A*, the second digit that for factor *B*, and so on. It must be noted here that "1" indicates the higher level and "0" the lower level. The level definitions as discussed in Section A.2 are still used in the subsequent data processing.

As is also seen from Table A.8, factor *D* is the "new" factor that was added to the design (*D* = *ABC*). Taking into account that it is not possible to estimate any interactions with factor *D* due to aliasing, the particle stiffness, k_p, was associated with this factor. This was done based on the assumption that although particle stiffness alone could have a large effect on the said responses, its interactions with the other factors will be insignificant. The interactions between the remaining factors *A*, *B* and *C* were deemed more worth investigating.

The four bulk properties (responses) were then simulated in PFC^{3D} using this experimental design. The bulk properties that were obtained for each treatment combination are shown in Table A.9:

Table A.9 - Bulk Property Value for each Treatment Combination

	ρ_b (kg/m^3)	n (%)	E' (MPa)	ϕ (°)
0000	1 144.1	42.8	3.30	12.6
1001	11 527.0	42.4	5.69	10.5
0101	1 136.1	43.2	6.74	14.7
1100	11 668.0	41.7	3.87	17.4
0011	1 140.2	43.0	5.69	16.0
1010	11 532.5	42.3	3.81	12.7
0110	1 141.9	42.9	4.03	13.9
1111	11 529.0	42.4	6.53	14.6

The effects of the four micro properties on the four bulk properties were calculated along with the effects of their three second-order interactions. The effect estimations are summarised in Table A.10:

Table A.10 - Estimated Micro Property Effects

	Effect on			
Factor	ρ_b	n	E'	ϕ
A	10 423.55	-0.79	0.04	-0.50
B	32.80	-0.09	0.67	2.20
C	-32.90	0.14	0.11	0.49
AB	35.95	-0.25	-0.22	2.23
AC	-33.85	0.19	0.27	-0.79
BC	-33.70	0.06	-0.14	-2.31
D	-38.55	0.30	2.41	-0.19

In Table A.10 *A*, *B*, *C* and *D* denote particle density, inter-particle friction, particle-wall friction and particle stiffness respectively. *AB* denotes the second-order interaction between particle density and inter-particle friction, while *AC* denotes the second-order interaction between particle density and particle-wall friction. Furthermore *BC* represents the second-order interaction between inter-particle friction and particle-wall friction.

The effects as summarised in Table A.10 were presented graphically in the form of a scree plot and normal probability plot for each bulk property. The effects were also used to derive the multiple linear regression models for each bulk property. In the following section this is discussed more comprehensively. Again, it should be noted that the results are for the parameters in Tables A.6 and A.7, and that different results can be expected for other implementations of particle sizes and shape distributions.

A.4 Results: Particle Micro Property Effects

A.4.1 Bulk Density and Porosity

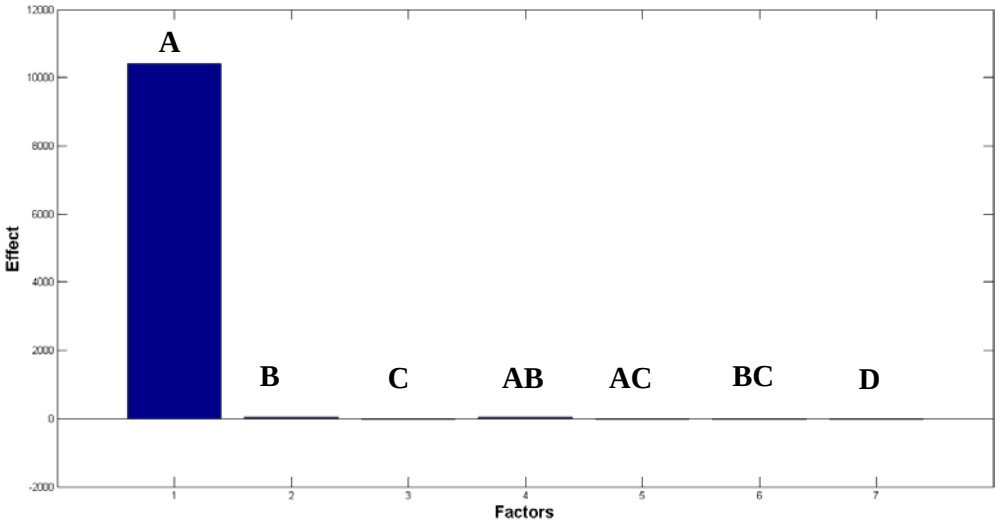

Figure A.1 – Scree Plot Showing the Effects of Factors and Interactions on Bulk Density

In Figure A.1 factor *A* (particle density) clearly has the largest effect on the bulk density of the simulated system. The remaining factors and their interactions appear to have a negligible effect on the bulk density. This finding is expected since, analytically, the bulk density depends directly on the bulk mass, which in turn depends directly on the specified particle density. If an increase in particle density is experienced, an increase in bulk density is expected which is also evident from Figure A.1. This behaviour is also seen in Figure A.2, where a normal probability plot was constructed for the data. According to Vining (1998) the so-called “fat pencil rule” is used in a normal probability plot to identify the factors that could have an important effect on the response under investigation. In Figure A.2 most of the data points lie in a line, which can be covered by the “fat pencil”, while one data point lies outside of the line, namely that of the particle density.

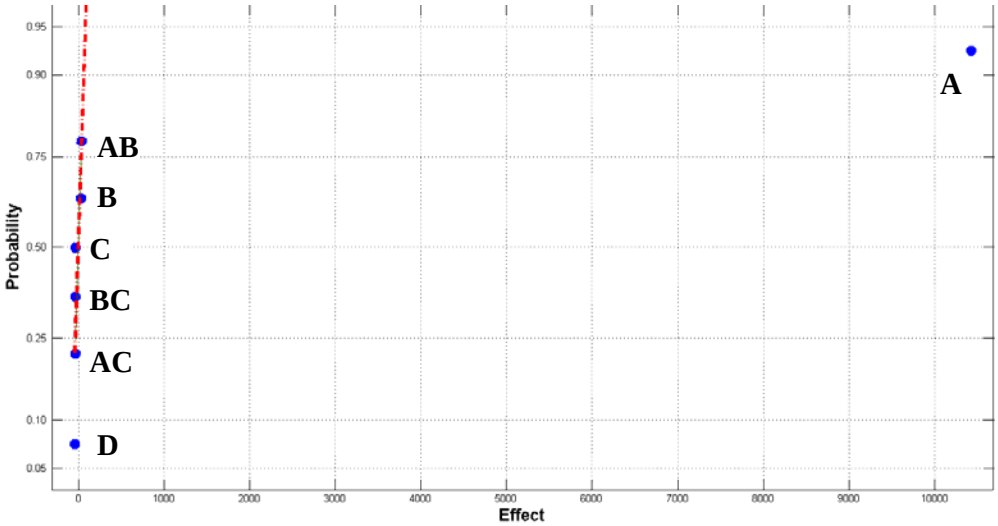

Figure A.2 – Normal Probability Plot of Factor Effects on Bulk Density

The bulk densities obtained in Table A.9 were used to derive a linear regression model in an attempt to present the empirical correlations more effectively. Multiple linear regression analysis was performed on the data to obtain a relation between the bulk density and the four micro properties (including their interactions) under investigation. This was done using the outline in Equation A.2. The regression coefficients were obtained using general linear regression theory and matrix calculations in Matlab as dictated by Vining (1998). The resulting regression equation is as follows:

$$\rho_b = 8.015 + 0.58\,\rho_p + 92.93\,\mu_{pp} + 1\,418.9\,\mu_{pw} + 0.009\,\rho_p\mu_{pp} - 0.108\,\rho_p\mu_{pw} - 4\,279.4\,\mu_{pp}\mu_{pw} - 38.55\,k_p \quad \text{(A.3)}$$

When the micro property values in Table A.8 are substituted into Equation A.3 and the results compared with the numerical results for the same micro property treatment combinations, it is seen that the regression model predicts the numerically bulk density very well (see Table A.11). The regression model is further tested later in this appendix by means of a centre run evaluation as well as with an additional treatment combination test.

Table A.11 - Multiple Linear Regression Model Prediction of Bulk Density

	ρ_b (kg/m^3)		% Variation
	PFC^{3D}	Regression	
0000	1 144.1	1 145.0	0.079
1001	11 527.0	11 535.0	0.069
0101	1 136.1	1 137.0	0.079
1100	11 668.0	11 677.0	0.077
0011	1 140.2	1 141.0	0.070
1010	11 532.5	11 540.0	0.065
0110	1 141.9	1 143.0	0.096
1111	11 529.0	11 538.0	0.078

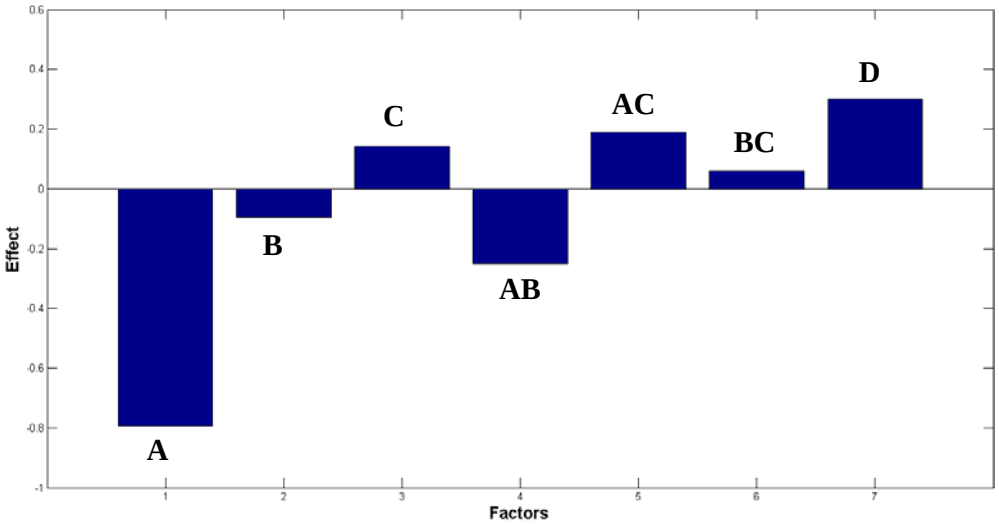

Figure A.3 – Scree Plot Showing the Effects of Factors and Interactions on Porosity

For the porosity (Figure A.3) the particle density (*A*) also has the largest effect while the particle stiffness (*D*) appears to have the second largest effect. Furthermore the interaction between the particle density and inter-particle friction (*AB*) also seem to have a significant effect on the porosity. Figure A.4 suggests from the normal probability plot that the most important factor that affects the porosity is the particle density (*A*).

Since porosity can also be analytically derived from the particle density it becomes clear that the particle density can have a significant effect on porosity. The higher the particle density the more compaction of the sample will take place under gravity, resulting in fewer voids between the particles and thus a lower porosity. The interaction between particle density and inter-particle friction (*AB*) also makes sense since it is expected that inter-particle friction can also have a direct influence on the compaction of a sample under gravity.

In general it is expected that the porosity will increase with an increase in friction (for both inter-particle and particle-wall) due to the reduced compaction brought

about by the restricted movement due to the higher friction. This was found for the particle-wall friction (*C*), but the opposite was found for the inter-particle friction (*B*). More research is needed to further investigate this phenomenon.

The effect of the particle stiffness (*D*) is not as trivial as it is generally not expected for particle stiffness to have a meaningful effect on the porosity. This phenomenon can be attributed to the overlapping characteristics of the linear contact model, where the particle stiffness can result in substantial particle overlaps that, in turn, can affect the porosity. It is still expected not to be as significant as the effect of inter-particle friction, or even particle-wall friction and a more detailed investigation is required.

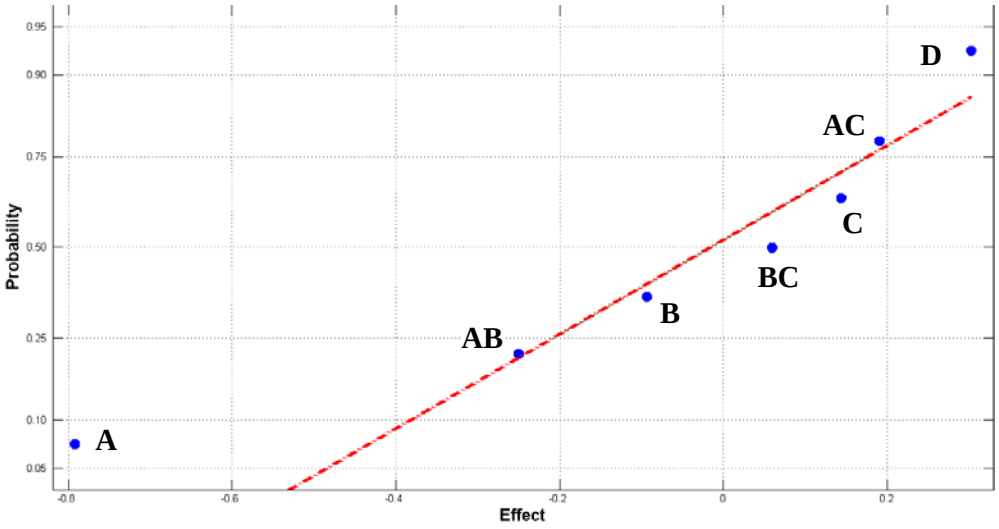

Figure A.4 – Normal Probability Plot of Factor Effects on Porosity

A multiple linear regression analysis was also performed on the data for the porosity and the resulting regression model is as follows:

$$\begin{aligned} n \; = {} & 42.604 - 0.000044\,\rho_p + 0.265\,\mu_{pp} - 4.616\,\mu_{pw} \\ & -0.000062\,\rho_p\mu_{pp} + 0.0006\,\rho_p\mu_{pw} + 7.521\,\mu_{pp}\mu_{pw} \\ & +0.302\,k_p \end{aligned} \tag{A.4}$$

Substituting the micro property values in Table A.8 into Equation A.4 and comparing the results with the numerical results, it is again seen that the regression model predicts the numerically porosity satisfactorily (Table A.12). A centre run evaluation as well as an additional treatment combination test will also be discussed for the porosity later in this appendix.

Table A.12 - Multiple Linear Regression Model Prediction of Porosity

	n (%)		% Variation
	PFC^{3D}	Regression	
0000	42.8	42.8	0.002
1001	42.4	42.4	0.002
0101	43.2	43.2	0.002
1100	41.7	41.7	0.005
0011	43.0	43.0	0.002
1010	42.3	42.3	0.002
0110	42.9	42.9	0.002
1111	42.4	42.4	0.005

A.4.2 Confined Young's Modulus

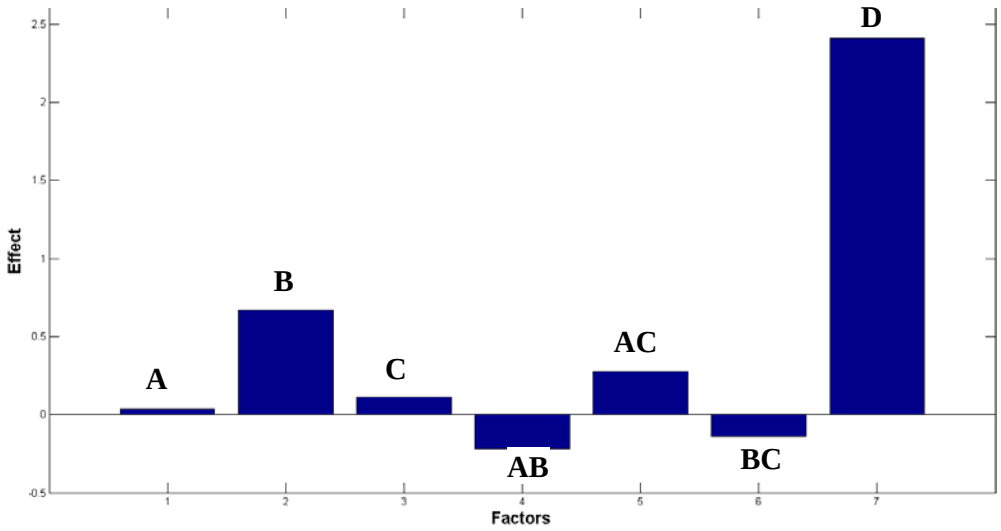

Figure A.5 – Scree Plot Showing the Effects of Factors and Interactions on Confined Young's Modulus

The confined Young's Modulus is affected mostly by the particle stiffness (*D*), while the inter-particle friction (*B*) has the second largest effect. The remaining factors and their interactions appear not to have any significant effects on the simulated confined Young's Modulus as can be shown in Figures A.5 and A.6.

The large effect of the particle stiffness (*D*) on the confined Young's Modulus is expected since the bulk (macro) stiffness of a bulk material packing depends largely on the micro stiffness. An increase in the particle stiffness will result in an increase in the bulk stiffness as well as the confined Young's Modulus. The inter-particle friction (*B*) is also expected to have some effect on the strain that the sample experiences during uniaxial compression, which is ultimately used to determine the confined Young's Modulus. Since the packing's ability to compact decreases with an increase in inter-particle friction, an increase in confined Young's Modulus will be experienced with an increase in inter-particle friction.

It is also expected that the particle-wall friction would have a more significant effect than was found in Figures A.5 and A.6, as it could also tend to restrict the bulk strain experienced by the sample. This could be attributed to the relatively small particle-wall friction values used. It can also be due to the total number of particle-wall contacts being far less than the particle-particle contacts in the packing. More research is thus needed to investigate this finding.

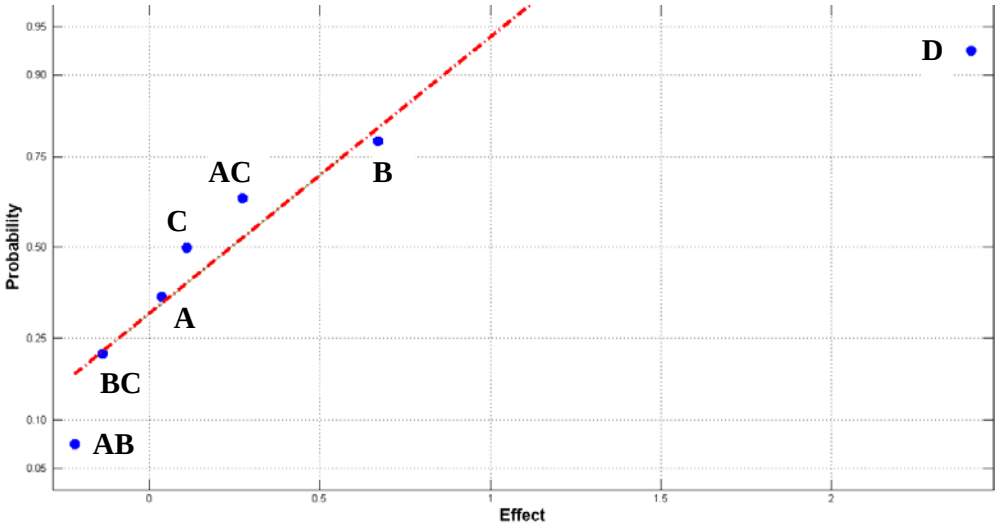

Figure A.6 – Normal Probability Plot of Factor Effects on Confined Young's Modulus

The multiple linear regression model as derived for the confined Young's Modulus is as follows (Equation A.5):

$$E' = 0.792 - 0.0000071\,\rho_p + 2.562\,\mu_{pp} - 1.588\,\mu_{pw} - 0.000054\,\rho_p\mu_{pp} + 0.00087\,\rho_p\mu_{pw} - 17.43\,\mu_{pp}\mu_{pw} + 2.409\,k_p \quad \text{(A.5)}$$

Testing Equation A.5 using the values in Table A.8 and comparing them with the numerical results show that, for the confined Young's Modulus, the regression model performs adequately in predicting the said bulk property (Table A.13).

Table A.13 - Multiple Linear Regression Model Prediction of Confined Young's Modulus

	E' (MPa)		% Variation
	PFC^{3D}	Regression	
0000	3.30	3.30	0.003
1001	5.69	5.69	0.002
0101	6.74	6.74	0.001
1100	3.87	3.87	0.013
0011	5.69	5.69	0.005
1010	3.81	3.80	0.011
0110	4.03	4.03	0.007
1111	6.53	6.53	0.005

A.4.3 Internal Friction Angle

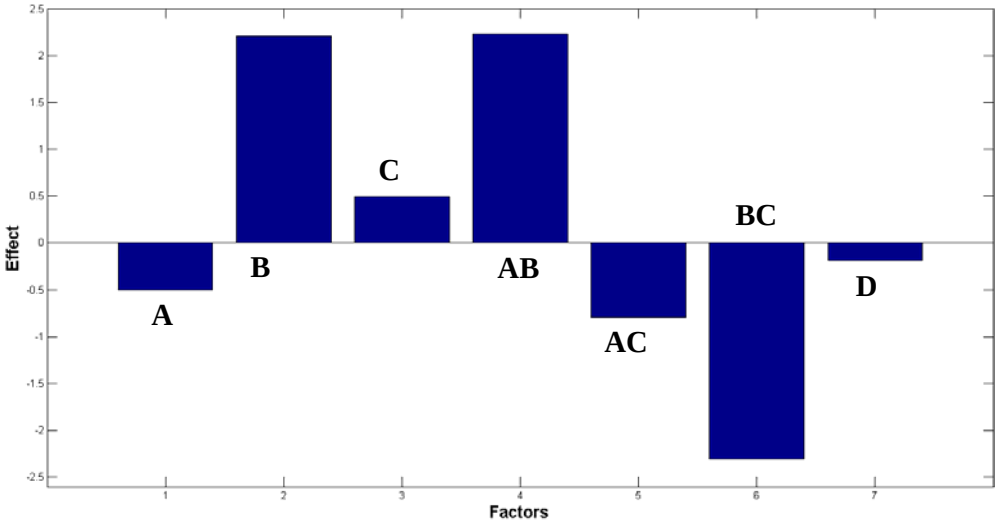

Figure A.7 – Scree Plot Showing the Effects of Factors and Interactions on Internal Friction Angle

In Figures A.7 and A.8 it is seen that the simulated internal friction angle depends mostly on the inter-particle friction (*B*), the interaction between particle density and inter-particle friction (*AB*) as well as the interaction between inter-particle friction and particle-wall friction (*BC*). The dependence on the inter-particle friction is evident from the fact that the internal friction angle is used to characterise the bulk frictional behaviour of a bulk material sample. Thus the inter-particle friction will have a significant effect on the internal friction angle, where an increase in the inter-particle friction results in an increase in the internal friction angle.

The effects of the interactions also make engineering sense since both of the significant interactions entail the interaction between inter-particle friction and another micro property (particle density for *AB* and particle-wall friction for *BC*). When the particle density and particle-wall friction are considered on their own, their effects do not seem to be of any importance. However, when they are considered along with the inter-particle friction, their effects become more important. This serves as an additional indication that the inter-particle friction has the most significant effect on the internal friction angle, as expected.

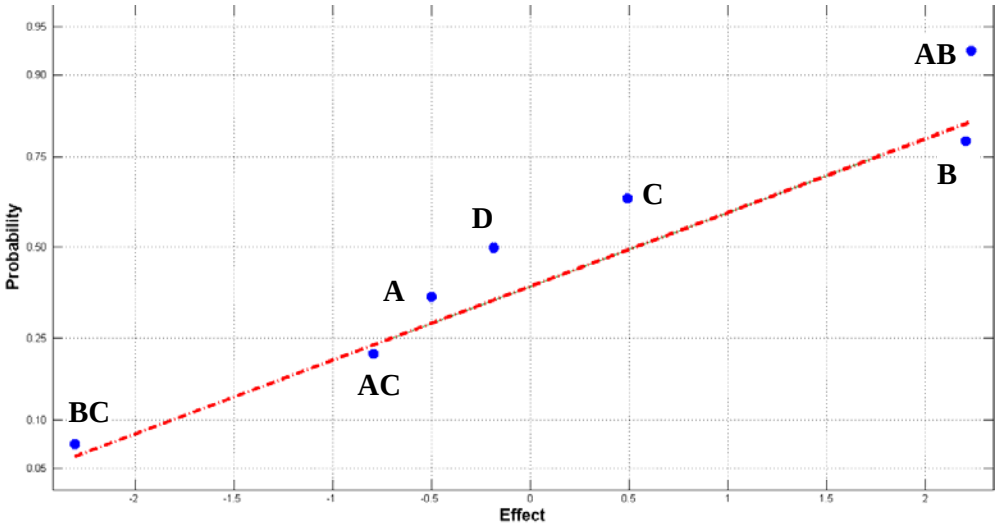

Figure A.8 – Normal Probability Plot of Factor Effects on Internal Friction Angle

Again a multiple linear regression analysis was performed with the data and he following model was obtained:

$$\phi = 11.595 - 0.00011\,\rho_p + 6.885\,\mu_{pp} + 122.279\,\mu_{pw} + 0.0005\,\rho_p\mu_{pp} - 0.0025\,\rho_p\mu_{pw} - 292.644\,\mu_{pp}\mu_{pw} - 0.186\,k_p \quad \text{(A.6)}$$

From testing the regression model, like for the previous bulk properties, it can again be seen that the regression model performs very well predicting the numerically obtained internal friction angles (Table A.14). The performance of this model, along with the other models presented in this Section, will be evaluated further in Section A.7.

Table A.14 - Multiple Linear Regression Model Prediction of Internal Friction Angle

	ϕ (°)		% Variation
	PFC^{3D}	Regression	
0000	12.6	12.6	0.002
1001	10.5	10.5	0.033
0101	14.7	14.7	0.002
1100	17.4	17.4	0.020
0011	16.0	16.0	0.010
1010	12.7	12.7	0.128
0110	13.9	13.9	0.012
1111	14.6	14.6	0.110

It should be noted that, for Equations A.3 to A.6, the random error estimations are present in the form of terms associated with the factors (or interactions) that are the least significant. The hidden replication phenomenon of factorial designs was used as the motivation for this approach (Vining, 1998).

A.5 Results: Particle Shape and Size Effects

To investigate the effect of particle size and shape on the four bulk properties, the same simulations were performed as for the design of experiments investigation. The general simulation parameters that were used are the same as in Table A.7, with the particle size and shape characteristics changed to account for this particular investigation.

A.5.1 Particle Shape Effects

Three particle shape scenarios were considered, namely a spherical shape and two elongated shapes that consist of two spherical particles clumped together (with no overlap C = 1.0 and 50% overlap C = 0.5) to form a so-called double clump. The particle shapes can be observed in Figure A.9. For comparison purposes, the overlap factor (C) for the spherical particles was defined as zero.

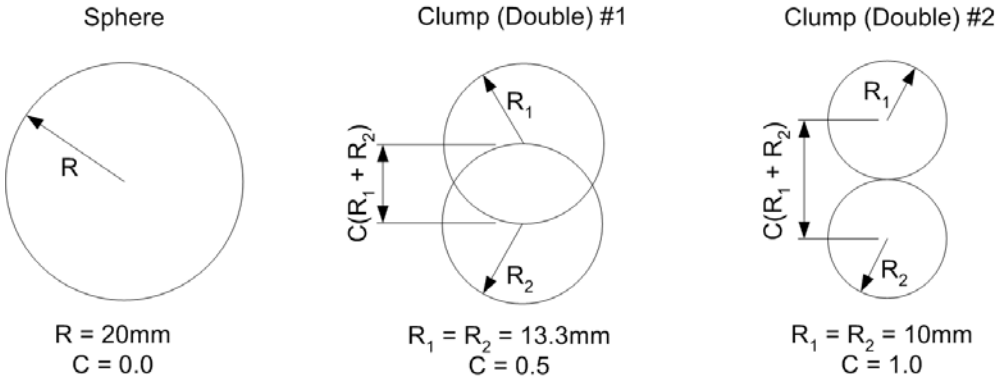

Figure A.9 – Schematic of Different Particle Shapes

The particle shape parameters are summarised in Table A.15, while the micro properties are in Table A.16. The remaining simulation parameters are as in Table A.7. For each particle shape scenario a packing consisting solely of that scenario's shape parameters (Table A.15) was used. One particle size per scenario was implemented, that is no size distribution was used.

Table A.15 - Particle Shape Parameters for the Three Scenarios

Shape	*C*	Radius (mm)	# of Spheres	# of Clumps
Spherical	0.0	20.0	839	839
Clump	0.5	13.3	3 740	1 870
Clump	1.0	10.0	6 820	3 410

Table A.16 - Micro Properties used in Particle Shape Effects Investigation

ρ_p (kg/m^3)	20 000
μ_{pp}	0.1
μ_{pw}	0.01
k_p (MN/m)	1.0

The particle radii were chosen as to give an overall particle size that is largely similar to that of the spherical particles. This was done to ensure a consistent particle size throughout the three cases, so that emphasis could be on the effect of particle shape alone.

The four bulk properties were simulated for the three particle shapes and the results are summarised in Table A.17.

Table A.17 - Bulk Property Values for Each Particle Shape

Shape	C	ρ_b (kg/m^3)	n (%)	E' (MPa)	ϕ (°)
Spherical	0.0	11 483.5	42.6	3.80	8.6
Clump	0.5	12 840.0	35.8	7.13	12.7
Clump	1.0	11 845.0	40.8	7.04	9.3

Due to the discrete nature of the particle shape variable, no regression analysis was performed for this investigation.

Bulk Density and Porosity

It was found that the bulk density increased when the shape was changed from spherical to a double clump with no overlap (C = 1.0). This increase was however not significant. This is due to the two shapes still resulting in packings with largely the same number of voids and gaps between the particles (albeit slightly fewer for the double clumps with no overlap). This appearance can also be seen when looking at the porosity values. The porosity decreases with a change from spherical to non spherical particles. The bulk density generally exhibits an increase with a change from spherical to non spherical particles. A higher compaction, and ultimately a denser packing, for non spherical particles is the reason for the abovementioned phenomena.

When the particle overlap is changed from no overlap to 50% overlap (C = 0.5), a substantial increase in the bulk density is achieved. This is also accompanied by a fairly large decrease in porosity. Since an increase in bulk density implies a more compacted system with a lower porosity, it can also be concluded that when a particle shape is altered (by means of increasing overlap), a smoother particle is created which will settle in a more compacted fashion due to the reduced interlocking effects. This can clearly be seen in the results for the change from no overlap to 50% overlap.

Confined Young's Modulus

A significant increase in the confined Young's Modulus is obtained when the particle shape is changed from spherical to double clump form (for both overlaps). There is a slight decrease in the values when the overlap changes from 50% to no overlap. It is, however, very small compared to the initial increase in values (from spherical to non spherical). This small decrease is not quite expected since the interlocking effects of the clumps with no overlap are expected to be more prominent than that for the clumps with 50% overlap. The interlocking effect contributes to the confined Young's Modulus. Higher interlocking reduces the inter-particle slip, or movement, which ultimately reduces the bulk strain of the sample; hence an increase in the confined Young's Modulus is expected. Therefore, the large increase in values from the spherical shape to double clump shape is understandable, since spherical particles essentially exhibit no interlocking effects. As for the small change in values when the double clump shape is changed from 50% overlap to no overlap, further investigation is required.

Internal Friction Angle

When the particle shape was changed from the spherical shape to the non spherical shape with no overlap, a slight increase in the internal friction angle was observed. This increase was not very significant, which is not expected since the interlocking effects of the non spherical particles should contribute to a large increase in the internal friction angle.

A further increase in the internal friction angle can be seen when the non spherical particles were changed from no overlap to 50% overlap. This was also not expected since the 50% overlap particles would exhibit less interlocking than those with no overlap, and thus a lower internal friction angle.

The results obtained for the particle shape effects on the internal friction angle did not correlate with the expected behaviour of the system. Further research is necessary to investigate this. Despite the results' apparent deviation from the expected system behaviour, the generally expected increase in internal friction angle with a change in particle shape, from spherical to non spherical, was still observed.

A.5.2 Particle Size Effects

For this investigation the variable was the particle size. Three scenarios were considered, each with spherical particles. The three different particle radii were implemented as in Table A.18. The remaining micro properties and simulation parameters can be observed in Tables A.16 and A.7. Only one particle size (with no size distribution) was implemented for each size scenario, as in Table A.18.

Table A.18 - Particle Size Parameters for the Three Scenarios

Shape	Radius (mm)	# of Particles
Spherical	15.0	2 029
Spherical	17.5	1 267
Spherical	20.0	844

The bulk properties obtained for this investigation are as follows (Table A.19):

Table A.19 - Bulk Property Values for each Particle Size

Shape	Radius (mm)	ρ_b (kg/m^3)	n (%)	E' (MPa)	ϕ (°)
Spherical	15.0	11 909.0	40.5	4.70	6.0
Spherical	17.5	11 690.5	41.5	3.55	11.4
Spherical	20.0	11 579.5	42.1	3.50	12.6

As expected, the bulk density increases with a decrease in particle size. This is due to the higher compaction achieved with the larger number of particles within the same bulk volume. The same conclusion can be made when looking at the porosity: the porosity decreases as the particle radius decreases, due to the increased compaction of the particles (and the denser nature of the packing).

The higher compaction of the packing due to the smaller particles that fill the same bulk volume also causes an increase in the confined Young's Modulus. This is also expected since a packing that is compacted will be less likely to experience additional inter-particle slip (movement) during compression than one that is less compacted. The bulk strain experienced will be smaller; hence the larger confined Young's Modulus.

With an increase in particle size the internal friction angle was also found to increase. This is due to the reduced number of particles in the same bulk volume that result in a "coarser" packing on a macro scale, which will directly contribute to the increasing of the internal friction angle. With more particles in the packing occupying the same bulk volume (as in the case for the smaller particles), more inter-particle contacts are present that enable "smoother" bulk behaviour in terms of particle flow and displacement. More inter-particle contacts (per bulk volume) result in inter-particle slip, or motion, to occur more readily, hence the "smoother" behaviour. The change in internal friction angle with a change in particle size (for the same particle shape and friction coefficient) could thus be attributed to this change in the total number of inter-particle contacts (per bulk volume).

The results from the particle size effect simulations were used to obtain basic linear regression models. These models can ultimately be used in predicting the bulk response of a system due to particle size variations. The continuity of the variable in this case enabled for a simple linear regression analysis to be performed. The linear regression models can be seen from Equations A.7 to A.10 and their bulk property predictions can be observed in Table A.20. The percentage

variations of the regression results from the corresponding DEM results in Table A.19 are also in Table A.20.

$$\rho_b = 12\,880 - 65\,900\,R \tag{A.7}$$

$$n = 35.6 + 329.7\,R \tag{A.8}$$

$$E' = 8.0926 - 238.8\,R \tag{A.9}$$

$$\phi = -12.9282 + 1\,310.3\,R \tag{A.10}$$

In the abovementioned equations R is the particle (sphere) radius in metres.

Table A.20 - Basic Linear Regression Predictions of Bulk Parameters (Particle Size)

Radius (mm)	ρ_b (kg/m^3)		n (%)		E' (MPa)		ϕ (°)	
	(A.7)	%	(A.8)	%	(A.9)	%	(A.10)	%
15.0	11 891.0	0.15	40.5	0.22	4.51	3.93	6.7	12.04
17.5	11 727.0	0.31	41.4	0.43	3.91	10.40	10.0	12.64
20.0	11 562.0	0.15	42.2	0.21	3.32	5.27	13.3	5.76

The predicted results in Table A.20 correspond well with the DEM results of Table A.19, when considering that linear assumptions were initially made for the bulk behaviours in this case. The regression models can thus be used to good effect in predicting the bulk properties as investigated in this study.

As for the particle shape investigation, more work can be done to investigate the repeatability and general reliability of the results by means of implementing particle size distributions. With a particle size distribution implemented along with a constant particle shape, more repeatable results are expected for the confined Young's Modulus, as well as the internal friction angle due to an increase in the total number of inter-particle contacts that enable more frequent inter-particle slip.

A.6 Results: Container Size and Shear Velocity Effects

The effect of the container size on the simulated bulk density, porosity, confined Young's Modulus and internal friction angle was investigated. The effect of the shear velocity on the general direct shear test simulation results was also briefly investigated.

A.6.1 Container Size Effects

The simulation parameters that were implemented for the container size investigation are as follows (Table A.21). Note that the DST simulation was only conducted at one normal load, as opposed to four, for each container size. This

was done to compare the typical shear stress-shear strain curves (no direct comparison between the internal friction angles were done).

Table A.21 - Simulation Parameters for Container Size Effect Investigation

	Small Container	Large Container
Wall Stiffness (MN/m)	10	10
Particle Shape	Spherical	Spherical
Particle Radius (mm)	20	20
Number of Particles	834	1715
Container Radius (mm)	200	295
Packing Depth (mm)	370	345
Lid Velocity (CCT) (mm/s)	1	1
Maximum Normal Force on Lid (N)	8 415	18 300
Shear Velocity (DST) (mm/s)	0.3	0.3
Total Shear Displacement (mm)	39	59
DST Normal Initial Compression (N)	8 415	18 300
DST Normal Load (N)	6 760	14 700

The differences in normal load values are to establish similar normal stresses on the samples for the different container sizes. The micro properties that were implemented for the spherical particles in both cases are as follows (Table A.22):

Table A.22 - Micro Properties for Container Size Investigation

ρ_p (kg/m^3)	11 000
μ_{pp}	0.275
μ_{pw}	0.0275
k_p (MN/m)	1.5

The resulting bulk densities, porosities and confined Young's Moduli obtained are as follows (Table A.23):

Table A.23 - Bulk Properties obtained for Different Container Sizes

	Small Container	Large Container	% Variation
ρ_p (kg/m^3)	6 306.8	6 328.8	0.35
n (%)	42.7	42.5	0.47
E' (MPa)	4.31	4.16	3.51

In Table A.23 it is clear that the size of the container has a negligible effect on the porosity and bulk density of the packing (for a specified particle size and shape) since the percentage variation from the smaller container's results is less than 1% for both of the said bulk properties. Considering the confined Young's Modulus a larger difference between the container size scenarios were obtained. This is however, still close enough to conclude that the confined Young's Modulus is also not drastically affected by the container size.

For the direct shear test simulations it is also observed that the results for the different container sizes appear largely similar (see Figure A.10). It can therefore be concluded that the effect of container size appears to be insignificant in terms of the internal friction angle as well. The stress dependency of the internal friction angle could indicate a more prominent effect of container size on the internal friction angle. However, due to time constraints the extra direct shear test simulations at the other normal loads, required to investigate this, were not conducted.

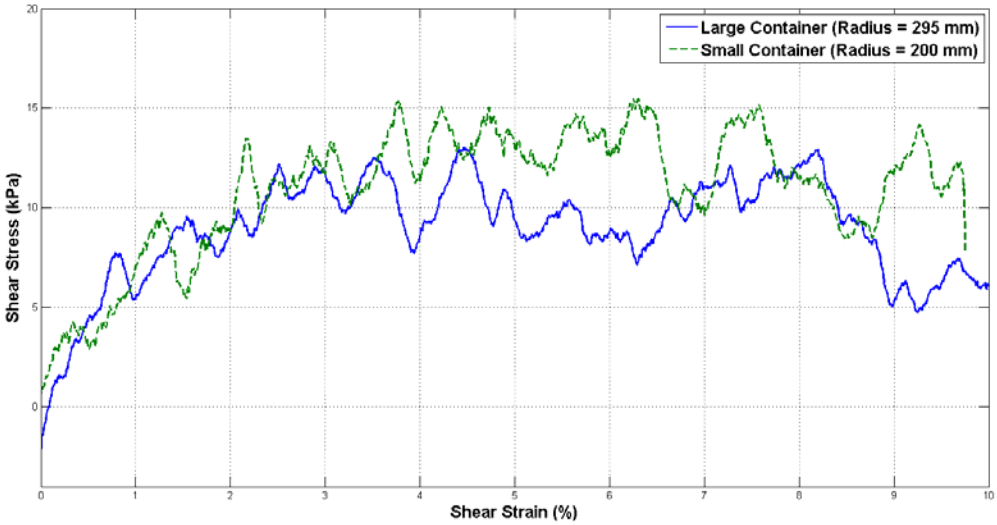

Figure A.10 – Shear Stress versus Shear Strain Curves for Different Container Sizes (Direct Shear Test)

A.6.2 Shear Velocity Effects

The same simulation parameters were used for the shear velocity investigation as in Table A.21 (Small Container). The parameter that was varied in this case was the shear velocity (from 0.3 mm/s to 1 mm/s). The micro properties as in Table A.22 were also used. The direct shear test results for the two shear velocity applications can be seen in Figure A.11. Again, note that only one normal load case was simulated for both velocities, as only a visual comparison of the curves were done.

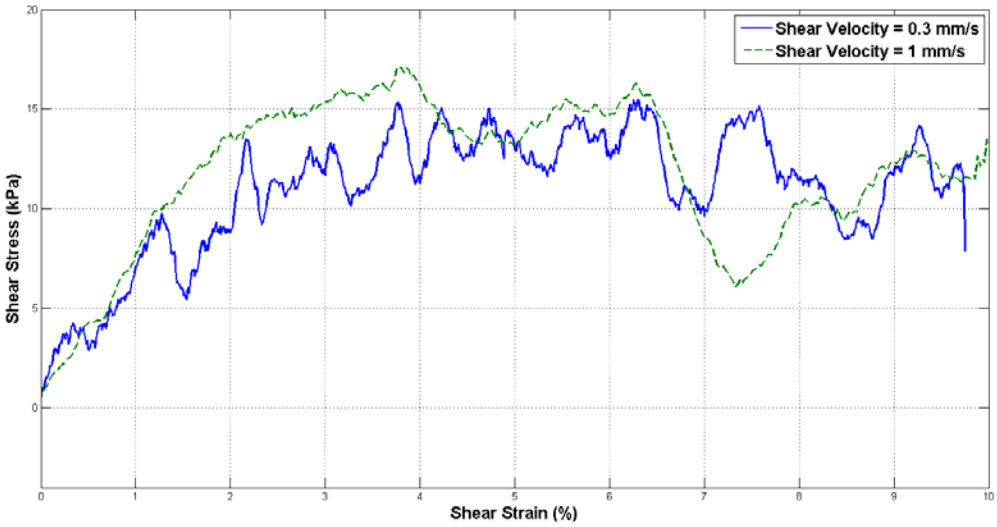

Figure A.11 – Shear Stress/ Shear Strain Curves for Different Shear Velocities (Direct Shear Test)

Again, for the different shear velocities implemented, it was found that the results appear to be similar to the extent that similar internal friction angles will also be derived. More research is still needed to investigate the shear velocity effect in more detail (on the simulated internal friction angle).

In general it is concluded that, for the simulation and material parameters considered, the effect of the container size on the mentioned bulk properties is not of any significance. The same can be concluded for the effect of shear velocity on the typical direct shear test results. The container size and shear velocity effects on repeatability could be more important; however, due to time constraints this was not investigated and future work is also needed in this regard.

A.7 Results: Centre Run and Extra Treatment Combination

The multiple linear regression models developed for the four bulk properties and presented in Section A.4 all predicted the numerical bulk properties for the specified micro property combinations to within less than 1% variation from the DEM results (see Tables A.11 to A.14). This good fit was, however, predictable since the DEM bulk properties for the eight treatment combinations were used in the regression analysis to construct the models. The general ability of the models to predict the bulk behaviour therefore needed to be further investigated. This was done by means of a centre run investigation, in which micro properties values were used that lie exactly halfway within the range of the micro properties for the design of experiments investigation. The bulk properties were then simulated again in PFC^{3D} with these properties and also predicted with the regression models (by substituting the new micro properties into the models). The correlations between the two sets of results were then used to evaluate the reliability and performance of the regression models.

Additionally, a second combination of micro property values was also used to evaluate the regression models. This time arbitrary micro property values were used that still lie within the range of values used for the large design of experiments investigation in Section A.4. The DEM results and regression model predictions were then also compared. The general simulation parameters in Table A.7 were used for both the centre run and extra treatment combination investigations.

A.7.1 Centre Run Evaluation

The micro properties for the centre run investigation lie halfway through the range of the micro properties in Table A.6 and are the same as in Table A.22. The values in Table A.22 were implemented in PFC^{3D} and also used in the regression models (Equations A.3 to A.6). The results are summarised in Table A.24.

Table A.24 - Centre Run: DEM and Regression Model Predictions

	PFC^{3D}	Regression	% Variation
ρ_b (kg/m^3)	6 327.9	6 357.0	0.46
n (%)	42.5	42.6	0.24
E' (MPa)	4.89	4.96	1.29
ϕ (°)	12.2	14.1	15.40

For the bulk density and porosity a very good correlation (of less than 1% variation from the DEM results) between the DEM results and regression model prediction is observed. The confined Young's Modulus also shows a good correlation (slightly higher than 1%). However, the internal friction angle shows a fairly large discrepancy between the DEM and regression model results (approximately 15%).

A.7.2 Extra Treatment Combination Evaluation

The arbitrary micro property values used for the extra treatment combination are within the range of Table A.6 and are as follows (Table A.25):

Table A.25 - Micro Properties for Extra Treatment Combination

ρ_p (kg/m^3)	16 000
μ_{pp}	0.15
μ_{pw}	0.035
k_p (MN/m)	1.2

As in the centre run evaluation, the properties in Table A.25 were implemented in PFC^{3D} and the regression models and the following results were obtained (Table A.26):

Table A.26 - Extra Treatment Combination: DEM and Regression Model Predictions

	PFC^{3D}	Regression	% Variation
ρ_b (kg/m^3)	9 222.2	9 244.0	0.24
n (%)	42.4	42.4	0.04
E' (MPa)	4.43	4.16	6.03
ϕ (°)	11.9	13.3	11.50

Again, it was found that the regression models for the bulk density and porosity predict the said bulk properties very well (also to within 1% variation from the DEM results). For the confined Young's Modulus a larger discrepancy was observed (approximately 6%). For the internal friction angle a relatively large discrepancy was also found (12%).

The good correlations for the bulk density and porosity serve as a reliable indication that the regression models are adequate for predicting these bulk properties within the ranges for which the models were developed. The correlations for the confined Young's Modulus and internal friction angle are not as close, but could still be regarded as adequate, depending on the assumptions and limitations that are relevant.

The larger discrepancies observed for the confined Young's Modulus and internal friction angle can be attributed to the behaviour of the bulk properties not being linear within the property range and system parameters of the investigation. The largely non-linear and occasional stochastic nature of the DEM can also account for this assumption. Should this be the case these linear regression models will not be able to predict the bulk properties with high accuracy. The results in Section A.4 from which the regression models for the confined Young's Modulus and internal friction angle were developed could also exhibit random error that was not properly accounted for, considering that the concept of hidden replication was used to consider possible random error.

Furthermore it is possible that there could be underlying simulation parameters that might have had an influence on the reliability as well as the repeatability of the DEM results, the subsequent regression analysis and thus the larger discrepancies for the confined Young's Modulus and internal friction angle. Factors such as the number of particles, particle and container size and particle shape could have resulted in parameters such as the ratio of particle size to container size not to be optimal. In general, more reliable and repeatable results are expected when smaller particles (and thus more particles) are used for the DEM simulations, but due to time constraints this option could not be fully implemented.

However, taking the limitations and assumptions of the DEM simulations into account, the reliability and repeatability of the results can still be regarded as adequate for this investigation. Thus the effects and regression models (from Section A.4) are also expected to be reliable, given the assumptions.

It can thus be concluded that all of the regression models are adequate for predicting the bulk properties within the chosen property ranges. When larger discrepancies are observed between the predicted and simulated results, it can be attributed to the need for more complex, higher order regression models. Further research could be done to investigate the repeatability and reliability of the DEM results by implementing smaller particles and particle size distributions. The next logical step would be for advanced analysis of variance (ANOVA) techniques to be performed on the regression models to further quantify the current models' validity and to form the basis for more complex models.

A.8 Conclusions

In this chapter a design of experiments analysis was done, in the form of a half fraction of the 2^4 design, to identify the most prominent micro property effects on the simulated bulk properties that were used in this project's general bulk material calibration procedure. It was found that the important micro properties identified for each bulk parameter were mostly as expected. Other, less trivial micro properties effects were justified using engineering judgement. The general findings are that the bulk density and porosity are both greatly affected by the particle density. The confined Young's Modulus is influenced mostly by the particle stiffness while the internal friction angle's most prominent micro property is the inter-particle friction. This is in conjunction with the expected behaviour.

For each bulk property a multiple linear regression model was generated from the data. Linear regression was used since it was assumed that, for an initial investigation, the behaviour of the bulk properties would be largely linear. The terms in the models associated with the least significant factors and interactions were regarded as random error terms, in an attempt to account for error in the processes. The regression models were then tested by means of a centre run investigation as well as an extra arbitrary treatment combination. It was found that the models predicted the bulk responses with acceptable accuracy. Other discrepancies between the model predictions and the DEM simulations were concluded to be due to possible non-linear, or higher-order, bulk property behaviour and thus the need for more complex regression models is envisaged. However, considering the limitations and assumptions made for this study, the regression models predicted the system behaviours considerably well.

A brief investigation into the effects of the particle size and shape on the said bulk properties was also done. It was found that the particle shape affected all of the bulk properties, especially when the shape was changed from spherical to non-spherical. The varying degree of interlocking between the particles associated with these changes allowed for differences in compaction as well as recorded bulk strain, which in turn affected the bulk properties. The particle size also tended to affect the bulk properties, but to a lower degree than the particle shape.

An independent investigation was also done to determine whether the container size would have an effect on the bulk properties and, for the material and system parameters used, no significant effects were observed. The shear velocity, in the case for the direct shear test simulations, also appeared not to have any substantial influence on the bulk results.

In general it can be concluded that the micro properties considered do affect the bulk properties in the fashion expected. Using these quantified effects a more efficient calibration procedure can be planned. Since this was an initial investigation, more research can be done in the development of more complex, higher-order regression models to be used as objective functions for formal optimisation. More work can also be done to improve the reliability and repeatability of the simulated results to improve the general credibility thereof. Ultimately these improved results and prediction models can be used, along with an appropriate design of experiments methodology, to form part of a more formal bulk material calibration procedure that incorporates DEM parameter optimisation in addition with the design of experiments screening procedure.

Appendix B: Rolling Friction Estimation

The rolling friction coefficient, μ_{rf}, of the castor wheels of the large scale shear box was estimated using a preliminary test that entailed the execution of a DST, but with no bulk material in the container and no lid on top. The test was performed four times, each time with a different weight placed in the bottom half of the container, as shown in Table B.1.

Table B.1 - Weights used in Rolling Friction Test

Scenario	Total Mass (kg)
1	110
2	200
3	260
4	300

The normal load on the tracks, F_n^{μ}, is determined as follows, with m_1 being the mass of the weight in the container and m_2 the mass of the bottom half of the container (88 kg):

$$F_n^{\mu} = (m_1 + m_2)g \tag{B.1}$$

Using general mechanics, μ_{rf} can be determined as follows (where F_s^{μ} is the recorded friction force):

$$\mu_{rf} = \frac{F_s^{\mu}}{F_n^{\mu}} \tag{B.2}$$

The typical friction forces measured for the scenarios can be seen in Figure B.1.

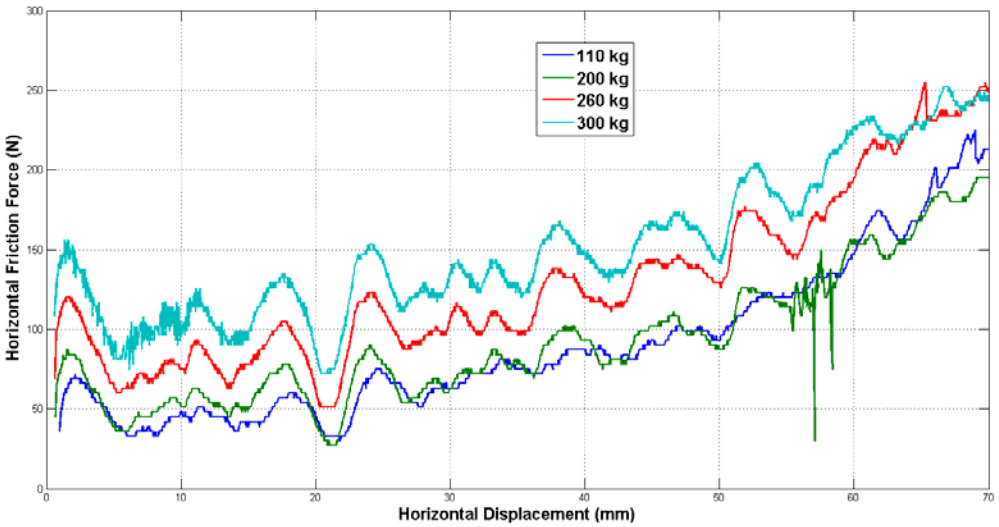

Figure B.1 - Rolling Friction Force on the Castor Wheels

The friction force notably increases with horizontal displacement. The reason for this is not known, but it might be due to manufacturing tolerances and the layout of the tracks. However, these friction loads and corresponding normal loads were still used to calculate the rolling friction coefficient, as in Equation B.2, which can also be seen in Figure B.2.

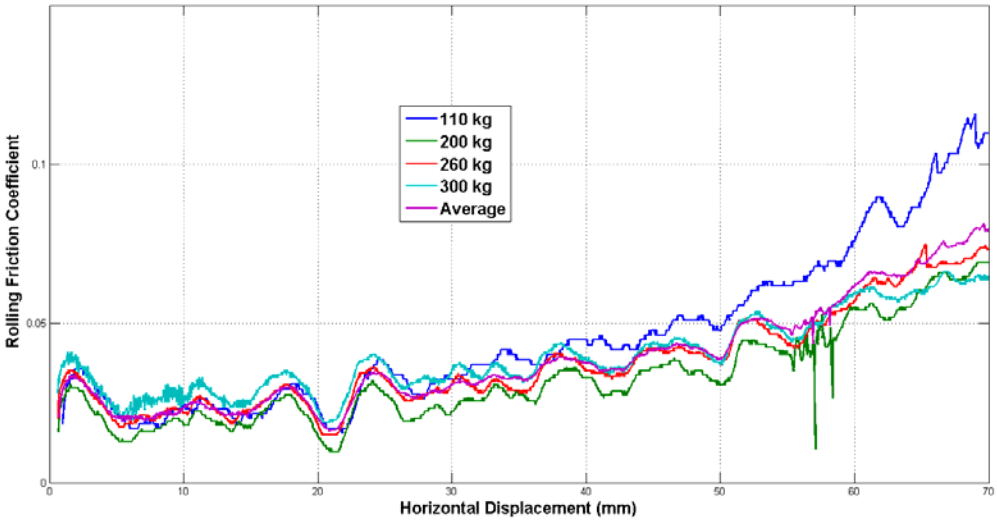

Figure B.2 - Rolling Friction Coefficient over Horizontal Displacement

The rolling friction coefficient is mostly load independent but still displacement dependent. The average rolling friction coefficient (as a function of displacement) was then used in all direct shear tests to calculate the friction force given by Equation 3.5.

Appendix C: Additional DST Evaluations

The experimental DST procedures in this project were conducted at a constant shear velocity of 1 mm/s, over a shear distance of 70 mm. The starting position of the bottom half is such that it is lined up with the top half (Figure C.1).

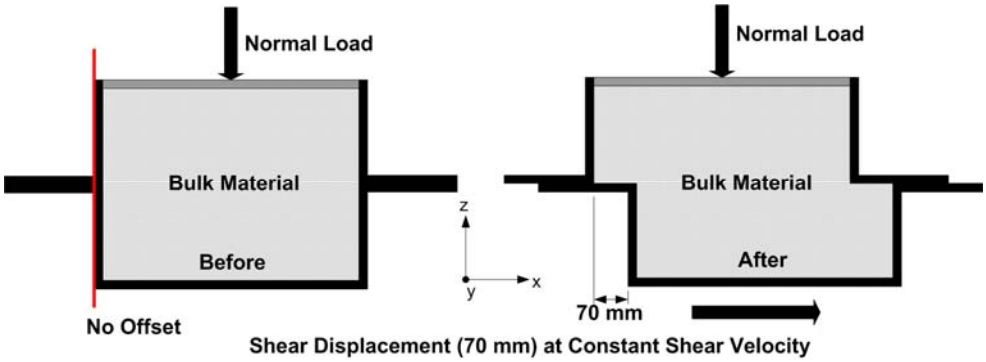

Figure C.1 - Direct Shear Test Before and After Test Run (No Offset)

In some cases the starting position can be at an offset, as in Figure C.2. The total shear distance will then typically be twice the offset. To investigate the effect of an offset on the results, a preliminary DST was run at an offset of 70 mm (and thus a total shear distance of 140 mm) and the results compared to that of a DST with no offset. Both of the tests were done at the same shear velocity (1 mm/s).

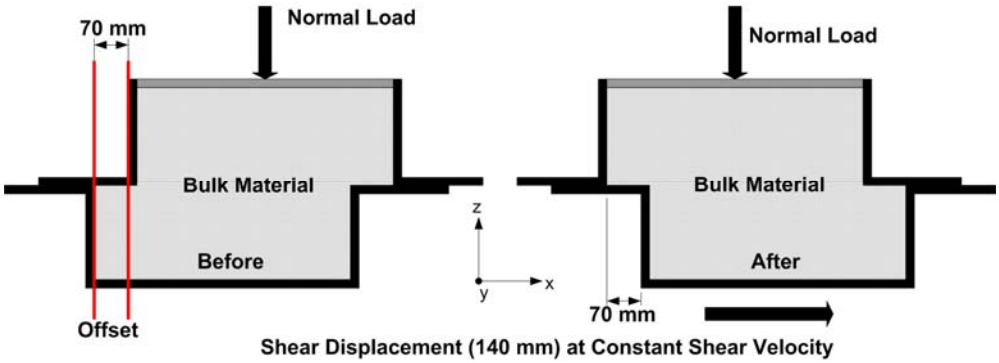

Figure C.2 - Direct Shear Test Before and After Test Run (70 mm Offset)

An additional test was also done in which the shear velocity was increased to 3 mm/s (at no offset). This test was done to evaluate the effect of shear velocity on the DST results. The normal load cases for these investigations were the same as for the general DST experiments (see Table 3.1). The bulk shear stress curves for the three cases can be seen in Figure C.3. For the case of no offset, the residual normal and shear stresses were obtained by considering the average stresses between 8% and 10% shear strain. For the 70 mm offset the averages were taken between 15% and 17% shear strain.

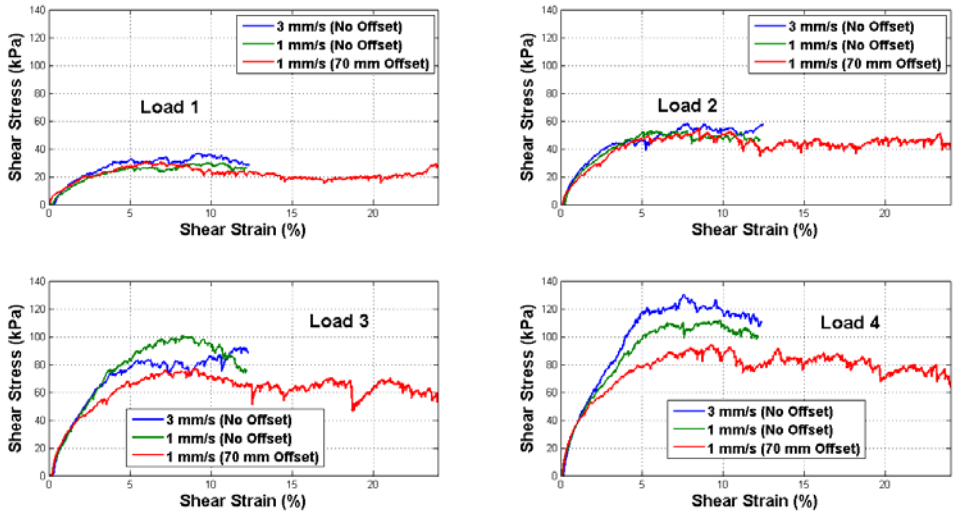

Figure C.3 - Bulk Shear Stress Curves for Additional Direct Shear Tests

In Figure C.4 the internal friction angle with no offset is compared to that with the 70 mm offset.

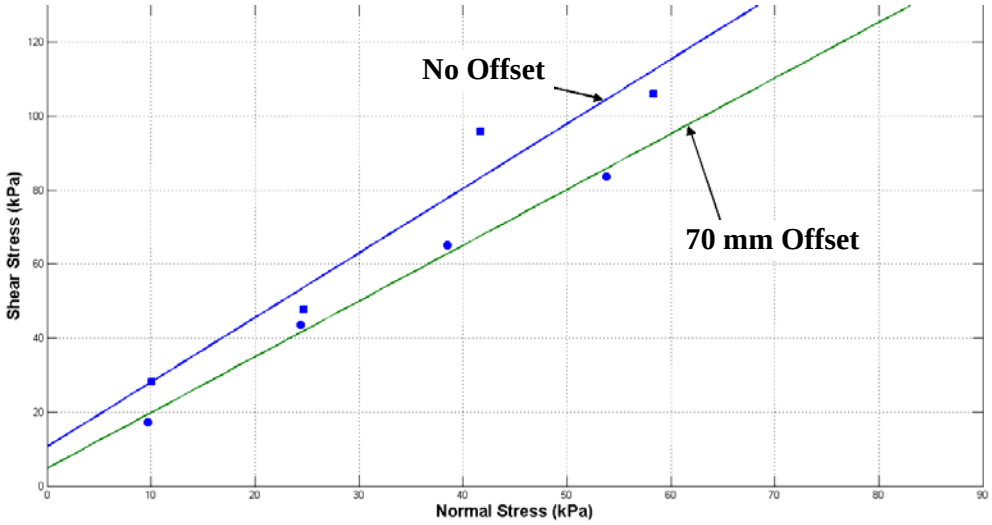

Figure C.4 - Internal Friction Angles (No Offset versus 70 mm Offset)

In Figure C.5 the comparison is shown between the internal friction angles at different shear velocities.

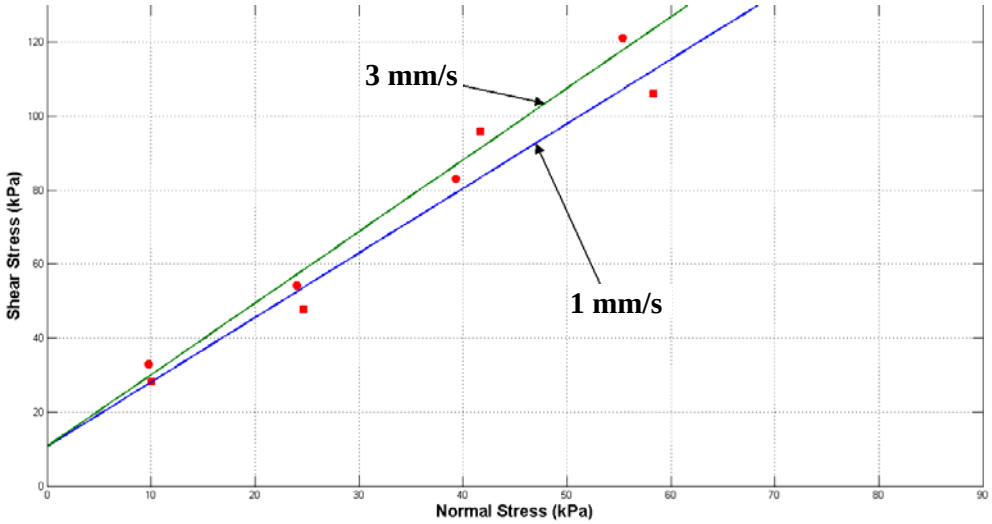

Figure C.5 - Internal Friction Angles (1 mm/s versus 3 mm/s Shear Velocity)

The internal friction angles are summarised in Table C.1:

Table C.1 - Internal Friction Angles for Additional Direct Shear Tests

Offset (mm)	Shear Velocity (mm/s)	ϕ (°)
0	1	60.2
70	1	56.4
0	3	62.7

Changing the DST set-up to one with an offset (also at 1 mm/s) yielded a 6.2% reduction in the internal friction angle. An increase of 4.1% is observed when the shear velocity is increased from 1 mm/s to 3 mm/s (both at no offset). These variations in the internal friction angle were considered insignificant, hence the effects of shear velocity and offset were not of any concern. The DST set-up with no offset and a shear velocity of 1 mm/s was therefore regarded as appropriate (for both the experimental work and DEM simulations) and implemented accordingly.

References

Alejano, L.R., Alonso, E. 2005. Considerations of the dilatancy angle in rocks and rock masses. *International Journal of Rock Mechanics & Mining Sciences.* 42(4):481–507.

Carson, J.W., Wilms, H. 2006. Development of an international standard for shear testing. *Powder Technology.* 167(1):1-9.

Coetzee, C.J. 2000. *Forced Granular Flow.* Master's thesis. Stellenbosch: University of Stellenbosch.

Coetzee, C.J., Basson, A.H., Vermeer, P.A. 2007. Discrete and continuum modelling of excavator bucket filling. *Journal of Terramechanics*. 44(2):177-186.

Coetzee, C.J., Els, D.N.J. 2009. Calibration of granular material parameters for DEM modelling and numerical verification by blade-granular material interaction. *Journal of Terramechanics.* 46(1):15–26.

Coetzee, C.J., Els, D.N.J., Dymond, G.F. 2010. Discrete element parameter calibration and the modelling of dragline bucket filling. *Journal of Terramechanics.* 47(1):33–44.

Cundall, P.A., Strack, O.D.L. 1979. A discrete numerical method for granular assemblies. Geotechnique. 29(1):47–65.

Curry, D., Favier, J., LaRoche, R.D. 2009. A Systematic Approach to DEM Material Model Calibration, in *The American Institute of Chemical Engineers (AIChE).* Tennessee: Nashville.

Del Vecchio, R.J. 1997. *Understanding Design of Experiments.* Munich: Hanser Gardner Publications.

Dymond, G.F.D. 2007. *Creation, optimization and verification of a three dimensional numerical model to simulate a dragline bucket during the digging cycle using modern DEM software*. Master's thesis. Stellenbosch: University of Stellenbosch.

Frenning, G. 2008. An efficient finite/discrete element procedure for simulating compression of 3D particle assemblies. *Computer Methods in Applied Mechanics and Engineering.* 197(49-50): 4266-4272.

Gröger, T., Katterfeld, A. 2006. On the numerical calibration of discrete element models for the simulation of bulk solids, in *Conveying and Handling of Particulate Solids (CHoPS-05).* Italy: Sorrento.

Hanley, K.J., O'Sullivan, C., Oliveira, J.C., Cronin, K., Byrne, E.P. 2011. Application of Taguchi methods to DEM calibration of bonded agglomerates. *Powder Technology.* 210(3):230-240.

Härtl, J., Ooi, J.Y. 2008. Experiments and simulations of direct shear tests: porosity, contact friction and bulk friction. *Granular Material.* 10(4):263-271.

Hastie, D.B., Grima, A.P., Wypych, P.W. 2008. Validation of particle flow through a conveyor transfer hood via particle velocity analysis, in *2nd International Conference and Exhibition on Storage, Handling and Transporting Bulk (Bulk Europe 2008)*. Czech Republic: Prague.

Head, K.H. 1988. *Manual of Soil Laboratory Testing.* Volume 2. London: Pentech Press.

Head, K.H. 1989. *Soil Technicians' Handbook.* London: Pentech Press.

Ileleji, K.E., Zhou, B. 2008. The angle of repose of bulk corn stover particles. *Powder Technology.* 187(2):110-118.

Itasca. 2003. *PFC3D (Particle Flow Code in 3 Dimensions) Theory and Background.* Version 3.0. Minneapolis: Itasca Consulting Group.

Kruggel-Emden, H., Rickelt, S., Wirtz, S., Scherer, V. 2008. A study on the validity of the multi-sphere Discrete Element Method. *Powder Technology.* 188(2):153-165.

Lee, DS., Kim, KY., Oh, GD., Jeong, SS. 2008. Shear characteristics of coarse aggregates sourced from quarries. *International Journal of Rock Mechanics & Mining Sciences.* 46(1):210-218.

Liu, S.H., Sun, D., Matsuoka, H. 2005. On the interface friction in direct shear test. *Computers and Geotechnics.* 32(5):317–325.

Malone, K.F., Xu, B.H. 2008. Determination of contact parameters for discrete element method simulations of granular systems. *Particuology.* 6(6):521-528.

Mio, H., Akashi, M., Shimosaka, A., Shirakawa, Y., Hidaka, J., Matsuzaki, S. 2008. Speed-up of computing time for numerical analysis of particle charging process by using discrete element method. *Chemical Engineering Science*, 64(5):1019-1026.

Nakashima, H., Shioji, Y., Kobayashi, T., Aoki, S., Shimizu, H., Miyasaka, J., Ohdoi, K. 2010. Determining the angle of repose of sand under low-gravity conditions using discrete element method. *Journal of Terramechanics.* 48(1):17-26.

Nordell, L.K. 1997. Particle Flow Modelling: Transfer chutes and other applications, in *International Materials Handling Conference (BELTCON 9)*. South Africa: Johannesburg.

Pillai, J.R., Bradley, M.S.A., Berry, R.J. 2007. Comparison between the angles of wall friction measured on an on-line wall friction tester and the Jenike wall friction tester. *Powder Technology*. 174(1-2):64–70.

Schwedes, J. 2003. Review on testers for measuring flow properties of bulk solids. *Granular Matter*. 5:1–43.

Tijskens, B., Van Besin, Vandewalle, Ramon. 2006. Large scale DEM, in *Conveying and Handling of Particulate Solids (CHoPS-05)*. Italy: Sorrento.

Vining, G.G. 1998. *Statistical Methods for Engineers.* United States of America: Duxbury Press.

Yan, W.M. 2008a. Effects of Particle Shape and Microstructure on Strength and Dilatancy During a Numerical Direct Shear Test, in *International Association for Computer Methods and Advances in Geomechanics (IACMAG).* Goa: India: 1340-1345.

Yan, W.M. 2008b. Fabric evolution in a numerical direct shear test. *Computers and Geotechnics.* 36(4):597-603.

Yoon, J., 2007. Application of experimental design and optimization to PFC model calibration in uniaxial compression simulation. *International Journal of Rock Mechanics & Mining Sciences.* 44(6):871-889.

Zhou, Y.C., Xu, B.H., Yu, A.B., Zulli, P. 2002. An experimental and numerical study of the angle of repose of coarse spheres. *Powder Technology*. 125(1):45-54.